

International Journal of Microscale and Nanoscale Thermal and Fluid Transport Phenomena

Volume 4, Number 1, 2013

Table of Contents

Editorial: In Celebration of Professor John Richard Thome on His 60th Birthday	1
<i>Lixin Cheng</i>	
Coupled Electrohydrodynamic-Dielectrophoretic Micropumping of Colloidal Suspensions in a Microchannel	5
<i>Guoliang He and Dong Liu</i>	
Onset of Nucleate Boiling and Critical Heat Flux with Boiling Water in Microchannels	25
<i>R. R. Bhide, S. G. Singh, Vijay S. Duryodhan, Arunkumar Sridharan, and Amit Agrawal</i>	
Melting Effect on Natural Convection about Axisymmetric Stagnation Point on a Surface in Porous Media with Soret and Dufour Effects and Temperature-Dependent Viscosity	49
<i>M. Modather, M. Abdou, and Ali J. Chamkha</i>	
Pushing the Limits of Liquid Cooling: Design and Analysis of a Direct Liquid Cooling System for Power Modules	71
<i>Matt Reeves, Jesus Moreno, Peter Beucher, Sy-Jenq Loong, and David Bono</i>	

International Journal of Microscale and Nanoscale Thermal and Fluid Transport Phenomena

The *International Journal of Microscale and Nanoscale Thermal and Fluid Transport Phenomena (IJMNTFTP)* is a quarterly, peer-reviewed, academic journal. It aims to provide a vehicle for the exchange and dissemination of original research results, technical notes, and state-of-the-art reviews pertaining to thermal and fluid transport phenomena at microscales and nanoscales. It covers a wide range of topics on fundamentals and applications of microscale and nanoscale transfer processes of mass, momentum, and energy such as microscale and nanoscale heat transfer and fluid flow, nanofluid heat transfer and flow, microfluidics, nanofluidics, and technologies based on these transport processes such as various microscale and nanoscale thermal and fluid devices, microscale and nanoscale energy systems, micro-cooling technology in the computer and electronics industries, MEMS (Micro-Electro-Mechanical-Systems) and NEMS (Nano-Electro-Mechanical-Systems), microscale and nanoscale thermal and fluid flow in mechanical-, chemical-, nuclear-, process-, petroleum-, precision-, and aerospace-engineering, micro-electronics, information technology and interdisciplinary research related to microscale and nanoscale thermal and fluid transport in bio-engineering, medical engineering, and life engineering, etc. The audience is made up of research scientists, graduates, engineers, and others concerned about these issues, who are working in academia and industry.

This journal is published quarterly by

Nova Science Publishers, Inc.
400 Oser Avenue, Suite 1600
Hauppauge, New York 11788-3619, USA
Telephone: (631) 231-7269
Fax: (631) 2131-8175
E-mail: nova.main@novapublishers.com
Web: www.novapublishers.com

ISSN: 1949-4955

Subscription Price per Volume (2013)

Print: \$235.00 Electronic: \$235.00 Combined Print + Electronic: \$352.50

Copyright © 2013 by Nova Science Publishers, Inc. All rights reserved. Printed in the United States of America. No part of this Journal may be reproduced, stored in a retrieval system, or transmitted in any form or by any means: electronic, electrostatic, magnetic, tape, mechanical, photocopying, recording, or otherwise without permission from the Publisher. The Publisher assumes no responsibility for any statements of fact or opinion expressed in the published papers.

EDITOR-IN-CHIEF

Dr. Lixin Cheng
School of Engineering
University of Portsmouth
Anglesea Building, Anglesea Road
Portsmouth PO1 3DJ, United Kingdom
Email: lixincheng@hotmail.com

EDITORIAL BOARD

Panagiota Angeli, Department of Chemical Engineering, University College London, UK
Gian Piero Celata, ENEA - Institute of Thermal-Fluid Dynamics, Italy
Ali J. Chamkha, Mechanical Production Engineering Department, Public Authority for Applied Education and Training, Shuwaikh, Kuwait
Ping-Hei Chen, Dept. of Mechanical Engineering, National Taiwan Univ., Taiwan, R.O.C.
Jacob N. Chung, Dept. of Mechanical and Aerospace Engineering, Univ. of Florida, USA
Stéphane Colin, Univ. de Toulouse, INSA, ICA (Institut Clément Ader), Toulouse, France
Afshin J. Ghajar, School of Mechanical and Aerospace Engineering, Oklahoma State University, USA
Rama S.R. Gorla, Dept. of Mechanical Engineering, Cleveland State University, Ohio, USA
Ralph Greif, Dept. of Mechanical Engineering, University of California, Berkeley, CA, USA
Takashi Hibiki, School of Nuclear Engineering, Purdue University, USA
Satish Kandlikar, Dept. of Mechanical Engineering, Rochester Inst. of Technology, USA
Tassos G. Karayiannis, School of Engineering and Design, Brunel University, UK
JungHo Kim, Department of Mechanical Engineering, University of Maryland, USA
Lei Liu, State Key Laboratory of Multiphase Flow in Power Engineering, Xi'an Jiaotong University, Xi'an, P. R. China
Dr-Ing. Dieter Mewes, Inst. of Multiphase Processes, Leibniz Univ. of Hanover, Germany
Gian Luca Morini, DIENCA, Alma Mater Studiorum Università di Bologna, Bologna, Italy
Sreekant V.J. Narumanchi, National Renewable Energy Laboratory, USA
Gherhardt Ribatski, Dept. of Mechanical Engineering, University of São Paulo, Brazil
Sujoy K. Saha, Mechanical Engineering Dept., Bengal Engineering and Science Univ., India
Khellil Sefiane, School of Engineering and Electronics, University of Edinburgh, Edinburgh, Scotland, UK
Professor Mashiro Shoji, Department of Mechanical Engineering, Kanagawa Univ., Japan
John R. Thome, Heat and Mass Transfer Laboratory (LTCM), Swiss Federal Institute of Technology Lausanne (EPFL), Switzerland
Cees van der Geld, Department of Mechanical Engineering, Eindhoven University of Technology, The Netherlands
Chien-Yuh Yang, Dept. of Mechanical Engineering, National Central Univ., Taiwan, R.O.C
Rin Yun, Department of Mechanical Engineering, Hanbat National University, South Korea

EDITORIAL:
IN CELEBRATION OF PROFESSOR
JOHN RICHARD THOME ON HIS 60TH BIRTHDAY

*Lixin Cheng**

School of Engineering, Univeristy of Portsmouth,
Portsmouth, UK

Prof. Thome is a well-known expert in the field of two-phase flows and heat transfer, having made many outstanding contributions to two-phase flow and heat transfer, through his research, reference books, teaching, standards, community service and engineering applications. He was born in Easton, PA. U.S.A. on February 25 1953 and grew up in Michigan. His past and curent research work spans nearly all areas of boiling and condensation and two-phase flows, covering both internal flows and external flows, enhanced heat transfer, micro/macro-scale heat transfer, pure fluid and mixtures, numerical modeling of two-phase phenomena and flows, and many special applications. He has published more than 180 journal papers with more than 4500 citations since joining the EPFL in 1998, with an H-factor of 33 (Scopus).

He is Professor of Heat and Mass Transfer at the Ecole Polytechnique Fédérale de Lausanne (EPFL), Switzerland since 1998, where he is director of the Laboratory of Heat and Mass Transfer at the EPFL with a research staff of about 18-20 Ph.D. students and post-doctoral researchers, website at <http://lcm.epfl.ch> He is also Director of the EPFL Doctoral Programme in Energy since its founding. For many years, until the end of 2011, he was also the Director of the ERCOFTAC European Coordination Center (*European Research Community On Flow, Turbulence And Combustion*) with about 180 affiliated universities, research centers and industrial companies. He was the host of the recent 8th ECI International Boiling and Condensation Heat Transfer Conference in June, 2012. He is the Swiss delegate to the Assembly of the International Heat Transfer Conference, which organizes the International Heat Transfer Conference every four years. He is associate editor of *Heat Transfer Engineering* and editorial board member of *International Journal of Microcale & Nanoscale Thermal and Fluid Transport Phenomena (IJMNTFTP)*. He has hosted the European Two-Phase Flow Group Meeting in Lausanne and will host the next joint European-Japanese Two-Phase Flow Group Meeting in Switzerland in 2015. He has over 60 published prediction methods that are widely used in engineering practice...his motto is that

* Corresponding author, tel: +44 2392842583, fax: +44 2392842351, email: lixincheng@hotmail.com.

the real test of quality research is not journal papers and citations, but their widespread adoption by industry. Prof. Thome is also Chairman of ALPEMA (the Aluminum Plate Exchangers Manufacturers Association) that publishes industrial standards for the plate-fin heat exchangers widely used in cryogenic and LNG services...the new 3rd Edition of the ALPEMA Standards came out in 2010 under his tutelage.

Prof. Thome received his Ph.D. at Oxford University, England in 1978 and was then an assistant/associate professor at Michigan State University. From 1984 to 1998, he ran his own successful international engineering consulting company that specialized in developing new thermal engineering technologies for the refrigeration and petrochemical industries. He returned to academia in 1998 with his appointment at the EPFL. He is the author of four widely used books: *Enhanced Boiling Heat Transfer* (Hemisphere/Taylor&Francis, 1990), *Convective Boiling and Condensation, 3rd Edition* (Oxford University Press, 1994 with J.G. Collier), *Wolverine Engineering Databook III* (free e-book, 2004 and updated annually, with 21 chapters and over 200 embedded videos) and *Nucleate Boiling on Micro-Structured Surfaces* (free e-book, 2008 with M.E. Poniewski). He received the *ASME Heat Transfer Division's Best Paper Award* in 1998 for a 3-part paper on two-phase flow and flow boiling heat transfer published in the *Journal of Heat Transfer*. He has received the *J&E Hall Gold Medal* from the U.K. Institute of Refrigeration in 2008 for his extensive work on microscale refrigeration heat transfer and the *2010 ASME Heat Transfer Memorial Award* for his career work on flow pattern based heat transfer models for macro and micro-scale flows. He received the *2011/2012 Very Highly Commended Paper Award* from the *International Journal of Refrigeration*. One of his PhD students (R. Revellin) won the 2004-2007 Eurotherm Prize in 2008 for Best European Ph.D. Thesis in thermal engineering. He also hosts an annual one-week summer school on "Microscale Single- and Two-Phase Flow and Heat Transfer" each June at the EPFL and bi-annually also hosts the "Boiling" course at the EPFL.

Most of his research interests are directed on the joint topic of two-phase flow and two-phase heat transfer, where his group at the LTCM lab is one of the world's premier research groups in this area. He has proposed many widely used prediction methods for: flow pattern maps in macro- and micro-channels, flow boiling and condensation in macro- and micro-channels and flattened tubes, critical heat flux, two-phase pressure drops, entrainment, void fraction, enhanced pool boiling heat transfer, bundle boiling heat transfer, falling film evaporation and dryout, falling film condensation, mixture boiling effects, oil effects on two-phase heat transfer, flow boiling in microfin tubes, flow boiling of CO₂, pressure drops in U-bends, etc. Nearly all these methods have become the standard for industrial practice. His CO₂ flow pattern based flow boiling heat transfer model for macro- and micro-scale channels has been found to be highly accurate for CO₂ flow boiling and is being used to simulate CO₂ cooling of the new generation of particle detectors in development at CERN, the Stanford Linear Accelerator Lab and the Fermi lab.

He is also active in numerical modeling of two-phase flows, including work on condensation in circular and non-circular microchannels and micro-gravity flows, UDF modified versions of Fluent for two-phase flows, and a new 3D/ALE-FEM numerical code for two-phase flow and evaporation in microchannels. In this respect, he works hard to validate all these codes against independent test data, thus bringing more general faith to the validity and practical use of two-phase numerical modeling. His experimental activities now cover micro-PIV and newly developed micro-shadow-velocimetry (micro-PSV) of single-

and two-phase flows in microchannels and orifices, in addition to annular down-flows. He has proposed the first flow pattern-based suite of macroscale methods for predicting flow pattern transitions, flow boiling heat transfer, condensation heat transfer and two-phase pressure drops. He has also proposed the leading methods for flow boiling and critical heat flux in microchannels, just now adding a flow pattern-based model to this topic and has also just developed the first experimentally-validated simulation tool for combined heat spreading and flow spreading for multichannel micro-evaporators with non-uniform heat fluxes and hotspots. He has in recent years also proposed the first unified suite of annular flow models for predicting void fraction, entrainment, liquid film thickness, convective heat transfer and pressure drops in macro-and microscale annular flows, which so far are also proving there is not macro-to-microscale transition in annular flow. Recently, he has also extended his experimental research to cover two-phase flow control for electronics cooling and new hybrid cooling cycles, using speed control on oil-free pumps and compressors. His work is widely used in engineering practice in diverse industries: refrigeration, air-conditioning, petrochemical, nuclear, electronics cooling, high energy physics particle detectors, LNG, etc.

In occasion of his 60th birthday, on behalf of his colleagues, students and friends all over the world, we all wish him a very happy birthday and happiness with his wife Carla and sons Luca and Alessandro. John is still a young sixty, as he is very active in his research and teaching covering important topics in heat transfer and continues to add new topics of research to his laboratory. He has an unending enthusiasm for research on fundamental two-phase heat transfer and promotion of the new young generation of heat transfer researchers (he obtained 45 conference fellowships from 5 different sponsors for the 8th ECI Boiling and Condensation Heat Transfer Conference to bring the younger generation to this important event of our discipline). We all wish the best on his sixtyth birthday, and we look forward to his continued contribution to the field of two phase flow and heat transfer.



Prof. John Richard Thome (Editorial Board Member of IJMNTFTP)

COUPLED ELECTROHYDRODYNAMIC- DIELECTROPHORETIC MICROPUMPING OF COLLOIDAL SUSPENSIONS IN A MICROCHANNEL

*Guoliang He and Dong Liu**

Department of Mechanical Engineering
University of Houston, Houston, Texas, USA

ABSTRACT

Effective and versatile microfluidic pumps can be produced by utilizing various electrokinetic effects, such as electrohydrodynamics (EHD), induced-charge electroosmosis (ICEO) and dielectrophoresis (DEP). Among these, traveling-wave EHD (twEHD) has emerged as a powerful pumping mechanism due to its potential for miniaturization and the ability to pump a variety of liquids. However, when twEHD is used to deliver colloidal suspensions, the simultaneous presence of EHD effect may favorably or adversely influence the overall pumping performance, or vice versa. The net flow depends on the particle-fluid combination and the frequency range of the applied electric field. In this paper, the coupled EHD-twDEP flow was studied numerically in a microchannel with a three-phase interdigitated microelectrode array fabricated at the bottom surface. The results show that, depending on the frequency range of the traveling-wave electric field and the applied thermal boundary condition, the EHD-induced flow can significantly enhance or weaken the twDEP-induced flow.

Keywords: Electrohydrodynamics, dielectrophoresis, traveling-wave, micropump

NOMENCLATURE

A Particle radius, μm
D Electrical diffusivity, m^2/s
E Electric field, kV/m
F Force, N
H Height of microchannel, μm
J Current density, A/m^2

* To whom correspondence should be addressed. Email: dongliu@uh.edu. Phone: (01)713-743-4532. Fax: (01)713-743-4530.

K Thermal conductivity, W/(m K)
 L Characteristic length, μm
 T Temperature, K
 U Characteristic velocity, $\mu\text{m/s}$
 d Width or spacing, μm
 f Frequency, Hz
 p Dipole moment, C m_t Time, s
 u Velocity, $\mu\text{m/s}$

Greek symbols

α Thermal diffusivity, m^2/s
 ε Electrical permittivity, F/m
 λ Wavelength, μm
 μ Viscosity, N s/m²
 ρ Density, kg/m³
 ρ_q Charge density, C/m³
 σ Electrical conductivity, S/m
 ϕ Electric potential, V
 Ω Angular frequency, rad/s

Subscripts

b Body
 e External
 f Fluid
 m Medium
 p Particle
 r Relative

1. INTRODUCTION

The ability to generate and control fluid flow in small amounts with high precision is critical to the continued growth of microfluidic technology, which is now widely applied in drug delivery [1], chemical synthesis [2], biological diagnostics [3] and electronics cooling [4]. Conventional pumping methods driven by mechanical means are unsuitable for microfluidic applications due to their limits in miniaturization and lack of precision and flexibility in controlling low flow rates [5, 6]. Among the alternative solutions, a particularly attractive scheme is to exploit the AC electrokinetic effects, i.e., to generate the flow by inducing electrical forces in the fluid with an applied traveling-wave electric field. Based on the origin of the electrical forces, electrokinetic micropumps can be classified as the induced-charge electroosmotic (ICEO) micropump [7,8], dielectrophoretic (DEP) micropump, and electrohydrodynamic (EHD) micropump [10-12], etc.

In ICEO micropumps, the electrical double layer (EDL) is formed by the normal component of the traveling-wave field at the interface between the electrode and the electrolyte solution. The tangential component of the electric field acts on the mobile charges accumulated in the EDL, giving rise to a force that pulls the fluid along the direction of the traveling wave. The EHD micropumps are also generated through the interaction of an electric field with induced charges (ions), but the charge induction usually occurs in the bulk fluid due to the presence of a temperature gradient produced by anisotropic heating. The induced ions can be attracted or repelled by the traveling-wave field, depending on the direction of the temperature gradient, so that the fluid moves together with the ions owing to viscous drag. Although both ICEO and EHD micropumps involve a traveling-wave field, they can be discerned without ambiguity because they operate at very different frequency range [9, 13]. For instance, the maximum effect of EHD occurs near the charge relaxation frequency $f_c = \sigma_m / (2\pi\epsilon_m)$ [14], while the optimal frequency of ICEO is around $f_{ICEO} = [\sigma_m / (2\pi\epsilon_m)] / (\lambda_D / L)$, where λ_D is the Debye length and L is the characteristic length of the system, and f_{ICEO} is several orders of magnitude smaller than f_c .

Traveling-wave DEP (twDEP) is the sustained motion of dielectric particles in a fluid medium when exposed to a multi-phase (> 2 phases) traveling-wave field [15]. The driving force for particle motion originates from the interaction of the applied field with the induced electric dipole in the particles. When the moving particles drag the surrounding fluid together with them, an appreciable net flow, i.e., the twDEP micropumping effect, is generated [15]. The maximum twDEP is expected to take place near the Maxwell-Wagner relaxation frequency, f_{M-W} ,

$$f_{M-W} = \frac{1}{2\pi} \left(\frac{\sigma_p + 2\sigma_m}{\epsilon_p + 2\epsilon_m} \right) \quad (1)$$

This frequency is of the same order of magnitude of the charge relaxation frequency of EHD (f_c) at which the maximum EHD pumping occurs. In fact, f_{M-W} and f_c can coincide for certain particle-fluid combinations, for instance, if $\sigma_p \ll 2\sigma_m$ and $\epsilon_p \ll \epsilon_m$, f_{M-W} will reduce to f_c . Furthermore, the velocity fields produced by twDEP micropumping and EHD micropumping are typically comparable in magnitude, while the flow directions may be totally opposite (as will be discussed below). Consequently, when a traveling-wave electric field is applied to transport colloidal suspensions, where the subject of interest can be either the particles or the carrier liquid, twDEP-induced flow and EHD-induced flow are simultaneously present, and the two pumping mechanisms may cooperate or compete with each other, depending on their relative flow directions with respect to the applied field. Thus, it is important to analyze the EHD-twDEP coupled flow and its potential variations in order to ensure satisfactory liquid/particle delivery capability of a microfluidic system that employs the AC electrokinetic effects [9, 16-18].

In this paper, the coupled EHD- and twDEP electrokinetic flow was studied numerically in a microchannel with an interdigitated microelectrode array fabricated at the bottom surface. The temperature gradient for EHD flow was induced by Joule heating in the electrolyte solution, and both the repulsion-type and the attraction-type EHD were considered. The flow field due to twDEP was solved using an equivalent mixture approach. The results show that,

depending on the frequency range of the traveling-wave field and the thermal boundary condition, the EHD effect and the twDEP effect can work either synergistically or competitively to strengthen or weaken the net flow generated.

2. THEORY AND ANALYSIS

2.1. Electrohydrodynamics

EHD flow arises as the result of the interaction of an electric field with free charges induced in a fluid medium. The charge induction occurs when a temperature gradient ∇T exists in the bulk of the liquid, which brings about gradients in the temperature-dependent electrical conductivity and permittivity. Upon the application of an electric field, the electrical force drives the free charges into motion, thereby producing the bulk fluid flow. EHD pumping due to preexisting temperature gradient, e.g., a temperature difference imposed across the boundaries of the fluid, has been studied extensively for heat transfer enhancement applications [14, 19-21]. Under a difference circumstance where the fluid medium has a non-negligible electrical conductivity, the electric field used in electrokinetics studies is usually high enough to generate appreciable Joule heating, which can produce a substantial temperature gradient in the bulk liquid [22]. EHD originating from Joule heating is also termed the electrothermal effect [23], and is considered in this work. The steady-state energy equation for the fluid is given as

$$\rho c_p (\vec{u} \cdot \nabla T) = k \nabla^2 T + \sigma E^2 \quad (2)$$

where the heat generation source term σE^2 is due to Joule heating.

The electrical force due to EHD is given by [24]

$$\vec{f}_e = \rho_q \vec{E} - \frac{1}{2} E^2 \nabla \varepsilon \quad (3)$$

where ρ_q is the free charge density, and \vec{E} is the electric field. The two terms at the right hand side (RHS) of Eq. (3) represent the Coulomb and dielectric forces, respectively. The free charge density is related to the electric field by Gauss's law

$$\rho_q = \nabla \cdot (\varepsilon \vec{E}) \quad (4)$$

and the charge conservation equation is

$$\frac{\partial \rho_q}{\partial t} + \nabla \cdot \vec{J} = 0 \quad (5)$$

where the current density \vec{J} consists of the convection current, the conduction current and the diffusion current, and is given by

$$\vec{J} = \rho_q \vec{u} + \sigma \vec{E} - D \nabla \rho_q \quad (6)$$

where D is the electrical diffusivity. The convection and diffusion currents can be neglected in this work since they are much smaller than the conduction current [23, 25].

Assuming small variations in the permittivity and electrical conductivity, the electric field can be written as the sum of the applied component \vec{E}_0 and the perturbation component \vec{E}_1 , where $\vec{E} = \vec{E}_0 + \vec{E}_1$ and $|\vec{E}_0| \gg |\vec{E}_1|$. The electrical force becomes

$$\vec{f}_e = \left(\nabla \varepsilon \cdot \vec{E}_0 + \varepsilon \nabla \cdot \vec{E}_1 \right) \vec{E}_0 - \frac{1}{2} E_0^2 \nabla \varepsilon \quad (7)$$

Equations (4) and (5) can be combined as

$$\nabla \sigma \cdot \vec{E}_0 + \sigma \nabla \cdot \vec{E}_1 + \frac{\partial}{\partial t} \left(\nabla \varepsilon \cdot \vec{E}_0 + \varepsilon \nabla \cdot \vec{E}_1 \right) = 0 \quad (8)$$

In an applied AC field of angular frequency ω , $\vec{E}_0(t) = \text{Re}(\vec{E}_0 e^{i\omega t})$ and $\partial / \partial t = i\omega$, where $\text{Re}(\dots)$ is the real part of a complex quantity. From Eq. (8), it follows

$$\nabla \cdot \vec{E}_1 = \frac{-(\nabla \sigma + i\omega \nabla \varepsilon) \cdot \sigma + i\omega \nabla \varepsilon}{\sigma + i\omega \varepsilon} \quad (9)$$

Putting Eqs. (7) and (9) together, the time-averaged electrical force can be written as

$$\langle \vec{f}_e \rangle = \frac{1}{2} \text{Re} \left\{ \left[\frac{(\sigma \nabla \varepsilon - \varepsilon \nabla \sigma) \cdot \vec{E}_0}{\sigma + i\omega \varepsilon} \right] \vec{E}_0^* - \frac{1}{2} E_0^2 \nabla \varepsilon \right\} \quad (10)$$

where $*$ denotes the complex conjugate. The variations in permittivity and conductivity are related to the temperature gradient as

$$\frac{\nabla \sigma}{\sigma} = \frac{1}{\sigma} \left(\frac{\partial \sigma}{\partial T} \right) \nabla T \quad (11)$$

and

$$\frac{\nabla \varepsilon}{\varepsilon} = \frac{1}{\varepsilon} \left(\frac{\partial \varepsilon}{\partial T} \right) \nabla T \quad (12)$$

The EHD-induced flow field can be described by the Navier-Stokes equations for an incompressible fluid

$$\rho \left(\frac{\partial \vec{u}}{\partial t} + \vec{u} \cdot \nabla \vec{u} \right) = -\nabla p + \mu \nabla^2 \vec{u} + \vec{f}_b + \vec{f}_e \quad (13)$$

and the continuity equation

$$\nabla \cdot \vec{u} = 0 \quad (14)$$

where \vec{f}_b is other body forces if present. Considering the small velocity involved in most microfluidic studies, the inertia term can be omitted from Eq. (13) since the Reynolds number is usually less than unity ($\text{Re} = \rho u L / \mu \leq 1$). Further neglecting the body force, Eq.(13) reduces to the Stokes equation

$$0 = -\nabla p + \mu \nabla^2 \vec{u} + \vec{f}_e \quad (15)$$

2.2. Dielectrophoresis

Dielectrophoresis (DEP) is the motion of dielectric particles in colloidal suspensions when exposed to non-uniform electric fields [15]. When an electric field is applied, the redistribution of electrical charges in the particle gives rise to an induced dipole across the particle.

The induced dipole tends to align with the applied field. The induced dipole moment, \vec{p} , and the dielectrophoretic force, \vec{F} , are given by

$$\vec{p} = 4\pi a^3 \varepsilon_m \left(\frac{\varepsilon_p - \varepsilon_m}{\varepsilon_p + 2\varepsilon_m} \right) \vec{E} \quad (16)$$

$$\vec{F} = (\vec{p} \cdot \nabla) \vec{E} = 2\pi a^3 \varepsilon_m \left(\frac{\varepsilon_p - \varepsilon_m}{\varepsilon_p + 2\varepsilon_m} \right) \nabla \vec{E}^2 \quad (17)$$

If the applied field is non-uniform ($\nabla \vec{E} \neq 0$), the particle will experience a net force and move [15, 26]. In a DC field, the particles can either undergo positive DEP, i.e., they are attracted to the maxima of the field, or experience negative DEP, i.e., they are repelled to the field minima.

Sustained particle motion is possible when an AC traveling-wave field is applied with appropriate driving frequencies. The AC dielectrophoretic force on the particle can be expressed using the frequency-dependent permittivity as [26]

$$\vec{F} = 2\pi a^3 \varepsilon_m \left(\frac{\tilde{\varepsilon}_p - \tilde{\varepsilon}_m}{\tilde{\varepsilon}_p + 2\tilde{\varepsilon}_m} \right) \nabla \bar{E}^2 \quad (18)$$

where $\tilde{\varepsilon}$ is $\tilde{\varepsilon} = \varepsilon - i(\sigma / \omega)$ and $i = \sqrt{-1}$. In the time domain, the time-averaged DEP force becomes [18]

$$\langle \vec{F}_{DEP} \rangle = \pi a^3 \varepsilon_m \operatorname{Re}(f_{CM}) \nabla |\bar{E}|^2 + 2\pi a^3 \varepsilon_m \operatorname{Im}(f_{CM}) (E_x^2 \nabla \varphi_x + E_y^2 \nabla \varphi_y + E_z^2 \nabla \varphi_z) \quad (19)$$

where the Clausius-Mossotti factor, f_{CM} is a complex parameter, defined as

$$f_{CM} = \frac{\tilde{\varepsilon}_p - \tilde{\varepsilon}_m}{\tilde{\varepsilon}_p + 2\tilde{\varepsilon}_m} \quad (20)$$

in which $\operatorname{Re}(f_{CM})$ and $\operatorname{Im}(f_{CM})$ denote the real and imaginary parts of f_{CM} ; E_x , E_y and E_z are the three directional components of the electric field; and φ_x , φ_y and φ_z are the phase angles. The first term on the RHS of Eq. (19) determines the alignment of the DEP force with respect to the maxima/minima of the electric field, and the second term appears only in a traveling-wave field and therefore, is called the traveling-wave DEP (twDEP) force component.

When the particles are driven into motion by twDEP, the viscous drag will pull the surrounding fluid to move together with the particles. Eventually, for each particle, the twDEP driving force is balanced by the viscous drag force

$$\langle \vec{F}_{DEP} \rangle = -6\pi \mu_f a (\vec{u}_m - \vec{u}_p) \quad (21)$$

Once the equilibrium state is reached, a steady flow field will be established around the particle. In a particle suspension where a large number of particles are present, the particle-particle hydrodynamic interactions take place as the inter-particle distance decreases, which will intensify the induced flow field [27]. Consequently, an appreciable net flow can be produced by the collective pumping action [9].

2.3. Interference between EHD and twDEP

The direction of EHD flow with respect to the traveling-wave field is determined by the temperature distribution in the fluid [14]. When the lowest fluid temperature happens to be near/at the electrodes where the electric field is most intense, the induced free charges will be attracted toward the traveling wave and the fluid will follow the electric field in the same direction, resulting in the attraction-type EHD. Conversely, as in the case of repulsion-type

EHD where the fluid temperature is higher near/at the electrodes, the induced flow will be opposite to the direction of the traveling wave.

The twDEP motion of particles with respect to the traveling wave field is contingent upon the Clausius-Mossotti factor, f_{CM} , as indicated by Eq. (19). Figure 1 illustrates $\text{Re}(f_{CM})$ and $\text{Im}(f_{CM})$ as a function of the frequency of the applied field (where the particle-fluid combination is polystyrene particles suspended in the 2.2×10^{-5} M KCl solution). It is seen that $\text{Re}(f_{CM})$ is always negative over the entire frequency range, i.e., the particles undergo negative DEP so that they can move freely without being immobilized onto the electrodes. $\text{Im}(f_{CM})$ vanishes at both extremes of the frequency spectrum, and only assumes non-zero values in the mid-range around the cross-over frequency (f_{M-W}). When $\text{Im}(f_{CM})$ is not trivial, the resulting twDEP force will propel the particles either along or against the propagation direction of the traveling wave, depending on the sign of $\text{Im}(f_{CM})$. For the particle-fluid combination used in this work, Figure 1 shows $\text{Im}(f_{CM}) < 0$, the particles as well as the twDEP-induced flow will move against the traveling wave. Therefore, when considering both EHD and twDEP effects, the net induced flow can be either enhanced if the EHD-induced flow is repulsion-type (i.e., also against the traveling wave), or diminished if the EHD-induced flow is attraction-type (i.e., along the traveling wave), depending on the temperature distribution in the fluid.

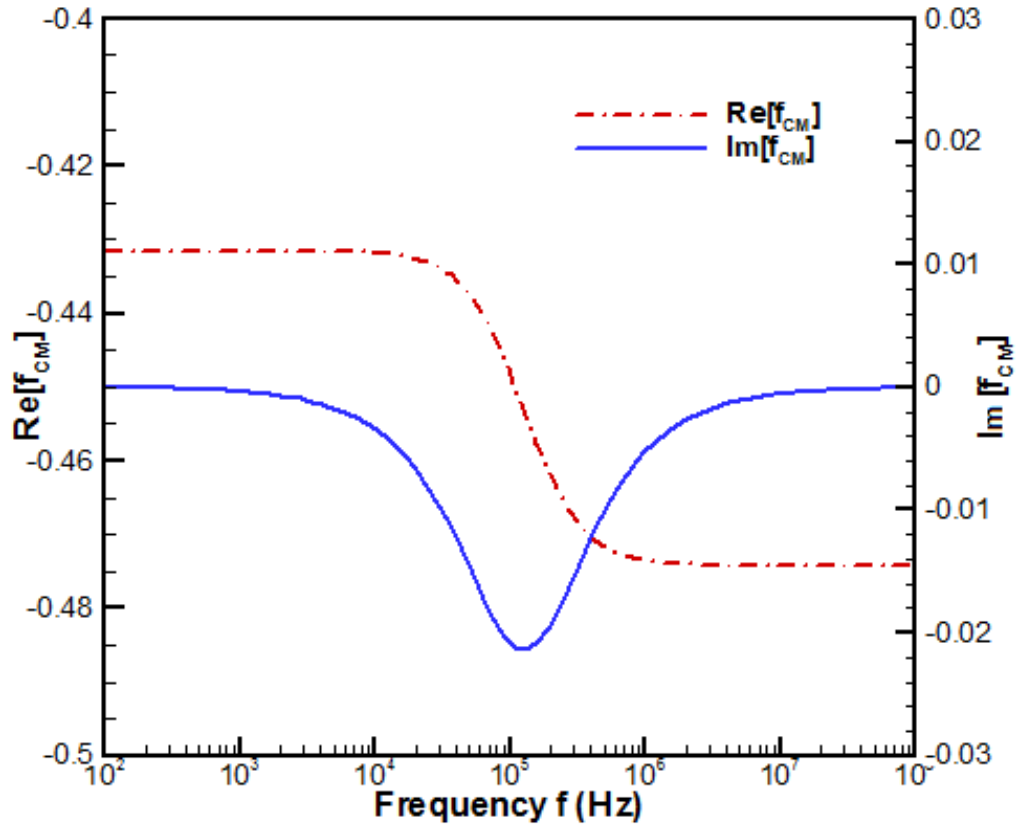


Figure 1. Frequency-dependence of $\text{Re}(f_{CM})$ and $\text{Im}(f_{CM})$.

3. NUMERICAL MODELS

The microfluidic system to be modeled consists of an array of three-phase, planar parallel microelectrodes fabricated on a silicon substrate, a microchannel, and a glass cover slide, as shown in Figure 2. The height of the microchannel formed is $50\ \mu\text{m}$. The electrodes are very thin ($\sim 100\ \text{nm}$) and are $8\ \text{mm}$ long.

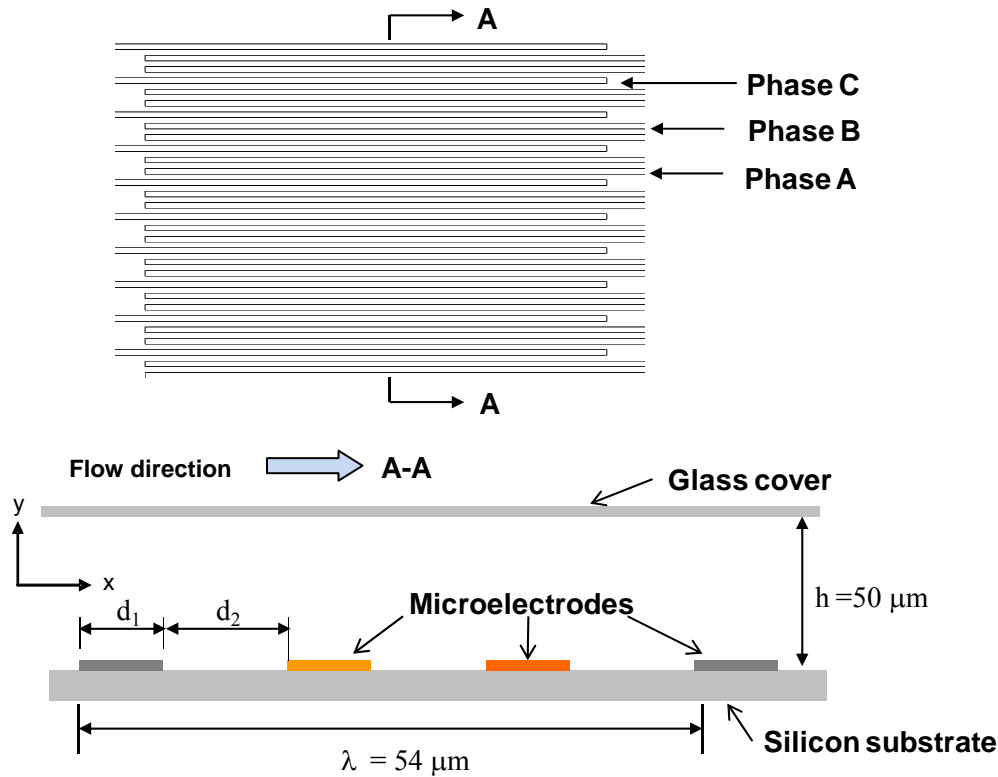


Figure 2. The microfluidic system: a silicon substrate, a glass cover slide, a microelectrode array and a microchannel. A top view of the three-phase electrode array is shown in the upper location, and the cross-sectional view (A-A) of the microchannel shown in the lower location where $d_1 = 6\ \mu\text{m}$ and $d_2 = 12\ \mu\text{m}$.

They have a width and a spacing of $d_1 = 6\ \mu\text{m}$ and $d_2 = 12\ \mu\text{m}$, which yield a wavelength of $\lambda = 3(d_1 + d_2) = 54\ \mu\text{m}$. The electrode array can be treated as a two-dimensional system because the length ($8\ \text{mm}$) along the transverse direction is considered infinite relative to the other two dimensions. The computational domain is shown in Figure 3 where the electric, temperature and velocity fields will be solved, respectively. Due to periodicity consideration, only a distance of one wavelength along the electrodes is modeled which covers three electrodes and the inter-spacing gaps.

A low-concentration KCl solution ($2.2 \times 10^{-5}\ \text{M}$) is used as the working fluid in both EHD and twDEP simulations. The solution has an electrical conductivity of $\sigma = 5.43 \times 10^{-4}$

S/m, a dielectric constant of $\epsilon_r = 80$, and the temperature coefficients of $2.11\% \text{ K}^{-1}$ for σ and $-0.4\% \text{ K}^{-1}$ for ϵ [14].

The density, viscosity and thermal conductivity of the KCl solution are assumed to be the same as water ($\rho = 997 \text{ kg/m}^3$, $\mu = 5.28 \times 10^{-4} \text{ N s/m}^2$ and $k = 0.7 \text{ W/(m K)}$), respectively, due to the low electrolyte concentration. In the twDEP simulation, polystyrene microparticles of $2.9 \text{ }\mu\text{m}$ diameter are dispersed in the KCl solution at a volume fraction of 1%. The electrical conductivity and dielectric constant for polystyrene are $\sigma = 5.2 \times 10^{-5} \text{ S/m}$ and $\epsilon_r = 2.8$.

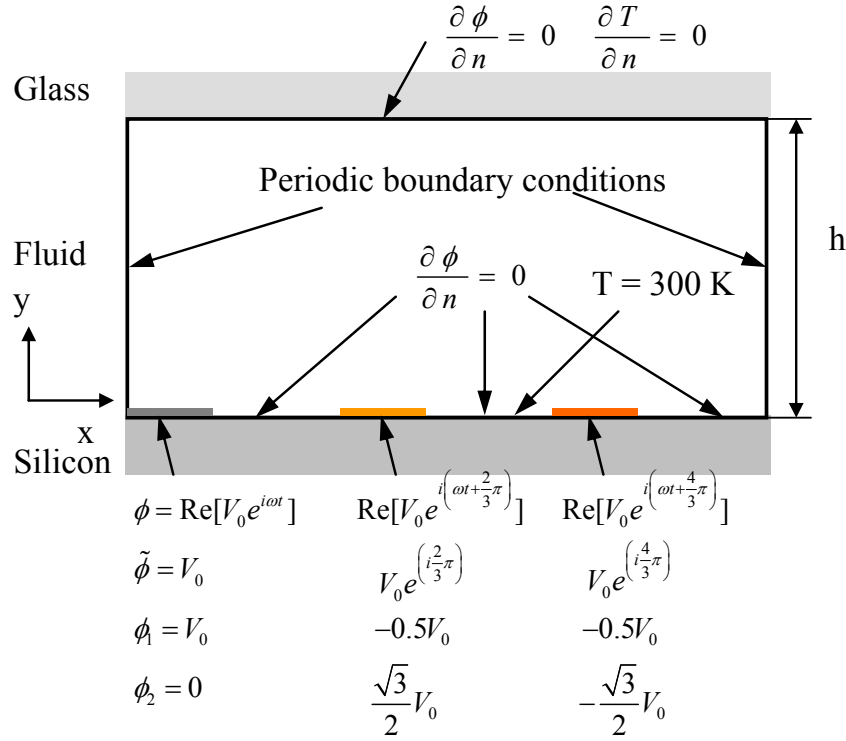


Figure 3. The computational domain and the electrical boundary conditions.

3.1. Electric Field

The electric fields are generated by applying a traveling-wave voltage signal to the three-phase electrode arrays. For a harmonic electric field of angular frequency ω , the electrical potential in the computational domain can be written in phasor notation as [28]

$$\phi(\vec{x}, t) = \text{Re}[\tilde{\phi}(\vec{x}) e^{i\omega t}] \quad (22)$$

where the phasor $\tilde{\phi} = \phi_1 + i\phi_2$, and $\omega = 2\pi f$ (f is the frequency of the applied field). The electric field is obtained from $\vec{E}(\vec{x}, t) = \text{Re}[\vec{\tilde{E}}(\vec{x}) e^{i\omega t}]$, where $\vec{\tilde{E}}(\vec{x}) = -\nabla \tilde{\phi} =$

$-(\nabla\phi_1 + i\nabla\phi_2)$. Since the fluid and the particles are assumed to be homogeneous, linear dielectric materials, both ϕ_1 and ϕ_2 satisfy Laplace's equation $\nabla^2\phi_i = 0$ ($i = 1, 2$).

The boundary conditions are specified as follows. At the top glass surface, a Neumann condition ($\partial\phi/\partial n = 0$) is assumed, where n is the normal to the boundary [25]. At the bottom surface, three-phase traveling-wave potentials are assigned to the electrodes, as shown in Figure 3. A sinusoidal voltage $\phi(t) = \text{Re}[V_0 e^{i\omega t}]$ is applied to the first electrode, and the signals are phase-shifted by $2/3\pi$ on consecutive electrodes. The corresponding boundary values of ϕ_1 and ϕ_2 on the electrodes are illustrated in Figure 3. For the inter-spacing gaps, the Neumann condition is specified since the neighboring electrodes are isolated from each other by using dielectric films, which results in zero potential flux in the gaps. Periodic boundary conditions are imposed at the left and right boundaries of the computational domain.

3.2. Temperature and Velocity Fields

Since the thermal conductivities of glass and silicon are two orders of magnitude different (i.e., 1.4 W/mK for glass and 148 W/mK for silicon), two different kinds of thermal boundary conditions are considered. Under the first thermal boundary condition (BC-1), the top surface is assumed adiabatic ($\partial T/\partial n = 0$), and the bottom surface is assumed isothermal, i.e., at the room temperature 300 K as a result of good conduction through the silicon substrate. This is the standard thermal boundary condition used in solving heat transfer problems in microchannel flow through silicon-based microfluidic devices [29]. When heat losses due to natural convection are considerable, the second kind of thermal boundary condition (BC-2) is possible, where a convective heat transfer coefficient of 30 W/m² K is applied to both the top and bottom boundaries [30]. Under steady state, thermally fully developed boundary conditions are assigned to the vertical edges (i.e., inlet and outlet) of the computational cell. The boundary conditions for the velocity field calculation are: (1) no-slip conditions for the top and bottom surfaces and (2) periodic conditions for the flow inlet and outlet.

3.3. Numerical Methods

A commercial computational fluid dynamics (CFD) software package, FLUENT, is employed to solve the electrothermal and electrohydrodynamic problems. The general solution procedures are as follows. First, the electrical potential (ϕ) and the electric field (\vec{E}) are acquired by solving the Laplace's equation $\nabla^2\phi = 0$. Then the solutions are used in conjunction with the user-defined functions to compute the EHD force and DEP force defined in Eqs. (10) and (19). Finally, the Stokes equations are solved to obtain the velocity field.

In the EHD simulation, the velocity and temperature fields are coupled and can be calculated by solving Eqs. (2), (13) and (14) simultaneously. It is noted that if the temperature gradient in EHD is established by a pre-existing constant temperature difference across the boundary of the fluid ($\nabla T = \text{constant}$), the electrical force can be calculated directly from Eqs. (10) through (12) without having to solve the energy equation.

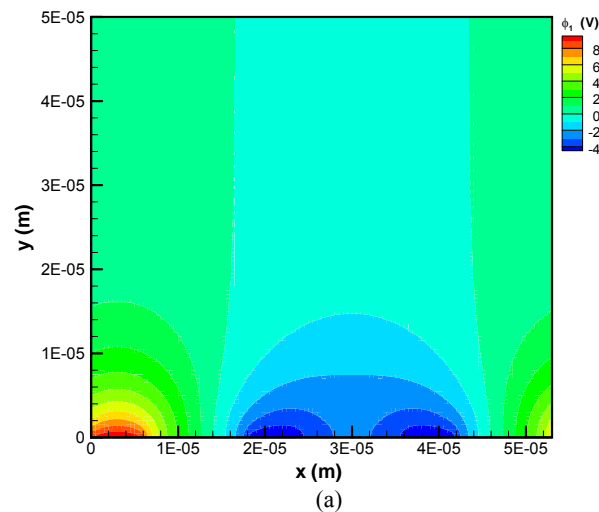
In the DEP calculation, the electrical force acts on discrete solid particles rather than on the continuous fluid elements. However, an accurate solution of the fluid-particle interactions in a Lagrangian frame requires the use of two-way coupling algorithm, and is computationally prohibitive for a colloidal system containing a large number of particles. Instead, a simplified, equivalent mixture model is adopted in this work. The DEP force is treated as a continuous body force *in the fluid* by volume-averaging, i.e., the DEP force on one particle is averaged over the fluid volume surrounding that particle, whose size is determined by the particle volume fraction. This continuous approach is warranted by the fact that there are ample particles in the suspension and their random passages in space make their presence *ergodic* [9]. The DEP force is then used as the electric force term in Eq. (13) to solve for the induced flow field. By following this procedure, the complex solid-liquid two-phase flow problem is converted to an equivalent, but more straightforward single-phase fluid flow problem.

In the simulations, the computational domain was discretized using a 106×200 (x-y) grid. Simulations with different grids showed a satisfactory grid-independence for the results obtained with this mesh size. The simulations were performed for $V_0 = 10$ V and three frequencies of $f = 10$ kHz, 100 kHz and 1 MHz, respectively.

4. RESULTS AND DISCUSSION

4.1. Electric Field Solution

Numerical results for the electric potential and the electric field are illustrated in Figure 4 for $V_0 = 10$ V. Figure 4(a) shows that the electric potential decays rapidly with increasing distance from the electrode surface. Since the density of the field lines is proportional to the strength of the electric field, Figure 4(b) shows clearly that the field maxima are located near the edges of the electrodes, and the local minima appear in the inter-spacing gaps. In all the simulations, the applied traveling-wave propagates from the left side to the right of the computational domain.



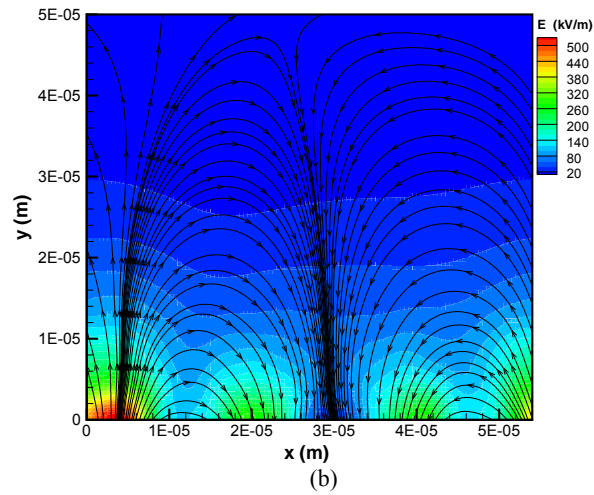


Figure 4. Solution of the electric field: (a) the electric potential ϕ and (b) the electric field E .

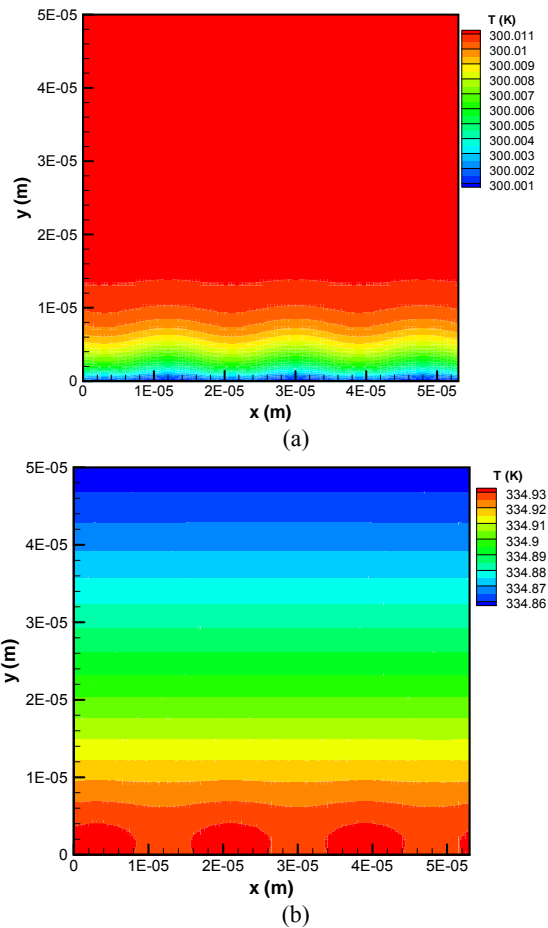


Figure 5. The temperature fields under (a) BC-1 and (b) BC-2 (at $V_0 = 10$ V and $f = 100$ kHz).

4.2. Electrohydrodynamics

Figure 5 presents the temperature distributions in the microchannel under the two different thermal boundary conditions. The frequency of the electric field is $f = 100$ kHz. In both cases, Joule heating is concentrated near the electrodes where the field strengths are at the maximum. Under BC-1, the maximum temperature is found near the top of the microchannel due to poor thermal conductivity of the glass cover. In contrast, the highest fluid temperature under BC-2 occurs in the region close to the electrodes, since the convection thermal resistances are equal on both the top and the bottom surfaces of the microchannel. It is noted that the temperature variation across the microchannel height is minuscule (~ 0.01 K), however, the resulting temperature gradient is sufficient (200 K/m) to induce EHD flows [25].

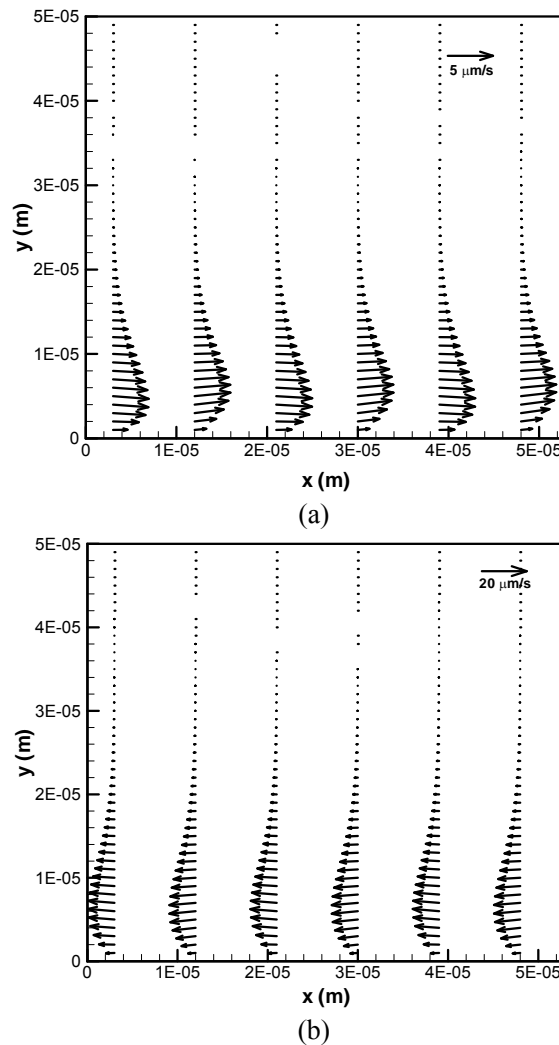


Figure 6. The EHD velocity vectors at various streamwise locations under (a) BC-1 and (b) BC-2 ($V_0 = 10$ V and $f = 100$ kHz).

Figure 6 illustrates the calculated EHD velocity vectors at various streamwise locations. As expected, attraction-type EHD occurs under BC-1 and the flow velocity follows the direction of the traveling wave (Figure 6(a)), i.e., going from the left to right, whereas repulsion-type EHD arises under BC-2 and the flow is against the traveling wave (Figure 6(b)). Figure 7 illustrates the comparison of the EHD velocity for three different frequencies at the midway location of the flow channel ($x = 30 \mu\text{m}$). It is known that the maximum EHD effect occurs at the relaxation frequency of the KCl solution, $f_c = 122 \text{ kHz}$. At lower frequencies, the induced charges will decay during the long residence time and the EHD force exerted in the fluid is small. If the frequency is too high, the charges will not be able to fully transit from one electrode to the next before the voltages on the electrodes change, again reducing the EHD force [14].

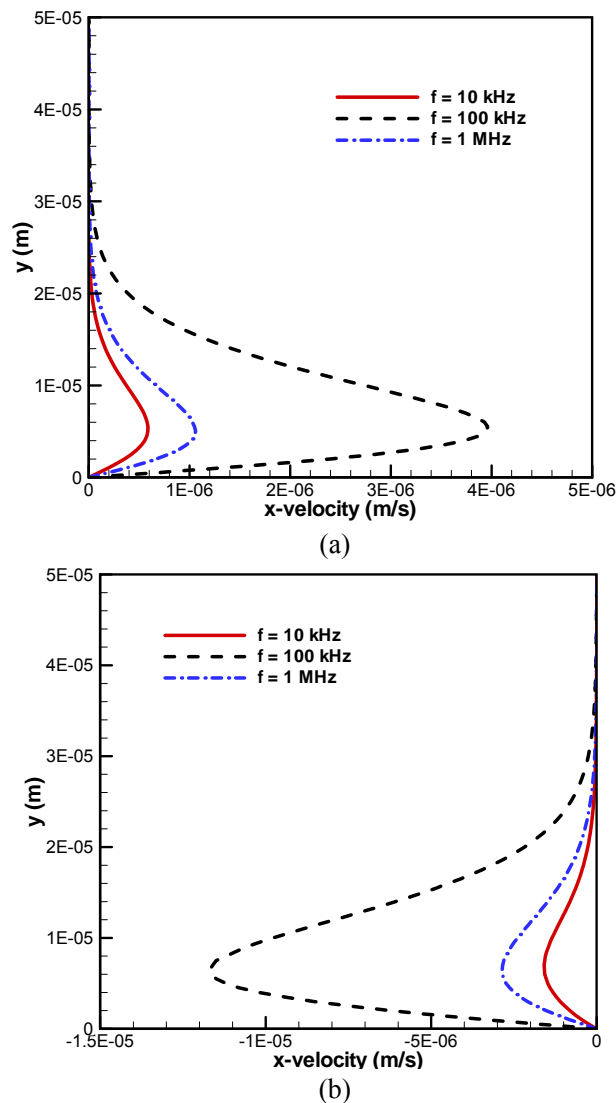


Figure 7. Comparison of the EHD velocity at the streamwise location $x = 30 \mu\text{m}$ at different frequencies under (a) BC-1 and (b) BC-2 ($V_0 = 10 \text{ V}$).

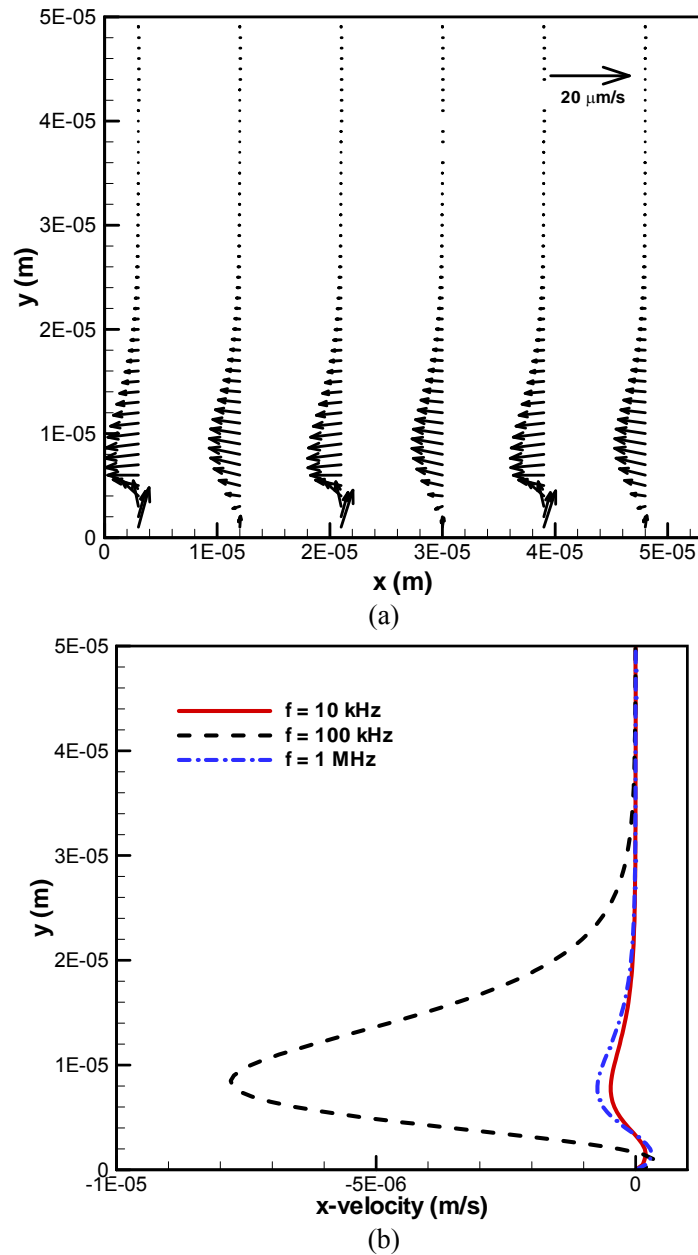


Figure 8. (a) The twDEP velocity vector field at various streamwise locations and (b) the twDEP velocity profile at the streamwise location $x = 30 \mu\text{m}$ at different frequencies.

The results in Figure 7 show that, in both repulsion-type and attraction-type EHD, the fluid velocity rises up drastically when the frequency is increased from 10 kHz to 100 kHz (close to the optimal frequency of 122 kHz), and decreases rapidly with further increasing the frequency to 1 MHz. The maximum velocity in the repulsion-type EHD ($\sim 12 \mu\text{m/s}$) is about three times that in the attraction-type EHD ($\sim 4 \mu\text{m/s}$). This is consistent with the greater temperature gradient observed under BC-2 (as shown in Figure 5), which leads to a stronger EHD driving force.

4.3. Dielectrophoresis

The DEP-induced velocity fields in the microchannel are shown in Figure 8(a). Since $\text{Im}(f_{\text{CM}}) < 0$, the DEP flow is opposite to the direction of the traveling wave. Velocity profiles at various streamwise locations resemble the asymmetric shape of the EHD flows, however, reverse flows are found in the near-wall area. Flow velocities at $x = 30 \mu\text{m}$ are plotted in Figure 8(b) for the applied frequencies of 10 kHz, 100 kHz and 1 MHz, respectively. It can be seen that the maximum velocity occurs at $f = 100 \text{ kHz}$, which is close to the Maxwell-Wagner relaxation frequency, $f_{\text{M-W}} = 126 \text{ kHz}$ for the fluid-particle combination used in this work. The velocity reductions at the lower and higher frequencies (10 kHz and 1 MHz) are due to the decreased values of $\text{Im}(f_{\text{CM}})$ in both frequency ranges (as shown in Figure 1).

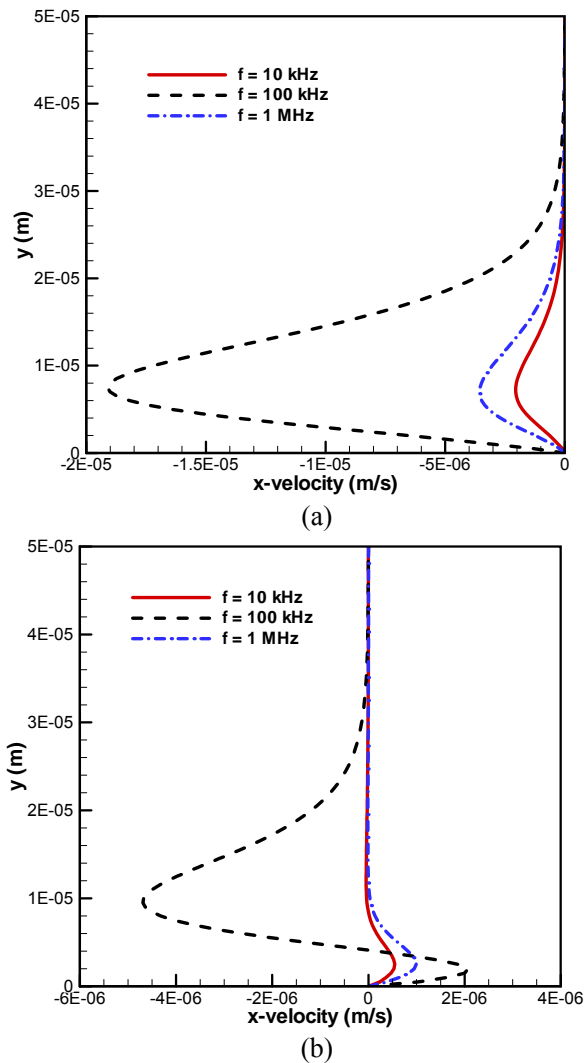


Figure 9. Velocity profile at the streamwise location $x = 30 \mu\text{m}$ when EHD interferes with twDEP: (a) twDEP + repulsion-type EHD and (b) twDEP + attraction-type EHD.

4.4. EHD and twDEP

The simulation results in Figure 7 and Figure 8 suggest that EHD and twDEP operating in the same frequency range can simultaneously induce flow fields of a comparable velocity magnitude. The direction of the net flow depends on the relative directions of the individual flows with respect to that of the applied field. Figure 9 shows the velocity profile at the streamwise location $x = 30 \mu\text{m}$ when the DEP-induced and EHD-induced flow fields are superimposed.

In Figure 9(a), the repulsion-type EHD and the twDEP act in the same direction (from the right to left), both contributing synergistically to the net flow. This is evidenced by the increase in the maximum velocity at all three frequencies.

Figure 9(b) depicts that, when the attraction-type EHD competes with the twDEP, the net flow field will be suppressed. For instance, at $f = 100 \text{ kHz}$, the maximum twDEP velocity reduce from $8 \mu\text{m/s}$ (Figure 8(b)) to $5.5 \mu\text{m/s}$; moreover, the twDEP flow directions are totally reversed at $f = 10 \text{ kHz}$ and 1 MHz . As a consequence, when utilizing twDEP for particle manipulation or micropumping, great caution must be exercised to ensure both the frequency range of the traveling-wave field and the thermal boundary condition of the microfluidic device are appropriate so that the effects of EHD will not interfere obstructively with twDEP.

Additionally, it is noted that the DEP flow may alter the temperature distribution in the microchannel and, therefore, influence the velocity profile of the EHD flow. For conditions considered in this work, however, the Peclet number (which characterizes the relative importance of advection to conduction in determining the temperature field and is defined as $Pe \equiv L \cdot U / \alpha$ where L is the characteristic length of the flow $\sim 2h = 100 \mu\text{m}$, U the characteristic velocity $\sim 10 \mu\text{m/s}$, and α the thermal diffusivity $\sim 1.4 \times 10^{-7} \text{ m}^2/\text{s}$) is estimated to be only about 0.007. Thus, the impact of DEP flow on EHD via advection effect can be safely neglected.

CONCLUSION

In this paper, the coupled EHD- and twDEP-driven flows were studied numerically in a microchannel. The EHD flow was caused by the Joule heating effect in the electrolyte solution.

Both the repulsion-type EHD and the attraction-type EHD were considered, each determined by the corresponding thermal boundary condition. The flow field due to twDEP was solved using an equivalent mixture model and the calculated flow velocity was compared to that induced by EHD. The results show, depending on the frequency range of the traveling-wave field and the thermal boundary condition, the EHD-induced flow and the twDEP-induced flow can work either synergistically or competitively.

ACKNOWLEDGMENTS

The authors would like to acknowledge the financial support from the National Science Foundation (Grant No. 0927340 and Grant No.1134119).

REFERENCES

- [1] J. Z. Hilt, N. A. Peppas, Microfabricated drug delivery devices, *International Journal of Pharmaceutics* 306 (2005) 15-23.
- [2] H. R. Sahoo, J. G. Kralj, K. F. Jensen, Multistep continuous-flow microchemical synthesis involving multiple reactions and separations, *Angewandte Chemie-International Edition* 46 (2007) 5704-5708.
- [3] D. Erickson, D. Q. Li, Integrated microfluidic devices, *Analytica Chimica Acta* 507 (2004) 11-26.
- [4] V. Singhal, S. V. Garimella, Induction electrohydrodynamics micropump for high heat flux cooling, *Sensors and Actuators A: Physical* 134 (2007) 650-659.
- [5] B. D. Iverson, S. V. Garimella, Recent advances in microscale pumping technologies: a review and evaluation, *Microfluidics and Nanofluidics* 5 (2008) 145-174.
- [6] V. Singhal, S. V. Garimella, A. Raman, Microscale pumping technologies for microchannel cooling systems, *Applied Mechanics Reviews* 57 (2004) 191-221.
- [7] B. P. Cahill, L. J. Heyderman, J. Gobrecht, A. Stemmer, Electro-osmotic pumping on application of phase-shifted signals to interdigitated electrodes, *Sensors and Actuators B: Chemical* 110 (2005) 157-163.
- [8] Ramos, H. Morgan, N. G. Green, A. Gonzalez, A. Castellanos, Pumping of liquids with traveling-wave electroosmosis, *Journal of Applied Physics* 97 (2005) 084906 - 084906-8.
- [9] D. Liu, S. V. Garimella, Microfluidic pumping based on traveling-wave dielectrophoresis, *Nanoscale and Microscale Thermophysical Engineering* 13 (2009) 109-133.
- [10] D. B. Go, S. V. Garimella, T. S. Fisher, R. K. Mongia, Ionic winds for locally enhanced cooling, *Journal of Applied Physics* 102 (2007) 053302 - 053302-8.
- [11] V. Singhal, S. V. Garimella, A novel valveless micropump with electrohydrodynamic enhancement for high heat flux cooling, *IEEE Transactions on Advanced Packaging* 28 (2005) 216-230.
- [12] W. Zhang, T. S. Fisher, S. V. Garimella, Simulation of ion generation and breakdown in atmospheric air, *Journal of Applied Physics* 96 (2004) 6066-6072.
- [13] Ramos, H. Morgan, N. G. Green, A. Castellanos, AC electric-field-induced fluid flow in microelectrodes, *Journal of Colloid and Interface Science* 217 (1999) 420-422.
- [14] D. Iverson, L. Cremaschi, S. V. Garimella, Effects of discrete-electrode configuration on traveling-wave electrohydrodynamic pumping, *Microfluidics and Nanofluidics* 6 (2009) 221-230.
- [15] H. Pohl, The motion and precipitation of suspensoids in divergent electric fields, *Journal of Applied Physics* 22 (1951) 869-871.
- [16] J. R. Melcher, Traveling-wave induced electroconvection, *Physics of Fluids* 9 (1966) 1548-1555.
- [17] J. R. Melcher, M. S. Firebaugh, Traveling-wave bulk electroconvection induced across a temperature gradient, *The Physics of Fluids* 10 (1967) 1178 - 1185.
- [18] H. Morgan, A. G. Izquierdo, D. Bakewell, N. G. Green, A. Ramos, The dielectrophoretic and travelling wave forces generated by interdigitated electrode

- arrays: analytical solution using Fourier series, *Journal of Physics D: Applied Physics* 34 (2001) 2708-2708.
- [19] J. Seyed-Yagoobi, J. E. Bryan, Enhancement of heat transfer and mass transport in thermal equipment with electrohydrodynamics, *Electrostatics*, 1999, pp. 127-130.
- [20] M. Yazdani, J. Seyed-Yagoobi, Heat transfer augmentation of parallel flows by means of electric conduction phenomenon in macro- and Microscales, *Journal of Heat Transfer-Transactions of the ASME* 132 (2010) 062402 - 062402-9.
- [21] M. Yazdani, J. Seyed-Yagoobi, An electrically driven impinging liquid jet for direct cooling of heated surfaces, *Ieee Transactions on Industry Applications* 46 (2010) 650-658.
- [22] M. Lian, J. Wu, Microfluidic flow reversal at low frequency by AC electrothermal effect, *Microfluidics and Nanofluidics* 7 (2009) 757-765.
- [23] Ramos, H. Morgan, N. G. Green, A. Castellanos, AC electrokinetics: a review of forces in microelectrode structures, *Journal of Physics D: Applied Physics* 31 (1998) 2338-2353.
- [24] J. A. Stratton, *Electromagnetic Theory*, McGraw-Hill, New York, 1941.
- [25] N. G. Green, A. Ramos, A. Gonzalez, A. Castellanos, H. Morgan, Electrothermally induced fluid flow on microelectrodes, *Journal of Electrostatics* 53 (2001) 71-87.
- [26] H. Morgan, N. G. Green, *AC Electrokinetics: colloids and nanoparticles*, Research Studies Press Ltd 2003, pp. 49 – 60.
- [27] J. Happel, H. Brenner, *Low Reynolds Number Hydrodynamics*, Springer, 1983.
- [28] N. G. Green, A. Ramos, H. Morgan, Numerical solution of the dielectrophoretic and travelling wave forces for interdigitated electrode arrays using the finite element method, *Journal of Electrostatics* 56 (2002) 235-254.
- [29] P. S. Lee, S. V. Garimella, D. Liu, Investigation of heat transfer in rectangular microchannels, *International Journal of Heat and Mass Transfer* 48 (2005) 1688-1704.
- [30] F. P. Incropera, D. P. Dewitt, T. L. Bergman, A. S. Lavine, *Fundamentals of Heat and Mass Transfer*, John Wiley and Sons, Hoboken, 2005.
- [31] FLUENT 6 User's Guide, 2000.

Received 27 February 2012, received in revised form 17 July 2012; accepted 18 July 2012.

ONSET OF NUCLEATE BOILING AND CRITICAL HEAT FLUX WITH BOILING WATER IN MICROCHANNELS

*R. R. Bhide¹, S. G. Singh², Vijay S. Duryodhan¹,
Arunkumar Sridharan¹, and Amit Agrawal^{1,*}*

¹Indian Institute of Technology Bombay, Powai, Mumbai, India

²Indian Institute of Technology, Hyderabad, India

ABSTRACT

This paper focuses on experimental determination of onset of nucleate boiling (ONB) and critical heat flux (CHF) at the microscales, and comparison of these with available correlations. The working fluid is deionised water and microchannel of four different hydraulic diameters: 65, 70, 107 and 125 μm , have been tested. Effect of hydraulic diameter (65-125 μm), mass flux (60-1410 $\text{kg}/\text{m}^2\text{s}$) and heat flux (0-910 kW/m^2) on ONB and CHF has been studied in detail. The heat flux for onset of nucleate boiling increases with hydraulic diameter and mass flux. The critical heat flux tends to increase with a decrease in hydraulic diameter and with increasing mass flux. The effect of surface roughness on CHF has also been tested to a limited extent; no clear change in the CHF value was observed upon changing the surface roughness by an order of magnitude. The empirical correlations tested in this study predict the experimental data to varying extent. These results may help better determine the lower and upper limits of heat flux while designing heat sink for electronic cooling.

Keywords: Two phase flow, ONB, CHF, Boiling incipience

NOMENCLATURE

Symbol used	Description	Units
A	Area	m^2
C_p	Specific heat of the fluid	$\text{J}/\text{kg}\cdot\text{K}$
d_h	Hydraulic Diameter	m
H	Height of channel	m

* Corresponding author: Dr. Amit Agrawal, Department of Mechanical Engineering, Indian Institute of Technology Bombay, Powai Mumbai 400076, INDIA, Email: amit.agrawal@iitb.ac.in, Phone: +91-22-2576-7516, Fax: +91-22-2572-6875

h_{fg}	Latent heat of evaporation of fluid	J/kg
G	Mass flux	$\text{kg/m}^2\text{-s}$
L	Length in the microchannel	m
\dot{m}	Mass flow rate	kg/s
P	Power	W
ΔP	Pressure drop	mbar
q''	Heat flux	W/m^2
Q	Volumetric flow rate	m^3/s
T	Temperature	$^{\circ}\text{C}$
u	Velocity	m/s
W	Width of the microchannel	m
x	Quality	-
ε	Surface roughness	m
ρ	Density	kg/m^3
ρ_H	Homogenous Density	kg/m^3
v	Specific Volume	m^3/kg
μ	Viscosity	cP
σ	Surface Tension	N/m
Re	Reynolds Number	-
Fr_H	Froude Number	-
We_H	Weber Number	-

Subscript	Description
w	Wall
sat	Saturation
in	Inlet
exit	Exit
cross	Cross-sectional
h	Heated
air	Ambient
supp res	Supplied Reservoir
chan	Channel
pred	Predicted
expt	Experiment
f	Fluid
g	Vapour
tp	Two phase
sp	Single phase
i,f	Frictional Pressure drop
a,f	Acceleration Pressure drop
avg	Average
fo	Fluid only
go	Vapour only

1. INTRODUCTION

In the recent past, there has been an increasing trend to use miniaturised systems. The development of fabrication techniques and the advances in semiconductor technology have led to the development of miniaturised electronic components. These devices need to be maintained below a certain temperature for efficient working. Due to increased storage capacity, faster performance, the heat to be dissipated from electronic components has increased considerably. It has been found that dissipating heat fluxes greater than 100 W/cm^2 using conventional air cooling would be difficult. The use of microfluidic devices to remove high heat fluxes is thus being widely researched as a viable alternative. Apart from cooling of electronic components, the micro-thermal-mechanical systems can be used in portable computer chips, radar and aerospace avionics components, and in microchemical reactors [1].

A large amount of work has been devoted to the study of fluid flow and heat transfer mechanisms in microchannels. Specifically, researchers have concentrated on the prediction of flow patterns [2-6], heat transfer characteristics [4-9] and instability [5, 10-12] in two phase flow in microchannel. Singh et al. [13] found a strong dependence of two-phase pressure drop on aspect ratio in rectangular microchannel, with a minimum at an aspect ratio of about 1.6. Singh et al. [5] have reported the pressure drop in a $109 \mu\text{m}$ hydraulic diameter trapezoidal cross-section microchannel over a wide range of inlet mass flow rate and heat flux values. The pressure drop was found to exhibit a maximum with a reduction in mass flow rate for a constant heat flux. With a subsequent reduction in mass flow rate, the pressure drop rises rapidly. Their comprehensive data is further analyzed in this paper. This work was extended by Bhide et al. [12] to study mean and r.m.s. of pressure drop in sub-hundred sized microchannels. They found a reduction in pressure instabilities with a reduction in hydraulic diameter and increase in wall roughness. See Agrawal and Singh [36] and Singh et al. [37] for a recent review on flow boiling in microchannel.

Onset of nucleate boiling (ONB) and critical heat flux (CHF) are important issues in the study of two phase flow, especially in the design of microchannel heat sinks. Onset of nucleate boiling marks the beginning of the region of improved heat transfer. Several researchers [25-27] have developed correlations to predict ONB for flow boiling in conventional scale flow passages. Basu et al. [33] performed subcooled flow boiling experiments on conventional scale passages fabricated using copper plate and nine zircalloy rod bundle. They developed a correlation for heat flux and wall superheat required for bubble inception, and suggested that these parameters are dependent upon mass flow rate, liquid subcooling, and contact angle. Also, they developed a correlation for nucleation site density which is primarily dependent upon the contact angle. Qu and Mudawar [34] performed experiments on parallel microchannels to measure the incipient boiling heat flux. They developed a model to predict the incipient boiling heat flux, accounting for the complexities of bubble formation along the flat and corner regions of a rectangular flow microchannel. They have also accounted for the likelihood of bubbles growing sufficiently large to engulf the entire flow area of a microchannel. Liu et al. [35] experimentally investigated the onset of nucleate boiling and developed an analytical model to predict important parameters such as incipience heat flux, bubble size, etc. during ONB.

CHF is the maximum heat flux that can be applied to the heater surface without causing permanent damage to the device and therefore represents the upper limit for heat transfer in

two phase flow. CHF is the outcome of events that cause a sudden appreciable decrease in the heat transfer coefficient of a surface on which boiling is occurring. However, the value of CHF is seldom reported in literature because it is rather difficult to obtain – more so at the microscales. Qu and Mudawar [14] found that CHF increases with mass flux but does not depend on the inlet temperature. They attributed this to the vapour back flow due to the parallel channel instability which negated the effect of liquid subcooling. They developed a correlation from the data for water in rectangular microchannels and the data for R-113 in circular mini/ microchannel heat sinks available from their earlier study. They developed a correlation as a function of vapour and liquid densities, channel dimensions, and Weber number. Jiang et al. [7] carried out experiments for calculation of the CHF in microchannels of 40 and 80 μm hydraulic diameters. Although they did not carry out flow visualisation study, from the temperature data collected they postulated that the boiling mechanism may be different for smaller microchannels. They observed different trends in the streamwise temperature profile for microchannels of 40 μm and 80 μm hydraulic diameters at CHF conditions. For the case of 40 μm channel, they postulated that the bubble nucleation activity is suppressed and boiling takes place through forced convection vaporization. They concluded that the bubble dynamics mechanism is very different and that the mechanism of bubble growth may be completely suppressed in smaller microchannels. Some studies with working fluid other than water are also available; for example, Ribatski et al. [15] worked with refrigerants (R-134a and R-245fa) while Lee and Mudawar [16] used a dielectric fluid (HFE 7100). Following important points are noted from the CHF data reported in the literature: (i) The exit quality at which CHF occurs decreases by about 1.7 times for the two-fold increase in mass flux, and (ii) the correlations of Katto, Sudo and Mudawar suggest that CHF in microchannels is a weak function of inlet subcooling. However, the correlation of Mishima shows substantial dependence on inlet subcooling. CHF studies for refrigerant-123 are available in Refs. [17-19].

Kosar [20] used the annular flow model of Qu and Mudawar and mass deposition coefficient of Patankar and Puranik [21] to predict the value of CHF for both water and refrigerant. The model predicts the experimental data for water with a mean absolute error of 28.9%, and in most cases the model predicted a larger value of CHF than experimentally determined. The discrepancy was attributed to either presence of parallel channel instability which leads to pre-mature CHF, or large thickness of the microchannel wall which tends to make the wall temperature uniform thereby delaying CHF. Kuan and Kandlikar [18] investigated the effect of flow instabilities in six parallel rectangular microchannels, each having a cross-sectional area of $1054 \times 157 \mu\text{m}^2$. They postulated that the ratio of evaporation momentum to surface tension force is an important parameter. This formed the basis of theoretical analysis of flow boiling phenomena and theoretical CHF model is proposed using these underlying forces to predict CHF in microchannels. The proposed correlation agrees with the experimental data with a mean average error of 8.2% for water. Recently, Roday and Jensen [19] compared the data for water and R-123 with existing micro/microchannel correlations. They found that existing large-sized correlations do not predict CHF in microchannels. Therefore, they developed a new correlation in low-flow subcooled boiling situation from their experimental data. Chandraker et al. [22] pointed out that the mechanism of CHF even at the conventional scales is not well understood and needs careful investigation.

It is clear from the literature survey that very few experimental studies have reported the value of CHF. This study intends to partly fill this gap by providing data-points for four

different size microchannels and at different heat flux values. The obtained values are compared with available correlations. CHF is detected in the experiments by a sudden rise in temperature of the heater surface due to a decrease in the heat transfer coefficient. Literature available on ONB suggest that the bubble dynamics in microchannel differs from that in conventional scale passages, and therefore has an even greater impact on performance of microchannel based heat sinks. Also, it has been observed that there is lack of available data on effect of microchannel surface condition on ONB. Hence, data for the onset of boiling is also obtained and compared with existing empirical correlations.

2. EXPERIMENTAL SETUP AND DATA REDUCTION

2.1. Fabrication of Microchannels

The fabrication of microchannels is done in-house at IIT Bombay. The microchannels are fabricated on a 2-inch, $275 \pm 25 \mu\text{m}$ -thick, p-type, <100> double-side-polished silicon wafer. Trapezoidal microchannels of dimension $77 \mu\text{m} \times 270 \mu\text{m}$ (at the top) $\times 20\text{mm}$ (L) (yielding a width of $158 \mu\text{m}$ at the bottom and a hydraulic diameter of $107 \mu\text{m}$) are fabricated by a sequence of process steps. The size of reservoir at the two ends of the microchannel is $6 \text{ mm} \times 6 \text{ mm}$. Note that other hydraulic diameter trapezoidal microchannels such as $65 \mu\text{m}$, $70 \mu\text{m}$ and $125 \mu\text{m}$ have also been employed in this work. The surface roughness as determined using profilometer was found to be less than $0.1 \mu\text{m}$ for all microchannels (other than for $70 \mu\text{m}$ channel). The sealing of the microchannels with a quartz plate is a crucial step in fabrication and special care was taken to avoid leakage. A detailed description of microchannel fabrication is provided elsewhere [5, 6, 12, 13].

A multi-film stack of Ti-Pt is used to fabricate the microheater for controlled heat flux generation. Fabrication and characterization details are again mentioned in Ref. [13]. The resistance of the fabricated micro heater is found to be 445 ohm at room temperature.

The amount of subcooling at the inlet varies between 15 to $45 \text{ }^\circ\text{C}$, while the exit pressure is atmospheric (1 bar). The heat loss was calculated using the standard technique of supplying power to the test section without any flow of water. All the heat supplied in this case would be lost to the atmosphere. The surface temperature is monitored at the steady-state condition using four thermocouples, which probe different locations of the chip. Knowing the average surface temperature and the heat flux supplied, the average heat transfer coefficient for heat loss is obtained. This heat transfer coefficient in combination with the measured surface temperature for a given experimental run is used for subtracting the heat loss.

2.2. Experimental Setup

The schematic of the experimental setup is shown in Figure 1. The test section consists of the microchannel with a serpentine heater integrated on the back side of the silicon wafer. Heat is supplied by a DC power source (Keithley Sourcemeter, 2400 series). Deionised water is used as the working fluid; the water is vigorously boiled and then cooled to room temperature to remove dissolved air. The water is pumped through a peristaltic pump

(Masterflex Easyflow II EW-77200-50) at a predetermined flow rate which is maintained constant for a given data point. The flow rate through the system is given by the pump itself and has a range of 0.1-6 ml/min. The flow rate was independently checked by measuring the mass of the water collected over 10 minutes duration and weighed on a microbalance.

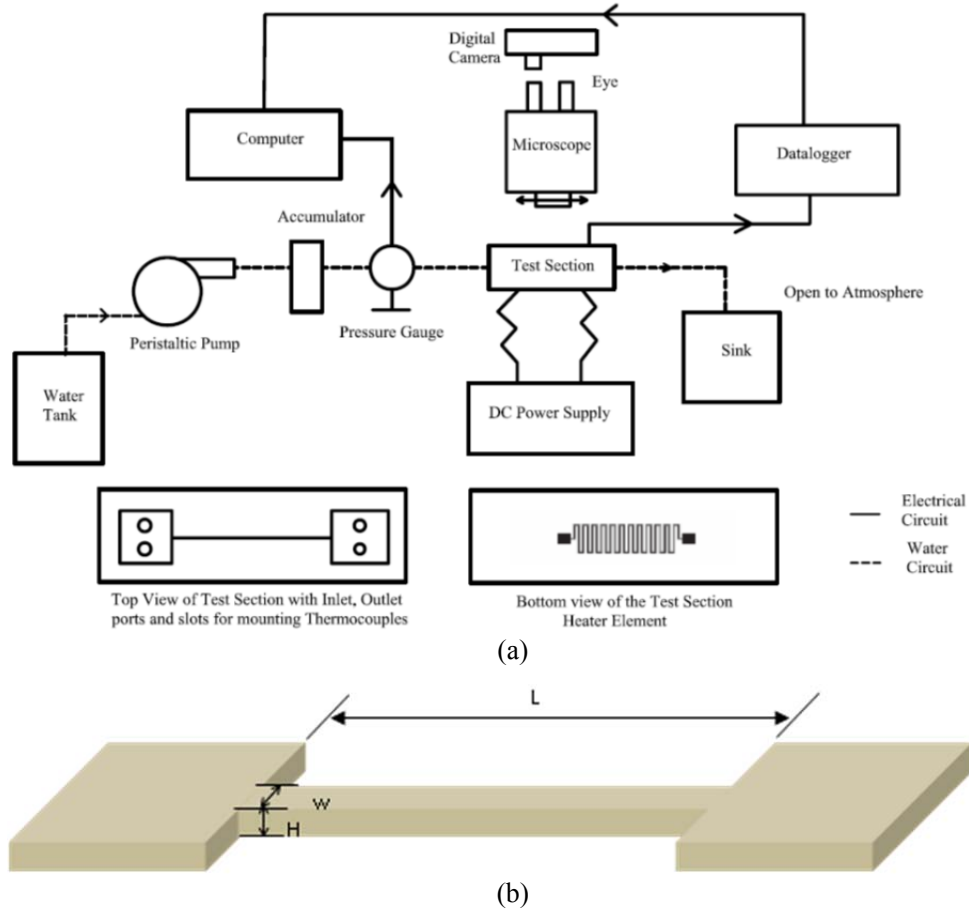


Figure 1. (a) Schematic of the experimental setup along with top and bottom view of the microchannel test section, (b) 3D view of microchannel geometry showing the measured geometrical parameters.

The microchannel has four ports, two at the inlet and two at the outlet. Two of these serve as entry and exit ports for the working fluid, and the remaining two are for inserting thermocouples (bead size of 0.5 mm, measurement accuracy ± 1 K, response time of 10 ms). Three equally-spaced K-type thermocouples (bead size 25 μm , measurement accuracy of ± 1 K, and response time of 1 ms) probe the surface temperature along the length of the microchannel. All the thermocouples used are connected to a data logger (Graphtec GL450) which collects data at 10 Hz frequency. A pre-calibrated digital pressure gauge (Keller, Leo 1 with a range of -1 to 3 bar, resolution of 0.05% of full scale, response time of 1 s) is connected at the inlet of the microchannel and provides the overall pressure drop (note that the pressure at the exit of the microchannel is atmospheric). The microchannel is oriented horizontally. The uncertainty in the different quantities, both measured and derived, is

provided in Table 1. The experimental setup has been carefully validated as discussed elsewhere [5, 12].

Table 1. Uncertainty for various parameters measured in the experiment

Parameter	Maximum error
\dot{Q}	0.01 ml/min
L	100 μm
W	0.5 μm
H	0.5 μm
P	0.02 W
T	0.5 $^{\circ}\text{C}$
ΔP	2 mbar
A_{Ch}	1.49 %
d_h	1.87 %
q''	5.54 %
P_{chan}	5.42 %

The following procedure is adopted for performing the experiments. The water reservoir is filled with de-gassed, deionized water and the micro-pump is set for the desired flow rate. The pressure drop, temperature of inlet and outlet, and flow rate values are measured simultaneously using the data logger. The pressure drop across the entire microchannel is measured, which includes entry and exit losses. The pressure drop due to expansion and contraction (at the entry and exit) is however estimated to be negligibly small (0.3%) as compared to the overall pressure drop. The microheater dc power supply was set for a predetermined heat flux value. The experiment is then repeated for different flow rates and heat fluxes. The experiments have been carried out on a single microchannel of different hydraulic diameters (65, 70, 107, and 125 μm) and 2 cm length. The flow rate has been varied from 0.1-0.5 ml/min corresponding to mass flux values of 60-1410 $\text{kg}/\text{m}^2\text{s}$. The power supplied is in the range of 0-7 W ($q'' = 0\text{-}91 \text{ W}/\text{cm}^2$). The maximum exit quality in these experiments is 0.6.

2.3. Data Reduction

Data like input power, inlet/outlet temperature, and mass flow rate obtained through measurement has been processed using following approach. Water enters the inlet reservoir at atmospheric temperature and gets heated. The power used to heat water in reservoir is:

$$P_{\text{reservoir}} = \dot{m} C_p (T_{\text{in}} - T_{\text{amb}}). \quad (1)$$

The heat gained by water at the inlet reservoir needs to be subtracted from the supplied power. This supplied power is directly obtained from the source meter. Therefore, power supplied to heat water in microchannel is given as,

$$P_{channel} = P_{supplied} (1 - \lambda) - P_{reservoir} \quad (2)$$

where, λ is the percentage of heat loss to the atmosphere. Microheater fabricated on the back side of the microchannel is uniformly distributed along the microchannel length. Therefore, Power per unit length of microchannel is given as,

$$q' = \frac{P_{channel}}{l} \quad (3)$$

The heat input to the microchannel is utilised for both sensible and latent heating of water. Thus, energy balance of the system gives the thermodynamic quality as,

$$x = \frac{q'l - \dot{m} C_p (T_{sat} - T_{in})}{h_{fg} \dot{m}} \quad (4)$$

Heat flux supplied to the microchannel is given

$$q'' = \frac{P_{channel}}{A_s} \quad (5)$$

where, A_s is the sum of the areas of side walls and the bottom wall. Mass flux is given as,

$$G = \frac{\dot{m}}{A_c} \quad (6)$$

where, A_c is the cross-sectional area of the microchannel.

3. ONSET OF NUCLEATE BOILING (ONB)

Apart from the pressure drop and heat transfer characteristics, the onset of nucleate boiling (ONB) and critical heat flux (CHF) are other two important parameters of concern to a thermal engineer.

The ONB point is basically the heat flux at which the bubble nucleation is initiated in the microchannel. In most cases subcooled boiling leads to ONB. The phenomenon of ONB is important because it marks an abrupt change from single phase flow to two phase flow. It is therefore the lower limit for heat sinks operating in two-phase regime and the upper limit for single-phase heat sinks.

3.1. Technique for Measurement of ONB

In these experiments, the onset of nucleate boiling was determined from the change in the slope of the pressure drop versus heat flux curves. These curves are for a fixed value of mass flow rate. In single phase, the pressure drop decreases with an increase in heat flux, which is due to reduction in viscosity of water with temperature. Upon ONB, bubbles appear along the microchannel length which leads to an increase in the overall pressure drop. Thus, the point of change of slope in the pressure drop versus heat flux curve is taken as the point of ONB (Figure 2). ONB can also be obtained from the boiling curves. The first change in slope of the boiling curve signifies the ONB point. The point from boiling curve agrees with data obtained independently from the pressure drop curves for all the cases (not shown).

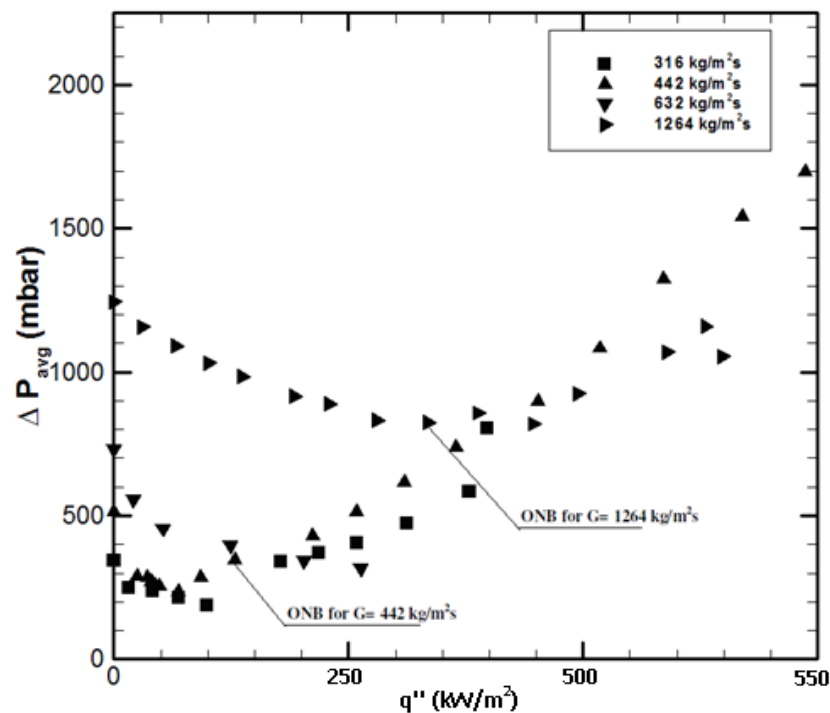


Figure 2. Variation of experimental pressure drop for different flow rates for 65 μm channel.

Figure 3 shows the variation of the ONB obtained experimentally with mass flux, in three different hydraulic diameter microchannels. For a given microchannel, the heat flux for ONB increases with an increase in mass flux, as expected. The heat flux required for ONB also increases with an increase in hydraulic diameter, for the same mass flux.

3.2. Comparison with ONB Correlations

The heat fluxes for ONB obtained experimentally are compared with different correlations. The comparison of the current dataset is limited to the correlations of Bergles

and Rohsenow [23] and Thom et al. [24]; these correlations are presented in Table 2. The heat flux required for ONB based on energy consideration, with $T_{sat} = 100^\circ\text{C}$ is calculated as,

$$q''_{boil} = \dot{m}C_p(T_{sat} - T_{in}) / A_h. \quad (7)$$

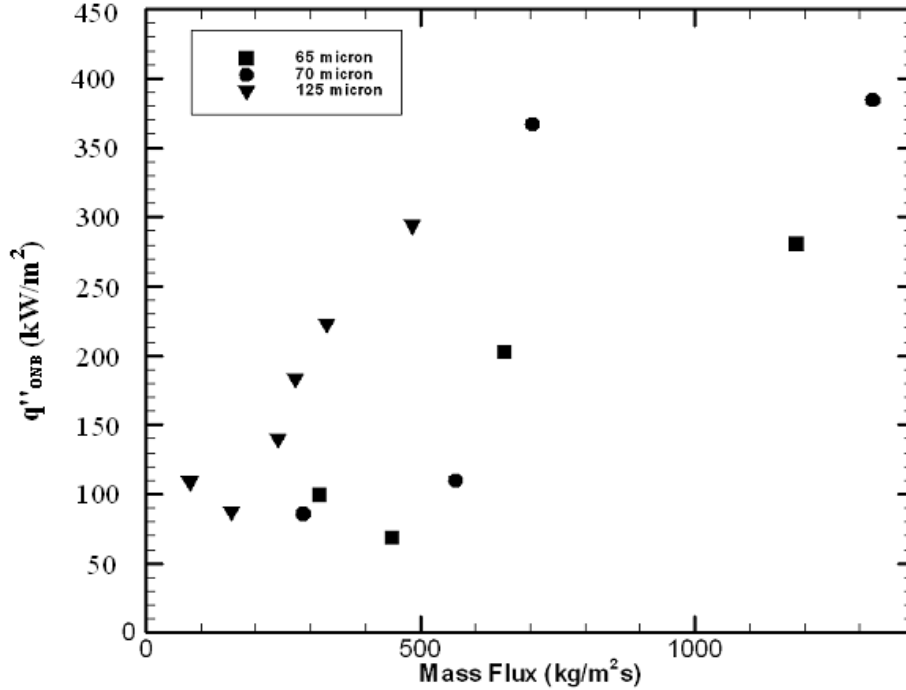


Figure 3. Variation of ONB with mass flux for different hydraulic diameters.

Note that most of the correlations for ONB are based on the work of Hsu [25]. The subsequent models of Sato and Matsumara [26], Davis and Anderson [27] and Kandlikar et al. [28] are of similar form but with a change in the empirical constants. These additional correlations were also tested in this work but were found to substantially over-predict most of the data-points; hence comparison with these correlations is not included here.

The comparisons with the aforementioned correlations are presented through Figs. 4, 5 and 6. Note that ratio of $q''_{predicted}$ to $q''_{experimental}$ as a function of mass flux is presented in the figures. The variation is largest with respect to the correlation of Thom et al. [24] (Figure 5). The correlation of Bergles and Rohsenow [23] also tends to over-predict the data (Figure 4). A relatively better match with the data (with most of the points lying within $\pm 50\%$) is found while comparing with q''_{boil} (Figure 6). On the whole, heat flux for ONB is predicted better at higher mass fluxes. Among all the correlations tested in this study, the simple energy balance calculation provides the best prediction. From Figs. 4-6 we note that the data for 125 μm channel is consistently over predicted by Thom et al. correlation as well as energy balance; but the energy balance method seems to fare better. For the 65 and 70 μm channel, Thom et al. correlation as well as energy balance under predicts the data. While simple energy balance show better prediction of ONB with increasing mass fluxes, Thom's correlation shows a

decreasing trend for $\frac{q''_{predicted}}{q''_{Expt}}$ with increasing mass flux. Interestingly, the correlation of Bergles and Rohsenow also shows a decreasing trend for $\frac{q''_{predicted}}{q''_{Expt}}$ with increased mass fluxes and the ratio approaches unity for higher mass fluxes.

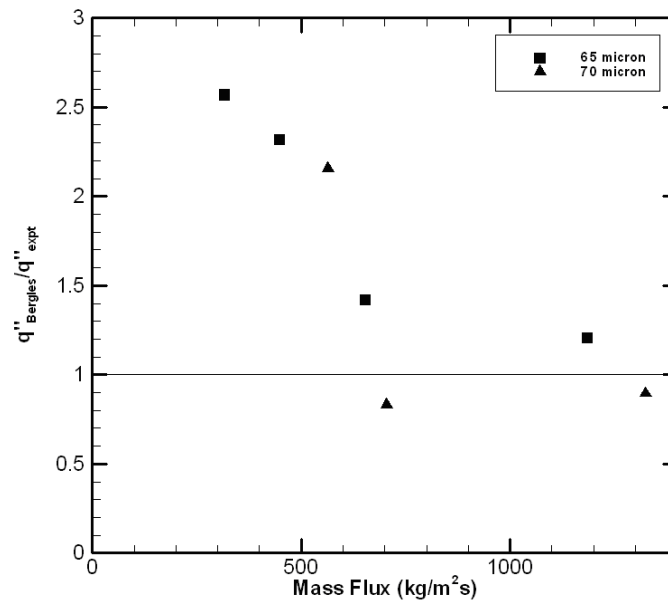


Figure 4. Comparison of ONB with the correlation of Bergles and Rohsenow [23].

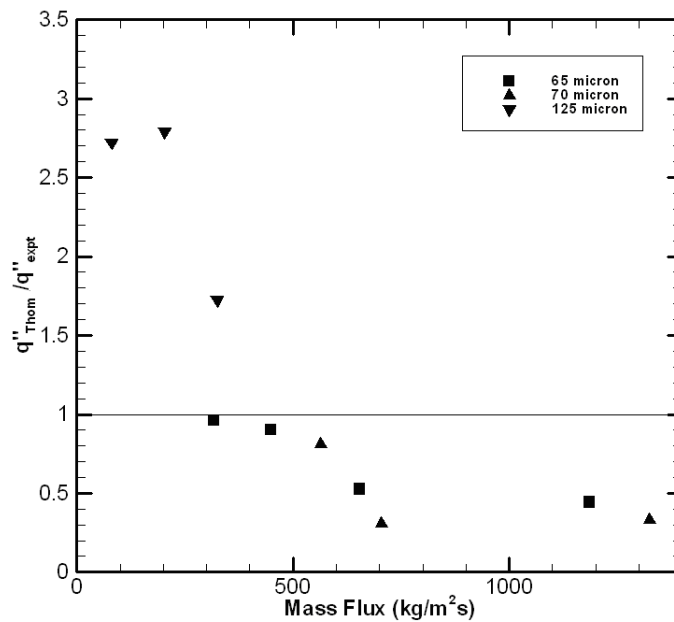


Figure 5. Comparison of ONB with the correlation of Thom et al. [24].

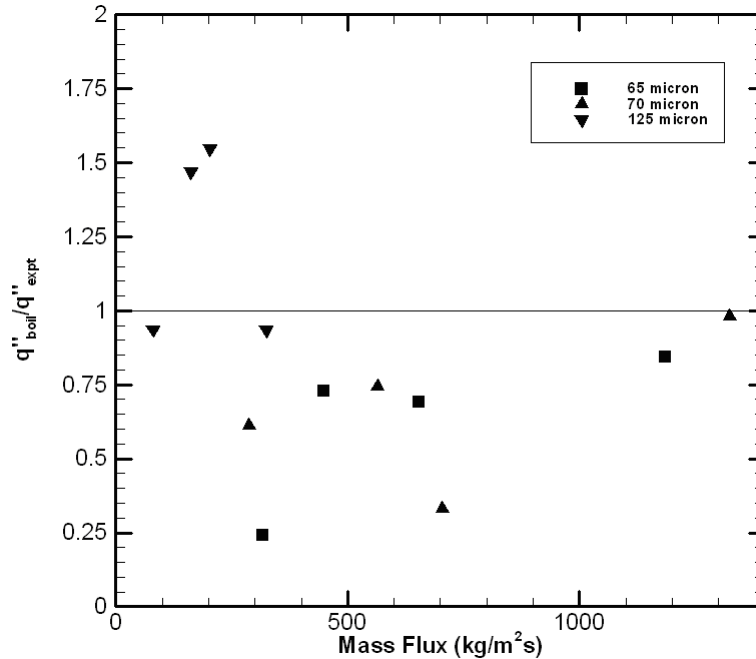


Figure 6. Comparison of ONB with q''_{boil} .

4. CRITICAL HEAT FLUX

Before moving on to the experimentally obtained CHF data (in Section 4.3), the procedure for determining CHF is discussed briefly in Sections 4.1 and 4.2.

4.1. CHF from Boiling Curves

CHF is estimated by plotting the boiling curve (heat flux versus surface temperature) (Figure 7a). While the first change in slope of the boiling curve indicates transition from single-phase to two-phase, the second change in slope occurs when the surface temperature increases rapidly owing to a drastic reduction in heat transfer coefficient. Thus, CHF corresponds to the point with a rapid increase in surface temperature.

Note that the two phase flow is accompanied by oscillations in temperature and pressure. From temperature-time plot, maximum, minimum and average temperatures can be determined. For example, in several cases the average surface temperatures may not be high (105-120 °C) while the peak temperatures may reach anywhere from 140-150 °C. Boiling curves with heat flux versus the maximum, minimum and average temperature are plotted and evaluated in Figure 7b. The figure shows that the CHF point is clearly obtained from plot of the maximum and average surface temperatures, while it is not so clear from the minimum temperature curve.

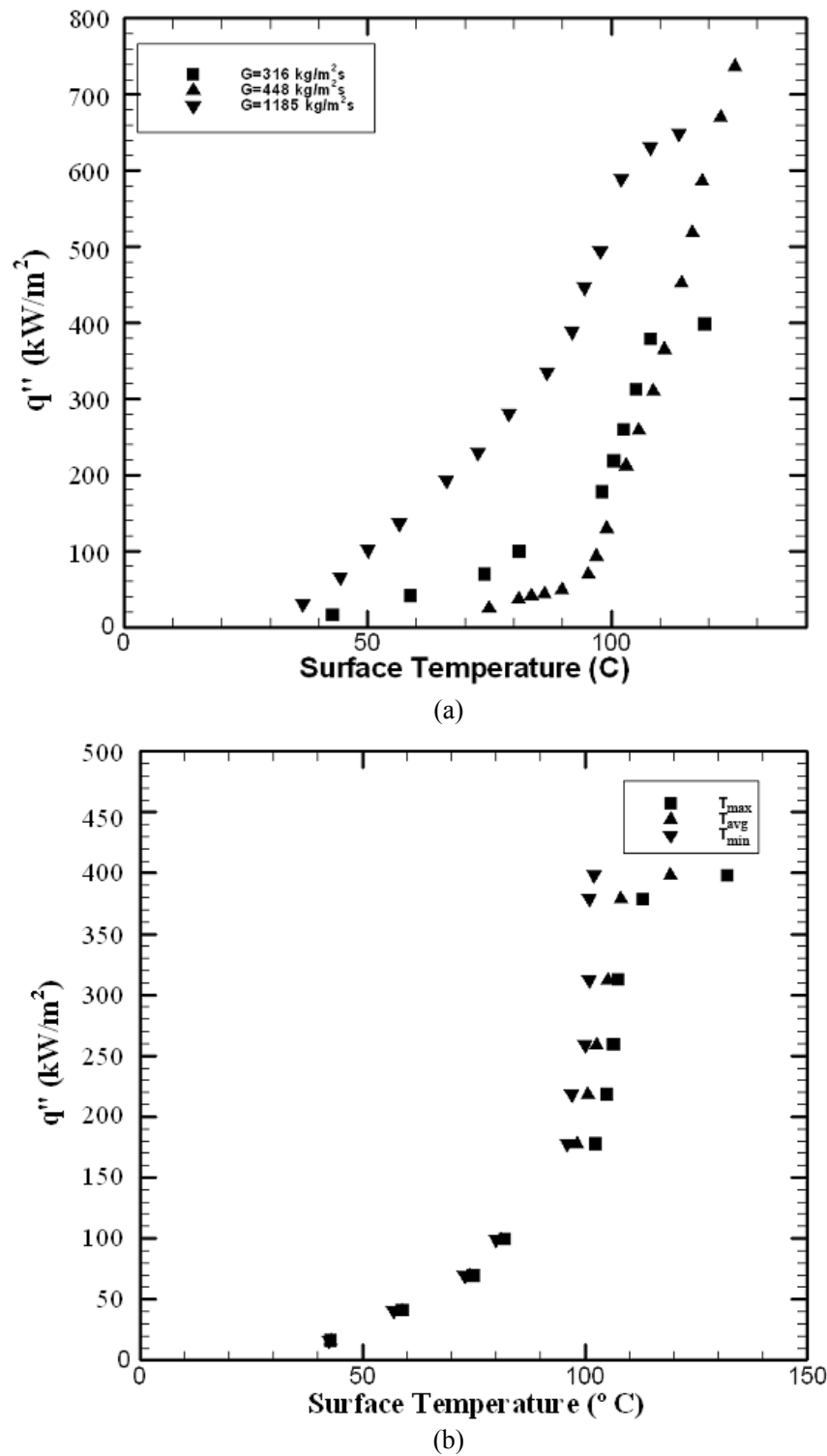


Figure 7. Boiling curve for 65 micron channel with (a) different mass flux values and (b) $G = 316$ kg/m²s with maximum, minimum and average temperatures.

4.2. CHF from Pressure Drop Curves

In these set of experiments, the heat flux is kept constant while the mass flux is systematically reduced. The curve shown in Figure 8a shows the typical variation of pressure drop [5]. The flow is initially in single phase region, which is represented by stars; with a reduction in flow rate the flow starts to boil, depicted by squares. The reason for this variation is discussed in sufficient detail in Singh et al. [5]. The heat flux corresponding to the sudden increase in pressure drop (point 'e' in Figure 8a) can be regarded as CHF for the particular value of mass flow rate. Note that the flow exhibits instability (i.e. the pressure varies rapidly with time). Singh et al. [5] and Bhide et al. [12] have quantified the variation in pressure with exit quality. In the former study, the normalized pressure (r.m.s. pressure by mean pressure) was found to be up to 14%. Further, the local maxima/ minima in normalized pressure were found to correlate very well with transitions in flow regime.

The above result is for a single heat flux value; a family of such curves was obtained, as shown in Figure 8b. The data obtained by Singh et al. [5] is unique because such detailed measurements on pressure drop, covering single-phase liquid, two-phase liquid-vapour and extending to dryout, are not available. In particular, Bergles and Kandlikar [29] have mentioned the difficulty in performing measurements in the regime d-e (in Figure 8a), highlighting that there is paucity of such data at the microscales. The CHF (estimated from point 'e') is influenced by the instabilities as pointed out by Bergles and Kandlikar [29]. It was specifically pointed out that microchannels with vaporization are prone to excursive instability which results in a relatively smaller value of CHF.

4.3. CHF Data and Comparison with Correlations

Note that instabilities are inherent in two-phase flow and no explicit attempt to suppress them has been made in this work. Quantification and discussion on the observed instabilities are provided elsewhere [5, 12]. The values reported here are therefore only indicative of the actual CHF.

The experimental CHF data points were obtained from one of the two methods discussed above (but not both) and plotted in Figure 9. Note that data from four different size microchannels is plotted in the figure. The CHF value increases with an increase in the mass flux (other than for $d_h = 125 \mu\text{m}$ case). For a given mass flux value, the CHF appears to increase with a decrease in hydraulic diameter. Note that the surface roughness of 65 and 70 μm microchannels at $\varepsilon/d_h = 0.0018$ and 0.0171, respectively, are different by approximately an order of magnitude [12]. However, the effect of surface roughness with approximately the same hydraulic diameter microchannel is not reflected in the CHF values. This may be owing to the fact that CHF occurs due to DNB (formation of vapour blanket) – as indicated by low quality values. The vapour layer may be such that it is thicker than the roughness elements on the tube surface, thereby masking the effect of surface roughness. Chandraker et al. [22] correlated the CHF data from the literature (at 9660 data points) to the underlying flow regime. They found that the CHF generally increases with mass flux in the churn/slug region; however, the CHF decreases with increase in mass flux in the annular region. The increase in CHF is attributed to the enhanced level of turbulence in the churn flow regime as the flow

rate is increased; this delays the occurrence of CHF [22]. On the other hand, in the annular flow regime the dryout mechanism is dictated by the entrainment and deposition of droplets on the liquid film. At higher flow rate in the annular regime the rate of droplet entrainment due to shearing at the liquid film-vapor interface increases, this causes early dryout and lower CHF values.

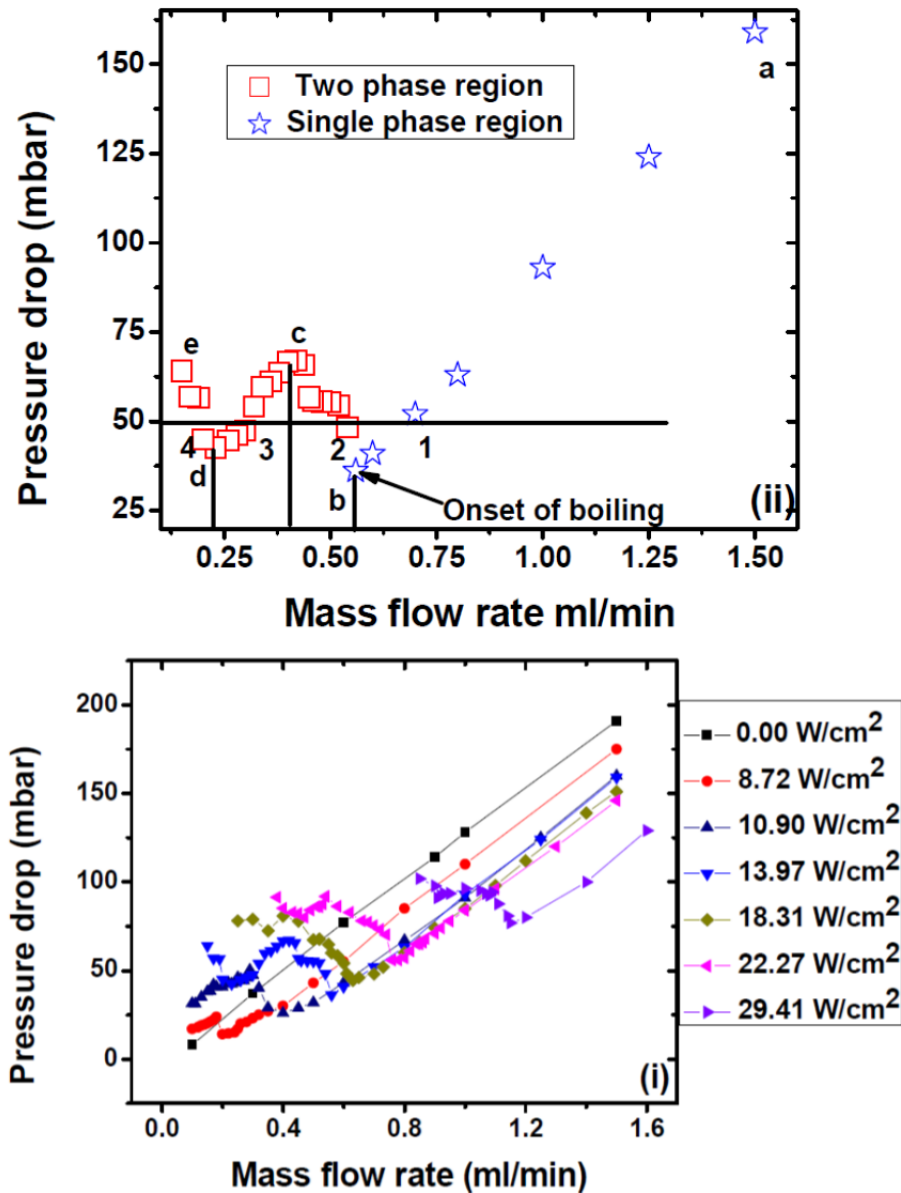


Figure 8. Experimental pressure drop versus mass flow rate for (a) heat flux of 13.97 W/cm² and (b) family of heat fluxes [5].

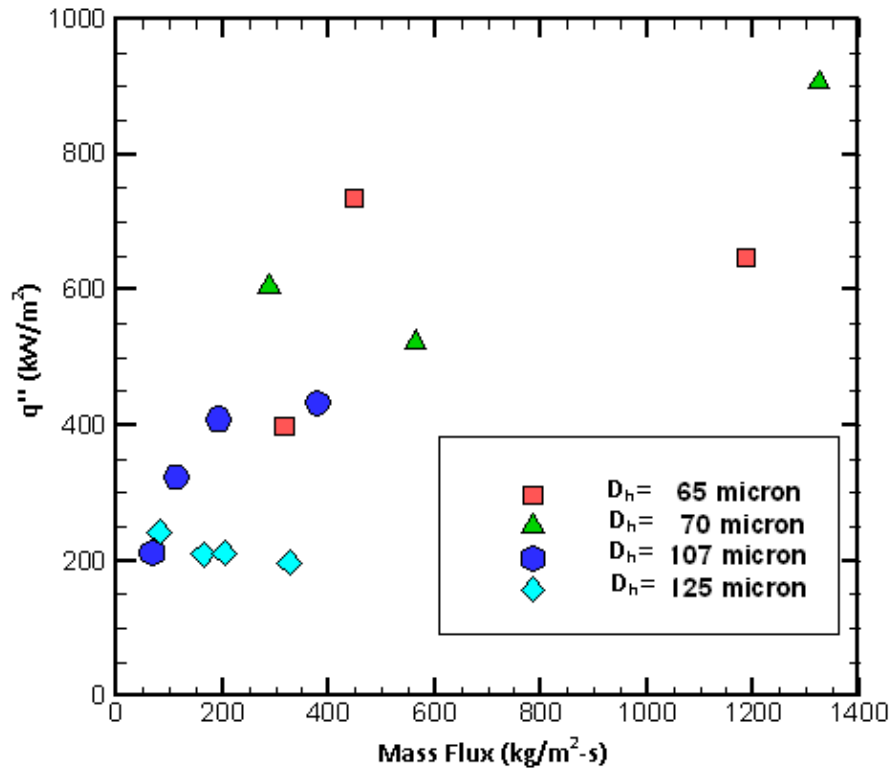


Figure 9. CHF versus mass flux.

Table 2. Correlations used for comparison with ONB

Bergles and Rohsenow [23]	$q''_{ONB} = 1082 P_{sat}^{1.156} [1.8(T_w - T_{sat})]^{2.16 / P_{sat}^{0.0234}} ;$ $P_{sat} \text{ in bar, } q''_{ONB} \text{ in MW/m}^2$
Thom et al. [24]	$q''_{ONB} = \left[\frac{\Delta T_{sat}}{22.65 \exp\left(-P_{sat}/87\right)} \right]^2 ;$ $P_{sat} \text{ in bar; } q''_{ONB} \text{ in MW/m}^2$
Single phase energy balance, q''_{boil}	$q''_{boil} = \frac{\dot{m} C_p (T_{sat} - T_{in})}{A_h}, T_{sat} = 100^\circ\text{C}$

Figure 9 shows an increasing trend in CHF with mass flux for all microchannels (other than 125 μm). The flow regime is however believed to be annular in all the cases [5, 12]. The result therefore suggests a change in the mechanism leading to CHF at the micro-scales. The mechanism of CHF is yet to be fully understood and calls for further detailed investigations.

Table 3. Correlations used for comparison with CHF

Qu and Mudawar [14]	$q''_{CHF} = 33.43 Gh_{fg} \left(\frac{\rho_g}{\rho_f} \right)^{1.11} We^{-0.21} \left(\frac{L}{d_h} \right)^{-0.36}$
Katto [30]	$q''_{CHF} = q''_{CHF,0} \left(1 + K \frac{\Delta h_{sub,in}}{h_{fg}} \right)$ $q''_{CHF,1} = 0.25 (Gh_{fg}) \frac{1}{L/d_h} \quad q''_{CHF,2} = C (Gh_{fg}) We^{-0.043} \frac{1}{L/d_h}$ $q''_{CHF,3} = 0.15 (Gh_{fg}) \left(\frac{\rho_g}{\rho_f} \right)^{0.133} We^{-1/3} \frac{1}{1 + 0.0077 L/d_h}$ $q''_{CHF,3} = 0.26 (Gh_{fg}) \left(\frac{\rho_g}{\rho_f} \right)^{0.133} We^{-0.433} \frac{\left(L/d_h \right)^{0.171}}{1 + 0.0077 L/d_h}$ <p>$C=0.25$ for $L/d_h < 50$; $C=0.34$ for $L/d_h > 50$</p> $K_1 = 1 ; K_2 = \frac{0.261}{CWe - 0.043} ; K_3 = \frac{0.556 \left(0.0308 + d_h/L \right)}{\left(\rho_g/\rho_f \right)^{0.133} We^{-1/3}}$ $q''_{CHF,1} < q''_{CHF,2} ; q''_{CHF,0} = q''_{CHF,1} ; K = K_1$ $q''_{CHF,1} > q''_{CHF,2} ; \text{if } q''_{CHF,2} < q''_{CHF,3} ; q''_{CHF,0} = q''_{CHF,2} ; K = K_2$ $q''_{CHF,2} > q''_{CHF,3} ; \text{if } q''_{CHF,3} < q''_{CHF,4} ; q''_{CHF,0} = q''_{CHF,3} ; K = K_3$ $q''_{CHF,3} > q''_{CHF,4} ; q''_{CHF,0} = q''_{CHF,4}$
Mishima and Ishii [31]	$q''_{CHF} = \frac{A_{cross}}{A_h} h_{fg} \left[\frac{G \Delta h_{sub,in}}{h_{fg}} + \left(\frac{1}{Co} - 0.11 \right) \sqrt{\rho_g g (\rho_f - \rho_g) d_h} \right]$ $Co = 1.35 - 0.35 \sqrt{\frac{\rho_g}{\rho_f}}$
Sudo et al. [32]	$q''_{CHF} = 0.005 h_{fg} G^{0.611} \left[\lambda \rho_g g (\rho_f - \rho_g) \right]^{0.195} \quad \lambda = \sqrt{\frac{\sigma}{(\rho_f - \rho_g) g}}$

Table 4. Comparison of q''_{\max} (expt) with different CHF correlations for various hydraulic diameters

Case I: Hydraulic diameter = 65 micron

Sr. No.	G (kg/m ² s)	Expt	Comparison with Correlations				Exit qlty	q''_{\max}/q''_{Mu}
		q''_{\max} (kW/m ²)	q''_{CHF} (kW/m ²) (Katto)	q''_{CHF} (kW/m ²) (Mishima)	q''_{CHF} (kW/m ²) (Sudo)	q''_{CHF} (kW/m ²) (Mudawar)		
1	316	398	668	152	637	398	0.37	1.00
2	448	736	672	224	788	488	0.55	1.51
3	1185	648	652	465	143	858	0.16	0.76

Case II: Hydraulic diameter = 70 micron

Sr. No.	G (kg/m ² s)	Expt	Comparison with Correlations				Exit qlty	q''_{\max}/q''_{Mu}
		q''_{\max} (kW/m ²)	q''_{CHF} (kW/m ²) (Katto)	q''_{CHF} (kW/m ²) (Mishima)	q''_{CHF} (kW/m ²) (Sudo)	q''_{CHF} (kW/m ²) (Mudawar)		
1	287	605	630	122	600	385	0.63	1.57
2	564	524	627	228	907	570	0.26	0.92
3	1324	907	610	450	1528	935	0.15	0.97

Case III: Hydraulic diameter = 107 micron

Sr. No.	G (kg/m ² s)	Expt	Comparison with Correlations				Exit qlty	q''_{\max}/q''_{Mu}
		q''_{\max} (kW/m ²)	q''_{CHF} (kW/m ²) (Katto)	q''_{CHF} (kW/m ²) (Mishima)	q''_{CHF} (kW/m ²) (Sudo)	q''_{CHF} (kW/m ²) (Mudawar)		
1	67	212	228	49	246	193	0.37	1.10
2	111	324	378	79	336	260	0.34	1.24
3	191	409	650	132	468	356	0.20	1.15
4	378	434	1270	232	710	529	0.07	0.82

Case IV: Hydraulic Diameter = 125 micron

Sr. No.	G (kg/m ² s)	Expt	Comparison with Correlations				Exit qlty	$q''_{\max} / q''_{\text{Mu}}$
		q''_{\max} (kW/m ²)	q''_{CHF} (kW/m ²) (Katto)	q''_{CHF} (kW/m ²) (Mishima)	q''_{CHF} (kW/m ²) (Sudo)	q''_{CHF} (kW/m ²) (Mudawar)		
1	81	243	307	33	277	226	0.47	1.08
2	163	210	623	72	424	338	0.20	0.62
3	203	212	775	86	486	385	0.16	0.55
4	325	197	1211	109	648	505	0.06	0.39

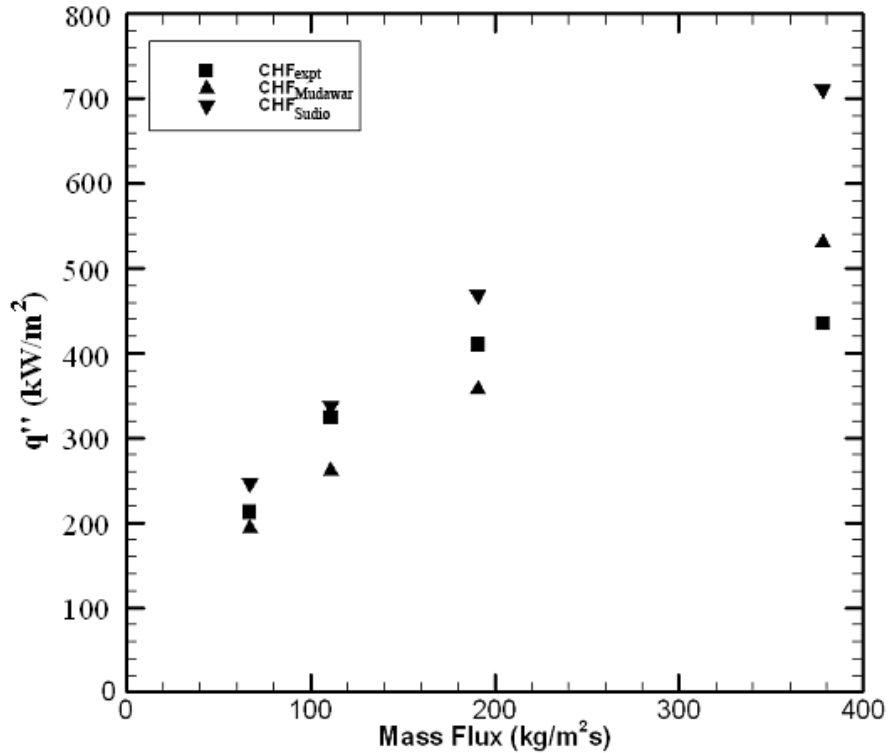


Figure 10. Comparison of CHF with the correlation of Sudo et al. [32] and Qu and Mudawar [14] for 107 μm channel.

The CHF value obtained experimentally is compared with the correlations of Katto [30], Mishima and Ishii [31], Sudo et al. [32] and Qu and Mudawar [14]. These correlations are tabulated in Table 3. Figure 10 and Table 4 provide a comparison of predicted and experimental values. Of the correlations tested, the correlation of Qu and Mudawar is for microscales while the other correlations are for conventional (macro) scale. It is seen from Table 4 that the CHF values obtained from the correlation of Qu and Mudawar compares with the experimental data better than the other tested correlations. In general, the correlation of Katto over-predicts the CHF data, while the correlation of Mishima under-predicts. A similar observation has been reported by Qu and Mudawar [14]. The correlation of Sudo et al. predicts the CHF data reasonably well; this correlation was however developed for flow in vertical rectangular channels.

DISCUSSION AND CONCLUSION

Experimental heat flux values for onset of nucleate boiling and critical heat flux are reported in this paper, as a function of mass flux and hydraulic diameter. The primary goal of this work is to add data points to the existing literature on microchannels, so that a more appropriate correlation for CHF at the microscales can eventually emerge. The obtained range of ONB and CHF are 50-400 kW/m^2 and 200-900 kW/m^2 , respectively, with hydraulic diameter in the range of 65-125 μm and mass flux in the range of 60-1410 $\text{kg/m}^2\text{-s}$. The CHF

is obtained from the boiling curve where a distinct increase in surface temperature occurs for a comparatively small increase in the applied heat flux. Alternatively, the CHF is obtained from the pressure drop curves in the two phase region, where backflow was observed. The CHF points are accompanied by fluctuations in pressure and temperature, and are responsible for premature CHF in microchannels. In several cases the average surface temperatures may not be high (105-120°C) while the peak temperatures may reach anywhere from 140-150°C. Such high temperatures though observed intermittently, can cause serious damage to the device.

Besides providing ONB and CHF data in extremely small channels, this paper also provides comparison with different correlations. In particular, the experimental CHF values are found to compare within $\pm 25\%$ with the correlation of Qu and Mudawar [14]. This correlation has been developed specially from microchannel database for CHF obtained from experiments done on water and R-113. It is needless to emphasize that the CHF data points are difficult to obtain and are rarely reported in the literature especially in the context of microchannels. The generation of CHF data is important as the occurrence of CHF is an important design consideration in two phase microchannel heat sinks. These results therefore provide useful lower and upper limits on heat flux to maintain two phase flow regime in microchannels.

ACKNOWLEDGMENTS

We are grateful to Mr. Anshul Jain for some initial calculations.

REFERENCES

- [1] J.R. Thome, Boiling in microchannels: a review of experiment and theory, *Int. J. Heat and Fluid Flow* 25 (2004) 128-139.
- [2] M Lee, Y. Y. Wong, M. Wong, Y. Zohar, Size and shape effects on two phase flow patterns in microchannel forced convection boiling, *Journal of Micromechanics and Microengineering*, 13 (2003) 155-164.
- [3] W. Qu, I. Mudawar, Flow boiling heat transfer in two-phase micro-channel heat sinks—-I. Experimental investigation and assessment of correlation methods, *Int. J. Heat Mass Transfer* 46 (2003) 2755-2771.
- [4] L. Zhang, J.M. Koo, L. Jiang, M. Asheghi, K.E. Goodson, J.G. Santiago, T. W. Kenny, Measurements and modelling of two phase flow in microchannels with nearly constant heat flux boundary conditions, *J. Microelectromechanical Systems*, 11 (2002) 12-19.
- [5] S.G. Singh, R. Bhide, B. Puranik, S.P. Dutttagupta, A. Agrawal, Two-phase flow pressure drop characteristics in trapezoidal silicon microchannels, *IEEE Transactions of Components and Packaging Technology*, 32 (2009) 887-900.
- [6] S. G. Singh, A. Jain, A. Sridharan, S. P. Dutttagupta, A. Agrawal, Flow map and measurement of void fraction and heat transfer coefficient using image analysis technique for flow boiling of water in silicon microchannel, *J. Micromech. Microeng.*, 19 (2009) 075004.

-
- [7] L. Jiang, M. Wong, Y. Zohar, Phase change in microchannel heat sinks with integrated temperature sensors, *J. of Microelectromechanical systems*, 8 (1999) 358-365.
- [8] M.E. Steinke, S.G. Kandlikar, An Experimental Investigation of Flow Boiling Characteristics of Water in Parallel Microchannels, *Transactions of ASME*, 126 (2004), 518-526.
- [9] G. Hestroni, A. Mosyak, E. Pogrebnyak, Z. Segal, Periodic boiling in parallel micro-channels at low vapour quality, *Int. J. Multiphase flow*, 32 (2006) 1141-1159.
- [10] H.Y. Wu and P. Cheng, Boiling instability in parallel silicon microchannels at different heat flux, *Int. J. of Heat and Mass Transfer*, 47 (2004), 3631-3641.
- [11] G. Hestroni, A. Mosyak, E. Pogrebnyak, Z. Segal, Explosive boiling of water in parallel micro-channels, *Int. J. Multiphase Flow*, 31 (2005) 371-392.
- [12] R.R. Bhide, S.G. Singh, A. Sridharan, S.P. Duttagupta, A. Agrawal, Pressure drop and heat transfer characteristics of boiling water in sub-hundred micron channel, *Experimental Thermal and Fluid Science*, 33 (2009) 963-975.
- [13] S.G. Singh, A. Kulkarni, S.P. Duttagupta, B.P. Puranik, A. Agrawal, Impact of aspect ratio on flow boiling of water in rectangular microchannels, *Experimental Thermal and Fluid Science* 33 (2008) 153–160.
- [14] W. Qu, I Mudawar, Measurement and correlation of critical heat flux in two-phase micro-channel heat sinks, *International Journal of Heat and Mass Transfer* 47 (2004) 2045–2059.
- [15] L. Wojtan, R. Revellin, J.R. Thome, Investigation of saturated critical heat flux in a single, uniformly heat microchannel, *Experimental Thermal and Fluid Science*, 30 (2006) 765-774.
- [16] J. Lee, I. Mudawar, Critical heat flux for subcooled flow boiling in micro-channel heat sinks, *International Journal of Heat and Mass Transfer*, 52 (2009) 3341-3352.
- [17] Kosar, and Y. Peles, Critical Heat Flux of R-123 in Silicon-Based Microchannels, *Journal of Heat Transfer*, 129 (2007) 844-851.
- [18] W.K. Kuan, and S.G. Kandlikar, Experimental Study and Model on Critical Heat Flux of Refrigerant-123 and Water in Microchannels, *Journal of Heat Transfer*, 130 (2008) 034503.
- [19] A.P. Roday, and M.K. Jensen, Study of the Critical Heat Flux Condition with Water and R-123 During Flow Boiling in Microtubes. Part I: Experimental Results and Discussion of Parametric Effects, *Int. J. Heat Mass Trans.*, 52 (2009) 3235-3249.
- [20] Kosar, A model to predict saturated critical heat flux in minichannels and microchannels. *Int. J. of Thermal Sciences* 48 (2009) 261-270.
- [21] P.U. Patankar, B.P. Puranik, Modifications and extensions to the annular flow model, in Proceedings of the Fourth International Conference on Nanchannels, Microchannels, and Minichannels, Limerick, Ireland, ICNMM2006-96053 (2006).
- [22] D.K. Chandraker, P.K. Vijayan, D. Saha and R.K. Sinha, Investigation on the characteristic of CHF in various flow pattern regimes based on look-up table data, *Nuclear Engineering Design*, 238 (2008), 170–177.
- [23] A.E. Bergles, W.M. Rohsenow, The determination of forced-convection surface-boiling heat transfer, *J. Heat Transfer* 86 (1964) 365–372
- [24] J.R.S. Thom, W.M. Walker, T.A. Fallon, and G.F.S. Reising, Boiling in subcooled water during flow up heated tubes or annuli. Symposium on Boiling Heat Transfer in

- Steam Generating Units and Heat Exchangers, Manchester, 15-16 September 1965. IMechE, London (1965).
- [25] Y.Y. Hsu, On the size range of active nucleation cavities on a heating surface, *J. Heat Transfer* 84 (1962) 207–216.
- [26] T. Sato, H. Matsumura, On the conditions of incipient subcooled-boiling with forced convection, *Bull. JSME* 7 (1963) 392–398.
- [27] E.J. Davis, G.H. Anderson, The incipience of nucleate boiling in forced convection flow, *AIChE J.* 12 (1966) 774–780.
- [28] S.G. Kandlikar, V. Mizo, M. Cartwright, E. Ikenze, Bubble nucleation and growth characteristics in subcooled flow boiling of water. National Heat Transfer Conference, HTD-342, *ASME*, 1997, 11–18.
- [29] E. Bergles, S.G. Kandlikar, On the Nature of Critical Heat Flux in microchannels, *J. Heat Transfer* 127 (2005) 101-107.
- [30] Y. Katto, General features of CHF of forced convection boiling in uniformly heated rectangular channels, *Int. J. Heat Mass Transfer* 24 (1981) 1413–1419.
- [31] K. Mishima, M. Ishii, Critical heat flux experiments under low flow conditions in a vertical annulus, ANL-82-6, NUREG/CR-2647, 1982.
- [32] Y. Sudo, K. Miyata, H. Ikawa, M. Kaminaga, M. Ohkawara, Experimental study of differences in DNB heat flux between upflow and downflow in vertical rectangular channel, *J. Nucl. Sci. Technol.* 22 (1985) 604–618.
- [33] N. Basu, G. R. Warriar, V. K. Dhir, Onset of nucleate boiling and active nucleation site density during subcooled flow boiling, *Journal of Heat Transfer* 124 (2002) 717-728.
- [34] W. Qu, I. Mudawar, Prediction and measurement of incipient boiling heat flux in micro-channel heat sinks, *International Journal of Heat and Mass Transfer*, 45 (2002), 3933-3945.
- [35] D. Liu, P. Lee, S. V. Garimella, Prediction of the onset of nucleate boiling in microchannel flow, *International Journal of Heat and Mass Transfer*, 48 (2005), 5134-5149.
- [36] Agrawal, S.G. Singh, A review of state-of-the-art on flow boiling of water in microchannel, *International Journal of Microscale and Nanoscale Thermal and Fluid Transport Phenomena*, 2 (2011) 1-39.
- [37] S.G. Singh, R.R. Bhide, S.P. Dutttagupta, A. Sridharan, A. Agrawal, Experimental study of water boiling in microchannel, *Advances in Multiphase Flow and Heat Transfer*, Eds: L. Cheng and D. Mewes, Vol. 3, pp. 246-303, Chapter 6, 2010 (Bentham Science Publishers).

Received 03 October 2011, *received in revised form* 12 August 2012; *accepted* 18 August 2012.

MELTING EFFECT ON NATURAL CONVECTION ABOUT AXISYMMETRIC STAGNATION POINT ON A SURFACE IN POROUS MEDIA WITH SORET AND DUFOUR EFFECTS AND TEMPERATURE- DEPENDENT VISCOSITY

M. Modather, M. Abdou^{1,2}, and Ali J. Chamkha^{3,}*

¹Department of Mathematics, Faculty of Science Aswan, Aswan University,
Aswan, Egypt

²Department of Mathematics, College of Science and Humanity Studies,
Salman Bin AbdulAziz University, Al-Kharj, KSA

³Manufacturing Engineering Department,
The Public Authority for Applied Education and Training, Shuweikh, Kuwait

ABSTRACT

A three-dimensional boundary layer solution is presented for melting effect on heat and mass transfer by natural convection with temperature-dependent viscosity in the vicinity of an axisymmetric stagnation point on heated vertical surfaces in porous media in the presence of Soret and Dufour effects. The governing equations for the velocity, temperature and concentration fields are solved numerically by the fourth order Runge-Kutta integration scheme. A parametric study illustrating the influence of the Darcy number, melting parameter or Stefan number, viscosity parameter, Dufour number and Soret number on the skin friction coefficient, Nusselt number as well as the Sherwood number are investigated. The results of the parametric study are shown in graphical and tabulated forms. It is found that increasing the Darcy number and the melting parameter within the boundary layer leads to increases in the velocity within the boundary layer and thus, increases the local skin friction coefficient. On the other hand, as the Darcy number and the melting parameter increase, the thermal boundary layer thickness decreases and thus, the rates of heat and mass transfer increase. As the Dufour number increases (or the Soret number decreases), the local skin friction coefficient increases and the local surface concentration decreases and thus increasing the local Sherwood number. Also, increasing the Dufour number tends to increase the local surface temperature and thus, decreasing the local Nusselt number.

* To whom correspondence should be addressed, email: achamkha@yahoo.com.

Keywords: Natural convection; melting effect; Dufour effect; Soret effect; porous media; variable viscosity; axisymmetric stagnation flow

NOMENCLATURE

a	constant in equation (7) [1/s]
C	concentration
C_p	specific heat of fluid [J/k]
C_s	concentration susceptibility
DA	Darcy number
D	Molecular diffusivity
D_m	mass diffusivity
D_u	Dufour number
f, F	dimensionless velocity function
g	acceleration due to gravity [m/s^2]
k	thermal conductivity [W/mK]
K	permeability of the porous media [m^2]
K_T	thermal-diffusion ratio.
M	melting parameter
Nu	Nusselt number, $Nu = q_w x / k (T_w - T_\infty)$
m_w	wall mass flux
p	pressure [N/m^2]
Pr_f	Prandtl number, $Pr_f = C_p \mu_f / k$
q_w	wall heat flux [W/m^2]
Sc	Schmidt number, $Sc = \mu_f / D_m$
Sh	Sherwood number, $Sh = m_w x / D_m (C_w - C_\infty)$
S_r	Soret number
T	temperature [K]
T_m	mean fluid temperature [K]
U_∞	free stream velocity [m/s]
u, v, w	velocity component in x, y and z-axis [m/s]
x, y, z	Cartesian coordinates [m]
Greek symbols	
α	thermal diffusivity [m^2/s]
β_T	coefficient of thermal expansion [K^{-1}]
β_C	coefficient of concentration expansion
μ	absolute dynamic viscosity [Ns/m^2]
λ	latent heat of the solid phase
θ	dimensionless temperature
ϕ	dimensionless concentration
γ_f	viscosity parameter [m^2/s]
ρ	density [kg/m^3]

Subscripts	refers to condition at wall
w	refers to condition far from the wall
∞	
Superscript	differentiation with respect to η

1. INTRODUCTION

The subject of convective flow in porous media has attracted considerable attention in the last few decades, due to its numerous applications in a wide variety of industrial processes as well as in many natural circumstances. Examples of such technological applications are geothermal extraction, storage of nuclear waste material, ground water flows, thermal insulation engineering, food processing, fibrous insulation, soil pollution and packed-bed reactors to name just a few. Seddeek [1] studied of the effect of a magnetic field and variable viscosity on steady two Darcy forced convection flow over a flat plate with variable wall temperature in a porous medium in the presence of blowing (suction). Hassanien et al. [2] investigated variable viscosity and thermal conductivity effects on combined heat and mass transfer in mixed convection over a UHF/UMF wedge in porous media in the entire regime. Bagai [3] investigated the effect of temperature dependent viscosity on heat transfer rates in the presence of internal heat generation, a similarity solution is proposed for the analysis of the steady free convection boundary layers over a non-isothermal axisymmetric body embedded in a fluid saturated porous medium. Modather and El-Kabeir [4] analyzed the effect of thermal radiation on free convection flow with variable viscosity and uniform suction velocity along a uniformly heated vertical porous plate embedded in a porous medium in the presence of a uniform transverse magnetic field. Modather [5] studied the effect of thermal radiation on unsteady boundary layer flow with temperature dependent viscosity and thermal conductivity due to a stretching sheet through porous media.

The effects of diffusion-thermo and thermal-diffusion of heat and mass transfer have been examined by Chapman and Cowling [6] and Hirshfelder et al. [7] from the kinetic theory of gases. They explained the phenomena and derived the necessary formulae to calculate the thermal-diffusion coefficient and the thermal-diffusion factor for monatomic gases or polyatomic gas mixtures. The heat and mass transfer simultaneously affecting each other that will cause the cross-diffusion effect. The heat transfer caused by concentration gradient is called the diffusion-thermo or Dufour effect. On the other hand, mass transfer caused by temperature gradients is called Soret or thermal-diffusion effect. Thus, the Soret effect is referred to species differentiation developing in an initial homogeneous mixture submitted to a thermal gradient and the Dufour effect is referred to the heat flux produced by a concentration gradient. The Soret effect, for instance, has been utilized for isotope separation, and in mixture between gases with very light molecular weight (H_2 , He) and of medium molecular weight (N_2 , air). Kafoussias and Williams [8] considered the boundary layer flows in the presence of Soret and Dufour effects associated with thermal-diffusion and diffusion-thermo for the mixed convection. The similarity equations of the problem considered are obtained by using the usual similarity technique. The Soret and Dufour effects have been found to appreciably influence the flow field in mixed convection boundary layer over a vertical surface embedded in a porous medium [9]. Alam and Rahman [10] investigated the

Dufour and Soret effects on mixed convection flow past a vertical porous flat plate with variable suction. Alam et al. [11] reported the effects of Dufour and Soret on unsteady MHD free Convection and mass transfer flow past a vertical porous plate in a porous medium numerically. Postelnicu [12] examined the heat and mass characteristics of natural convection about a vertical surface embedded in a saturated porous medium subjected to a magnetic field by considering the Dufour and Soret effects. The same author [13] studied influence of chemical reaction on heat and mass transfer by natural convection from vertical surfaces in porous media considering Soret and Dufour effects. Partha et al. [14] examined the Soret and Dufour effects in a non-Darcy porous medium. Mansour et al. [15] studied the multiplicity of solutions induced by thermosolutal convection in a square porous cavity heated from below and submitted to horizontal concentration gradient in the presence of Soret effect. Lakshmi Narayana et al. [16] studied the Soret and Dufour effects in a doubly stratified Darcy porous medium. Lakshmi Narayana and Murthy [17] examined the Soret and Dufour effects on free convection heat and mass transfer from a horizontal flat plate in a Darcy porous medium. Chamkha and Ben-Nakhi [18] considered the mixed convection flow with thermal radiation along a vertical permeable surface immersed in a porous medium in the presence of Soret and Dufour effects. El-Aziz [19] have investigated the combined effects of thermal-diffusion and diffusion-thermo on MHD heat and mass transfer over a permeable stretching surface with thermal radiation. Mahdy [20] studied the problem of MHD non-Darcian free convection from a vertical wavy surface embedded in porous media in the presence of Soret and Dufour effect.

In the present work, we consider the melting effect on natural convection flow with variable viscosity in the vicinity of an axisymmetric stagnation point on heated vertical surfaces in the presence of Soret and Dufour saturated in porous medium. The effect of Darcy number parameter, melting parameter, viscosity parameter, Dufour number and the Soret number on the velocity, temperature and concentration profiles as well as the skin friction coefficient, Nusselt number and the Sherwood number are investigated.

2. MATHEMATICAL FORMULATION

Consider an axisymmetric stagnation flow normal to a heated surface, as shown in Fig 1. The plate is in the x - y plane with z -axis in the vertical direction. The flow is impinging on the plate at the origin. In the formulation of the problem, the plate is assumed to be at a uniform temperature and concentration are T_w and C_w while the ambient fluid is maintained at the uniform temperature and concentration are T_∞ and C_∞ respectively. The dynamic viscosity μ is taken to be a variable in the equations of motion while the density ρ , the coefficients of thermal and concentration expansion are β_T and β_C respectively, permeability of the porous media is K , the thermal diffusivity, molecular diffusivity and mass diffusivity are α , D and D_m respectively, the specific heat at constant pressure and concentration susceptibility are C_p and C_s respectively, the mean fluid temperature is T_m and K_T is the thermal-diffusion ratio. Under the boundary layer assumptions, the governing equations are given by:

$$\frac{\partial u}{\partial x} + \frac{\partial v}{\partial y} + \frac{\partial w}{\partial z} = 0, \quad (1)$$

$$\rho \left(u \frac{\partial u}{\partial x} + v \frac{\partial u}{\partial y} + w \frac{\partial u}{\partial z} \right) = -\frac{\partial p}{\partial x} + \frac{\partial}{\partial x} \left(\mu \frac{\partial u}{\partial x} \right) + \frac{\partial}{\partial y} \left(\mu \frac{\partial u}{\partial y} \right) + \frac{\partial}{\partial z} \left(\mu \frac{\partial u}{\partial z} \right) + \rho g [\beta_T (T - T_\infty) + \beta_C (C - C_\infty)] - \frac{\mu}{K} u, \quad (2)$$

$$\rho \left(u \frac{\partial v}{\partial x} + v \frac{\partial v}{\partial y} + w \frac{\partial v}{\partial z} \right) = -\frac{\partial p}{\partial y} + \frac{\partial}{\partial x} \left(\mu \frac{\partial v}{\partial x} \right) + \frac{\partial}{\partial y} \left(\mu \frac{\partial v}{\partial y} \right) + \frac{\partial}{\partial z} \left(\mu \frac{\partial v}{\partial z} \right) - \frac{\mu}{K} v, \quad (3)$$

$$\rho \left(u \frac{\partial w}{\partial x} + v \frac{\partial w}{\partial y} + w \frac{\partial w}{\partial z} \right) = -\frac{\partial p}{\partial z} + \frac{\partial}{\partial x} \left(\mu \frac{\partial w}{\partial x} \right) + \frac{\partial}{\partial y} \left(\mu \frac{\partial w}{\partial y} \right) + \frac{\partial}{\partial z} \left(\mu \frac{\partial w}{\partial z} \right) - \frac{\mu}{K} w, \quad (4)$$

$$u \frac{\partial T}{\partial x} + v \frac{\partial T}{\partial y} + w \frac{\partial T}{\partial z} = \alpha \left(\frac{\partial^2 T}{\partial x^2} + \frac{\partial^2 T}{\partial y^2} + \frac{\partial^2 T}{\partial z^2} \right) + \frac{D_m K_T}{C_p C_s} \frac{\partial^2 C}{\partial y^2}, \quad (5)$$

$$u \frac{\partial C}{\partial x} + v \frac{\partial C}{\partial y} + w \frac{\partial C}{\partial z} = D \left(\frac{\partial^2 C}{\partial x^2} + \frac{\partial^2 C}{\partial y^2} + \frac{\partial^2 C}{\partial z^2} \right) + \frac{D_m K_T}{T_m} \frac{\partial^2 T}{\partial y^2}. \quad (6)$$

The boundary conditions are given by:

$$\begin{aligned} u = v = 0, \quad k \frac{\partial T}{\partial z} &= \rho [\lambda + C_p (T_w - T_\infty)] w, \quad T = T_w, \quad C = C_w. \quad \text{on } z=0 \\ u = ax, v = 0, w = -az, \quad T &= T_\infty, \quad C = C_\infty, \\ p &= p_0 - \frac{1}{2} \rho a^2 (x^2 + y^2). \quad \text{at } z = \infty \end{aligned} \quad (7)$$

Here u , v and w are the velocity components along x , y and z -axes; p is the pressure in the flow field; p_0 is the stagnation pressure; g is the acceleration due to gravity, λ is latent heat of the solid phase and the constant a is directly proportional to the free stream velocity (U_∞) far from the plate and inversely proportional to a characteristic length (L) of the plate.

Following Carey and Mollendorf [26], we assume that the absolute viscosity can be expressed as

$$\mu = \mu_f \left[1 + \frac{1}{\mu_f} \left(\frac{d\mu}{dT} \right)_f (T - T_f) \right] \quad (8)$$

where μ_f is the value of μ at the film temperature of the flow. The following transformations would reduce the governing equations (1-6) to ordinary differential equations:

$$u = \frac{g\beta(T_\infty - T_w)}{a} F(\eta) + axf'(\eta); \quad v = ayf'(\eta) \quad (9)$$

$$w = -2\sqrt{\frac{a\mu_f}{\rho}} f(\eta), \quad T - T_\infty = (T_w - T_\infty)\theta(\eta), \quad C - C_\infty = (C_w - C_\infty)\phi(\eta) \quad (10)$$

$$p = p_0 - \frac{\rho}{2} \left[a^2(x^2 + y^2) + w^2 - 2\frac{\mu_f}{\rho} \frac{dw}{dz} \right] \quad (11)$$

and

$$\eta = \sqrt{\frac{a\rho}{\mu_f}} z \quad (12)$$

where F, f, θ and ϕ are related to the non-dimensional velocity, temperature and concentration functions.

Using (10), relation (8) can be written as

$$\mu = \mu_f [1 + \gamma_f(\theta - 0.5)] \quad (13)$$

$$\text{where } \gamma_f = \left(\frac{1}{\mu} \frac{d\mu}{dT} \right)_f (T_w - T_\infty) \quad (14)$$

It can be verified that with transformations (9) to (12) the continuity equation (1) is automatically satisfied and the momentum, angular momentum and energy equations (2) to (6) reduce to:

$$[1 + \gamma_f(\theta - 0.5)]f''' + (2f + \gamma_f\theta')f'' + 1 - f'^2 - \frac{[1 + \gamma_f(\theta - 0.5)]}{DA}f' = 0 \quad (15)$$

$$[1 + \gamma_f(\theta - 0.5)]F'' + (2f + \gamma_f\theta')F' + fF - N\phi - \theta - \frac{[1 + \gamma_f(\theta - 0.5)]}{DA}F = 0 \quad (16)$$

$$\frac{1}{Pr_f}\theta'' + 2f\theta' + D_u\phi'' = 0 \quad (17)$$

$$\frac{1}{Sc}\phi'' + 2f\phi' + S_r\theta'' = 0 \quad (18)$$

where a prime denotes differentiation with respect to η only and $DA = \frac{K\rho a}{\mu_f}$ is Darcy

number, $N = \frac{\beta_C(C_w - C_\infty)}{\beta_T(T_w - T_\infty)}$ is concentration to thermal buoyancy parameter,

$Pr_f = \frac{C_p \mu_f}{k}$ is the film Prandtl number, $Sc = \frac{\mu_f}{D_m}$ is Schmidt number,

$D_u = \frac{D_m K_T (C_w - C_\infty)}{C_p C_s \mu_f (T_w - T_\infty)}$ is the Dufour number and $S_r = \frac{D_m K_T (T_w - T_\infty)}{\mu_f T_m (C_w - C_\infty)}$ is the Soret

number.

The transformed boundary conditions may be written as:

$$\begin{aligned} 2 Pr_f f(0) + M\theta'(0) = 0, \quad f'(0) = F(0) = 0, \quad \theta(0) = 1, \quad \phi(0) = 1, \\ f'(\infty) = 1, \quad F(\infty) = \theta(\infty) = \phi(\infty) = 0. \end{aligned} \quad (19)$$

where M is the Stefan number or the melting parameter.

The shear stress, heat and mass flux at the plate are important physical characteristics for this type of heat and mass transfer problem. They are given by:

$$\begin{aligned} \tau_{wx} &= \left(\mu \frac{\partial u}{\partial z} \right)_{z=0} \\ &= \mu_f \left(1 + \frac{1}{2} \gamma_f \right) \sqrt{\frac{a\rho}{\mu_f}} \left[\frac{g\beta(T_\infty - T_w)}{a} F'(0) + axf''(0) \right] \end{aligned} \quad (20)$$

$$\begin{aligned} \tau_{wy} &= \left(\mu \frac{\partial v}{\partial z} \right)_{z=0} \\ &= \mu_f \left(1 + \frac{1}{2} \gamma_f \right) \sqrt{\frac{a\rho}{\mu_f}} ayf''(0) \end{aligned} \quad (21)$$

$$q_w = -k \left(\frac{\partial T}{\partial z} \right)_{z=0} = -k \sqrt{\frac{a\rho}{\mu_f}} (T_w - T_\infty) \theta'(0). \quad (22)$$

$$m_w = -D_m \left(\frac{\partial C}{\partial z} \right)_{z=0} = -D_m \sqrt{\frac{a\rho}{\mu_f}} (C_w - C_\infty) \phi'(0).$$

One can write Nusselt number and Sherwood number as:

$$Nu = -\sqrt{\frac{a\rho}{\mu_f}}\theta'(0) \quad (23)$$

$$Sh = -\sqrt{\frac{a\rho}{\mu_f}}\phi'(0) \quad (24)$$

where

$$Nu = \frac{q_w}{T_w - T_\infty} \frac{x}{k} \quad \text{and} \quad Sh = \frac{m_w}{C_w - C_\infty} \frac{x}{D_m}. \quad (25)$$

where q_w and m_w are wall heat and mass flux, respectively.

3. NUMERICAL METHOD

The set of Equations (15) to (18) under the boundary conditions (19) has been solved numerically using the Runge–Kutta integration scheme with the shooting method. We let

$$f = x_1, \quad f' = x_2, \quad f'' = x_3, \quad F = x_4, \quad F' = x_5, \quad \theta = x_6, \quad \theta' = x_7, \quad \phi = x_8, \quad \phi' = x_9 \quad (26)$$

Equations (15) to (18) are transformed into systems of first-order differential equations as follows:

$$\begin{aligned} x_1' &= x_2 \\ x_2' &= x_3 \\ x_3' &= -\frac{1}{(1 + \gamma_f(x_6 - 0.5))} \left((2x_1 + \gamma_f x_7)x_3 + 1 - x_2^2 - \frac{[1 + \gamma_f(x_6 - 0.5)]}{DA} x_2 \right) \\ x_4' &= x_5 \\ x_5' &= -\frac{1}{(1 + \gamma_f(x_6 - 0.5))} \left((2x_1 + \gamma_f x_7)x_5 + x_2 x_4 - Nx_8 - x_6 - \frac{[1 + \gamma_f(x_6 - 0.5)]}{DA} x_4 \right) \\ x_6' &= x_7 \\ x_7' &= -Pr_f (2x_1 x_7 + D_u x_9) \quad x_8' = x_9 \\ x_9' &= -Sc (2x_1 x_9 + S_r x_7') \end{aligned} \quad (27)$$

subject to the following initial conditions:

$$2Pr_f x_1(0) + Mx_7(0) = 0, \quad x_2(0) = x_4(0) = 0, \quad x_6(0) = 1, \quad x_8(0) = 1,$$

$$x_2(\infty) = 1, \quad x_4(\infty) = x_6(\infty) = x_8(\infty) = 0. \quad (28)$$

Equation (27) is then integrated numerically as an initial-value problem to a given terminal point. The accuracy of the assumed missing initial condition is then checked by comparing the calculated value of the dependent variable at the terminal point with its given value. If a difference exists, improved values of the missing initial conditions must be obtained and the process is repeated. A step size of $\eta = 0.001$ was selected to be satisfactory for a convergence criterion of 10^{-6} in nearly all cases. The maximum value of η_∞ to each group of parameters DA, Pr_f, Sc, D_u, S_r, M, N and γ_f are determined when the values of unknown boundary conditions at $\eta = 0$ do not change to successful loop with error less than 10^{-6} . From the process of numerical computation, the local skin friction coefficient, the local Nusselt number and the local Sherwood number, which are respectively proportional to $f''(0)$, $-F'(0)$, $-\theta'(0)$ and $-\phi'(0)$ are worked out and their numerical values presented in tabular forms.

4. RESULTS AND DISCUSSION

Based on the fourth-order Runge-Kutta integration scheme described above, calculations were carried out for the values of Prandtl number Pr=0.733, Schmidt number Sc=0.66, Darcy number DA ranging from 1.0 to ∞ , variable viscosity parameter γ_f ranging from -0.8 to 0.8, Soret number S_r ranging from 0.06 to 0.8, Dufour number D_u ranging from 0.075 to 1.0 (the product of S_r and D_u must stay constant i.e. 0.06) and melting parameter M ranging from 0.0 to 1.5 with N=0.5.

It should be noted here that in the case of $\gamma_f=0$, M=0, Sc=0, DA= ∞ and D_u=S_r=0, Wang [27] has derived the solution of this problem. On the other hand, for the variable viscosity case (M=0, Sc=0, DA= ∞ and D_u=S_r=0) solution of the above equations (15-18) has been obtained by Takhar [28] for Pr_f=0.7,1,10 and 100 and viscosity variation parameter (-1.6 ≤ γ_f ≤ 1.6). The present results were compared with the results reported by Takhar [28] and they were found to be in good agreement.

Tables 1-3 display the results for the flow from heated vertical surface which show the surface values of velocity, temperature and concentration gradient components. These are proportional to the friction factor, Nusselt number and Sherwood number respectively. Table 1 shows the effect of the melting parameter M and the Darcy number DA on the local skin friction coefficient, Nusselt number and the Sherwood number.

The results indicate that as the melting parameter M increases, there is an increase in the local skin friction coefficient while the local Nusselt and Sherwood numbers have the opposite behavior. The Darcy number parameter also has a noticeable effect on the local skin friction coefficient. Increasing the Darcy number within the boundary layer leads to an increase in the velocity within the boundary layer and thus, increases the local skin friction coefficient. On the other hand, as the Darcy number increases, the thermal boundary layer thickness decreases and thus, the rates of heat and mass transfer increase.

Table 1. Values of $f''(0)$, $F'(0)$, $\theta'(0)$ and $\phi'(0)$ with $Pr = 0.733$, $Sc = 0.66$ and $N = 0.5$.

DA	M	$f''(0)$	$-F'(0)$	$-\theta'(0)$	$-\phi'(0)$	$-F'(0)/f''(0)$
1.0	0.0	0.72729	0.78105	0.51764	0.51065	1.07391
	0.4	0.77812	0.77188	0.58483	0.57518	0.99199
	0.8	0.85050	0.75704	0.67785	0.66441	0.89011
	1.0	0.90000	0.74621	0.73975	0.72374	0.82912
	1.5	1.10432	0.70007	0.98286	0.95659	0.63394
2.0	0.0	0.85556	0.80577	0.55306	0.54549	0.94180
	0.4	0.91999	0.79256	0.62485	0.61444	0.86149
	0.8	1.01098	0.77261	0.72405	0.70959	0.76422
	1.0	1.07269	0.75870	0.78995	0.77275	0.70729
	1.5	1.32327	0.70299	1.04780	1.01971	0.53125
5.0	0.0	0.94762	0.81794	0.57558	0.56764	0.86315
	0.4	1.02127	0.80222	0.65014	0.63925	0.78551
	0.8	1.12468	0.77919	0.75304	0.73795	0.69281
	1.0	1.19443	0.76350	0.82132	0.80338	0.63922
	1.5	1.47481	0.70253	1.08785	1.05863	0.47636
20.0	0.0	0.99816	0.82320	0.58711	0.57899	0.82471
	0.4	1.07670	0.80622	0.66306	0.65192	0.74879
	0.8	1.18663	0.78169	0.76781	0.75239	0.65875
	1.0	1.26057	0.76515	0.83727	0.81895	0.60699
	1.5	1.55633	0.70174	1.10808	1.07828	0.45090
50.0	0.0	1.00864	0.82418	0.58944	0.58128	0.81712
	0.4	1.08817	0.80695	0.66566	0.65448	0.74157
	0.8	1.19943	0.78213	0.77078	0.75529	0.65209
	1.0	1.27423	0.76543	0.84048	0.82208	0.60070
	1.5	1.57309	0.70154	1.11213	1.08223	0.44596
100.0	0.0	1.01216	0.82450	0.59022	0.58204	0.81460
	0.4	1.09202	0.80719	0.66653	0.65533	0.73917
	0.8	1.20373	0.78227	0.77178	0.75626	0.64988
	1.0	1.27881	0.76551	0.84155	0.82312	0.59861
	1.5	1.57871	0.70147	1.11349	1.08354	0.44433
∞	0.0	1.01569	0.82482	0.59099	0.58281	0.81208
	0.4	1.09589	0.80743	0.66740	0.65618	0.73678
	0.8	1.20804	0.78241	0.77277	0.75723	0.64767
	1.0	1.28341	0.76560	0.84262	0.82417	0.59653
	1.5	1.58435	0.70140	1.11484	1.08486	0.44270

Table 2. Values of $f''(0), F'(0), \theta'(0)$ and $\phi'(0)$ with $Pr = 0.733, Sc = 0.66$ and $N = 0.5$

D_u	S_r	M	$f''(0)$	$-F'(0)$	$-\theta'(0)$	$-\phi'(0)$	$-F'(0)/f''(0)$
0.075	0.80	0.0	1.05053	0.90275	0.64464	0.42769	0.85932
		0.4	1.14758	0.88995	0.75422	0.44354	0.77550
		0.8	1.29893	0.86655	0.92379	0.46212	0.66713
		1.0	1.41419	0.84727	1.05150	0.47300	0.59912
		1.5	2.07204	0.73621	1.75681	0.51365	0.35531
0.15	0.40	0.0	1.05245	0.87204	0.62712	0.53183	0.82858
		0.4	1.14598	0.85481	0.72501	0.59028	0.74592
		0.8	1.28636	0.82727	0.87057	0.67473	0.64311
		1.0	1.38847	0.80685	0.97525	0.73422	0.58111
		1.5	1.88960	0.71170	1.47490	1.01152	0.37664
0.30	0.20	0.0	1.05627	0.86620	0.59208	0.58382	0.82006
		0.4	1.14298	0.84965	0.66872	0.65742	0.74337
		0.8	1.26419	0.82527	0.77440	0.75877	0.65280
		1.0	1.34560	0.80861	0.84445	0.82589	0.60093
		1.5	1.67026	0.74380	1.11735	1.08723	0.44532
0.60	0.10	0.0	1.06384	0.88249	0.52192	0.60963	0.82953
		0.4	1.13772	0.87103	0.56383	0.67962	0.76559
		0.8	1.22892	0.85562	0.61402	0.76558	0.69624
		1.0	1.28297	0.84607	0.64308	0.81628	0.65946
		1.5	1.45244	0.81512	0.73163	0.97386	0.56120
1.0	0.06	0.0	1.07381	0.91325	0.42827	0.61972	0.85047
		0.4	1.13199	0.90787	0.43772	0.67620	0.80201
		0.8	1.19452	0.90106	0.44650	0.73689	0.75433
		1.0	1.22736	0.89713	0.45062	0.76874	0.73094
		1.5	1.31390	0.88585	0.46017	0.85254	0.67422

Table 3. Values of $f''(0), F'(0), \theta'(0)$ and $\phi'(0)$ with $Pr = 0.733, Sc = 0.66$ and $N = 0.5$

γ_f	DA	$f''(0)$	$-F'(0)$	$-\theta'(0)$	$-\phi'(0)$	$-F'(0)/f''(0)$
-0.80	1.00	1.51537	1.52585	0.55310	0.69844	1.00692
	2.0	1.84679	1.52912	0.60507	0.76323	0.82799
	5.0	2.10996	1.51824	0.64044	0.80730	0.71956
	20.0	2.26229	1.50930	0.65912	0.83059	0.66715
	50.0	2.29450	1.50724	0.66292	0.83533	0.65689
	100.0	2.30537	1.50654	0.66419	0.83692	0.65349
	∞	2.31631	1.50583	0.66547	0.83851	0.65010
-0.60	1.0	1.35138	1.35169	0.54899	0.69153	1.00023
	2.0	1.64403	1.35863	0.59916	0.75410	0.82640
	5.0	1.87312	1.35214	0.63296	0.79624	0.72187
	20.0	2.00471	1.34597	0.65072	0.81839	0.67140
	50.0	2.03245	1.34451	0.65433	0.82289	0.66152
	100.0	2.04181	1.34401	0.65554	0.82440	0.65825

Table 3. (Continued)

γ_f	DA	$f''(0)$	$-F'(0)$	$-\theta'(0)$	$-\phi'(0)$	$-F'(0)/f''(0)$
0.0	∞	2.05122	1.34350	0.65675	0.82591	0.65498
	1.0	1.04181	1.01970	0.54076	0.67690	0.97877
	2.0	1.25907	1.03380	0.58562	0.73302	0.82108
	5.0	1.42232	1.03596	0.61494	0.76968	0.72836
	20.0	1.51404	1.03527	0.63014	0.78869	0.68378
	50.0	1.53321	1.03499	0.63322	0.79254	0.67505
	100.0	1.53967	1.03489	0.63425	0.79383	0.67215
	∞	1.54615	1.03478	0.63528	0.79511	0.66926
0.60	1.0	0.86564	0.82678	0.53687	0.66853	0.95511
	2.0	1.03683	0.84538	0.57620	0.71802	0.81535
	5.0	1.16070	0.85291	0.60121	0.74948	0.73482
	20.0	1.22892	0.85562	0.61402	0.76558	0.69624
	50.0	1.24307	0.85608	0.61660	0.76883	0.68869
	100.0	1.24783	0.85623	0.61746	0.76992	0.68618
	∞	1.25260	0.85638	0.61832	0.77100	0.68368
	0.80	1.0	0.82261	0.77877	0.53631	0.66677
2.0		0.98179	0.79858	0.57371	0.71395	0.81340
5.0		1.09563	0.80752	0.59729	0.74369	0.73704
20.0		1.15794	0.81113	0.60932	0.75887	0.70049
50.0		1.17084	0.81178	0.61174	0.76192	0.69333
100.0		1.17518	0.81200	0.61255	0.76294	0.69096
∞		1.17952	0.81221	0.61335	0.76396	0.68859

The effects of the Soret S_r and Dufour D_u numbers with the melting parameter on the local skin friction coefficient, Nusselt number and Sherwood number are shown in Table 2. The Soret number S_r represents the effect of temperature gradients on mass (species) diffusion while the Dufour number D_u simulates the effect of concentration gradients on thermal energy flux in the flow domain. Table 2 indicates that as the Dufour number increases (and the Soret number decreases), significant changes in the local heat and mass transfer coefficients and a slight change in the value of local skin friction coefficient are caused. As the Dufour number increases (and the Soret number decreases), the local skin friction coefficient increases and the local surface concentration decreases and thus increasing the local Sherwood number. Increasing the Dufour number tends to increase the local surface temperature and thus, decreasing the local Nusselt number.

The effects of the temperature-dependent viscosity with Darcy number on the local skin friction coefficient, Nusselt number and Sherwood number are shown in Table 3. It can be seen from this table that the viscosity variation parameter has a significant effect on the local Nusselt number. As the viscosity variation parameter decreases, the thermal boundary layer thickness decreases and, thus, the rate of heat transfer increases. The viscosity variation parameter also has a noticeable effect on the local skin friction coefficient and a slight effect on the local mass transfer coefficient. It is observed that decreasing the viscosity within the boundary layer leads to an increase in the velocity within the layer and, thus, increases the local skin friction coefficient while the local mass transfer coefficient has the opposite behavior.

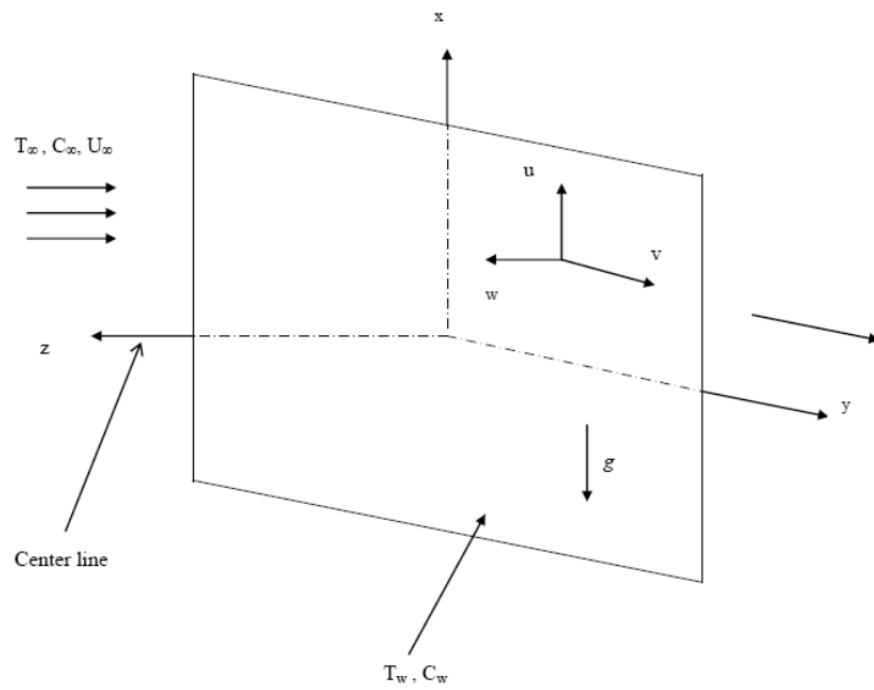


Figure 1. Physical model and coordinate system.

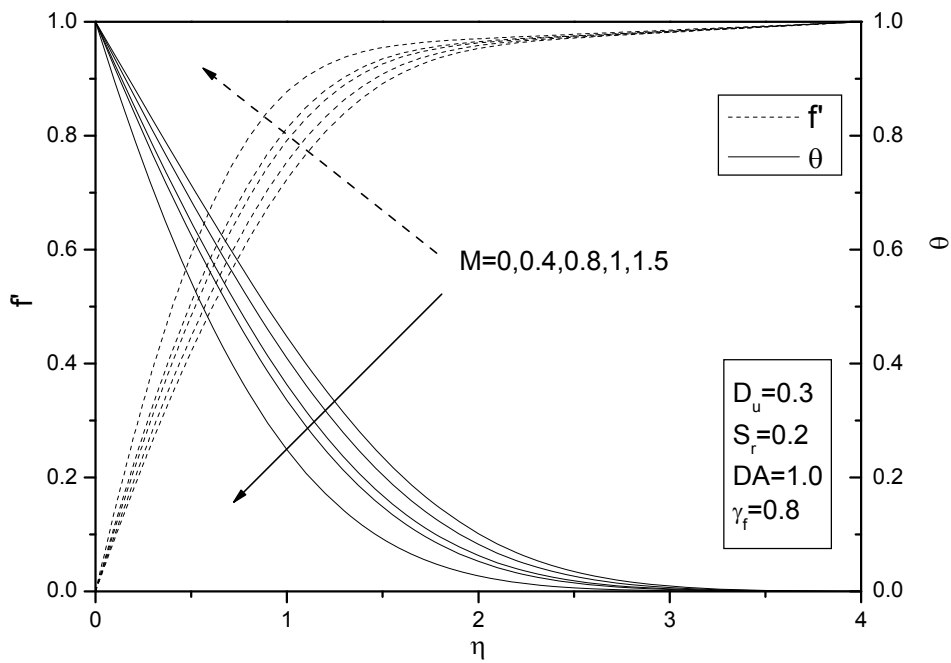
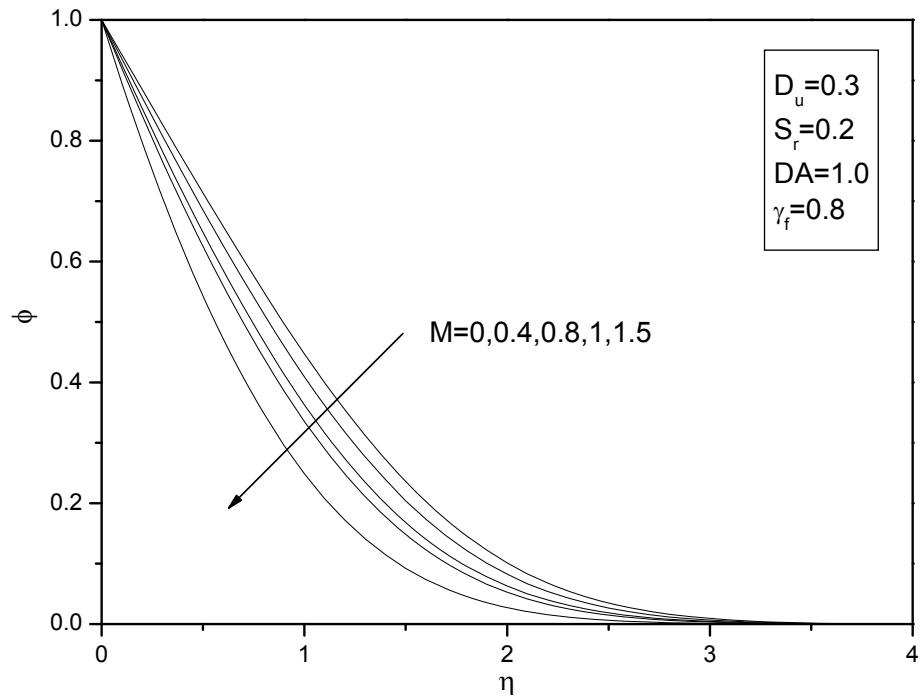
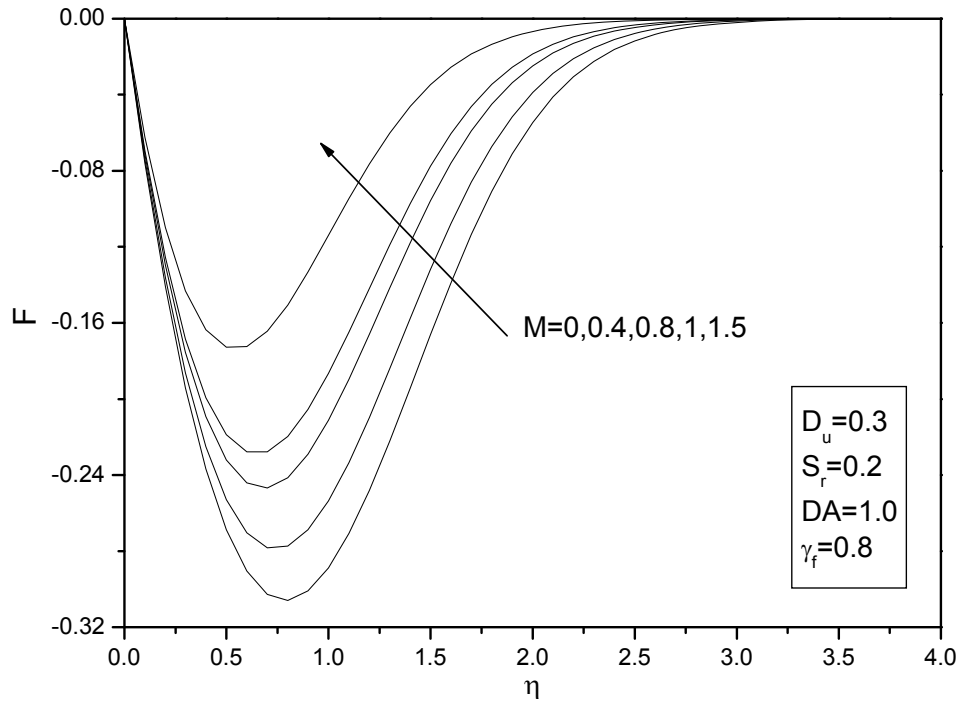


Figure 2. Effect of melting parameter M on velocity (f') and temperature (θ) profiles.

Figure 3. Effect of melting parameter M on concentration profile (ϕ).Figure 4. Effect of melting parameter M on velocity profile (F).

Figures 2-4 display typical dimensionless velocity, temperature and concentration profiles for various values of the melting parameter M , respectively. It can be seen that the velocity of the fluid increases as the melting parameter M increases while temperature and concentration decrease.

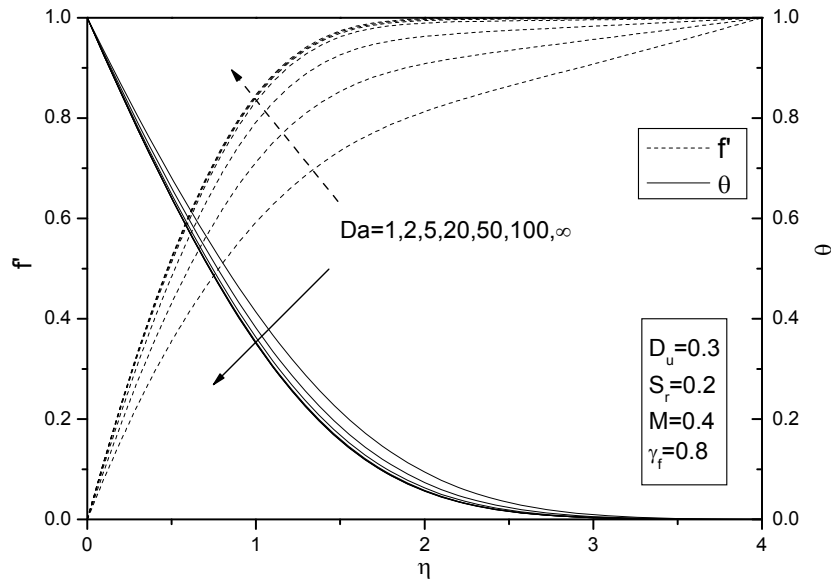


Figure 5. Effect of Darcy number Da on Velocity (f') and temperature (θ) profiles.

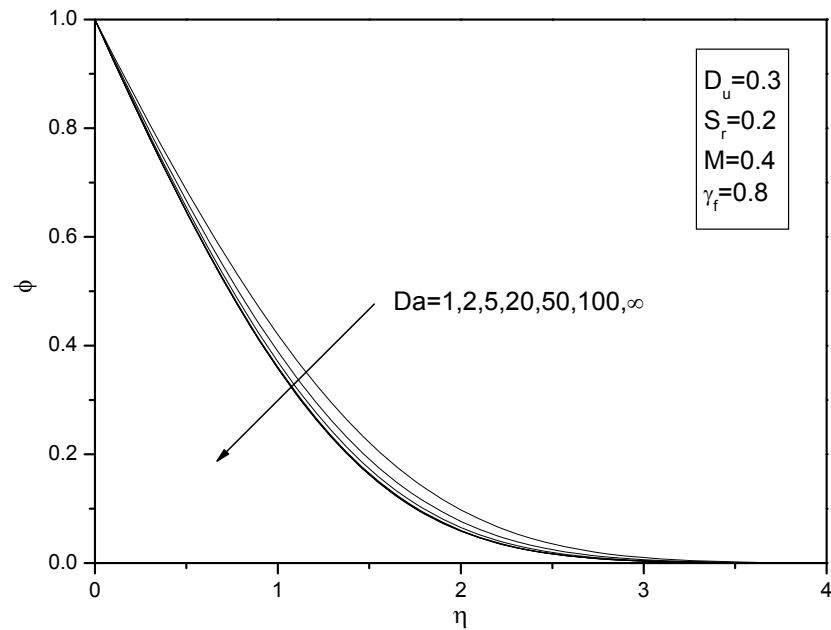


Figure 6. Effect of Darcy number Da on concentration profile (ϕ).

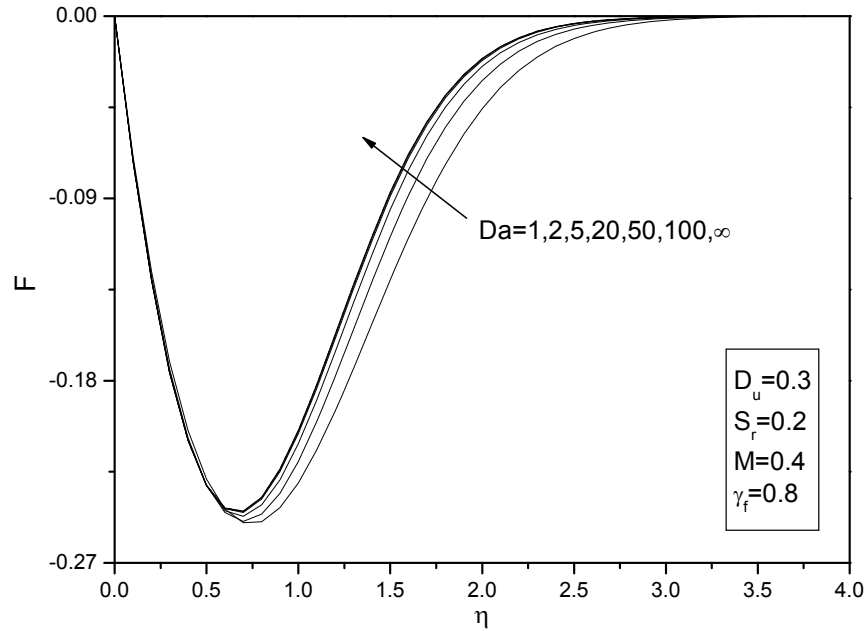


Figure 7. Effect of Darcy number Da on Velocity profile (F).

Figures 5-7 describe the behavior of the velocity, temperature and concentration fields for various values of the Darcy number parameter DA , respectively. It can be seen that the mass concentration and the fluid temperature fields decrease as the Darcy number DA increases, while the velocity increases as the Darcy number DA increases.

Figures 8-10 display the dimensionless velocity, temperature and concentration profiles for various values of variable viscosity γ_f , respectively. It is observed that the temperature and concentration across the boundary layer increase while the fluid velocity decreases with increasing values of the viscosity variation parameter γ_f .

Figures 11-13 show the velocity, temperature and concentration distributions with collective variation in the Soret number S_r , and the Dufour number D_u , respectively. We observe from these figures that a decrease in the value of D_u from 1.0 to 0.075 strongly increases the fluid velocity and decreases the fluid temperature values in the regime. Decreasing the value of D_u clearly reduces the influence of species gradients on the temperature field, so that the temperature function values are clearly lowered and the boundary layer regime is cooled. The S_r values rise from 0.06 to 0.8 over this range (the product of S_r and D_u must stay constant i.e. 0.06). On the other hand, the concentration function in the boundary layer regime is increased as D_u is decreased from 1.0 to 0.075 (and S_r simultaneously increased from 0.06 to 0.8). The mass diffusion is evidently enhanced in the domain as a result of the contribution of the temperature gradients.

From equation (20) it follows that the stagnation point is at:

$$x_s = \frac{g\beta(T_w - T_\infty) F'(0)}{a^2 f''(0)} \text{ at } y=z=0 \quad (29)$$

Since $F'(0)$ is negative, the stagnation point is below the centre line of the flow when $T_w > T_\infty$ (heated wall) and above the centre line of the flow for $T_w < T_\infty$ (cooled wall).

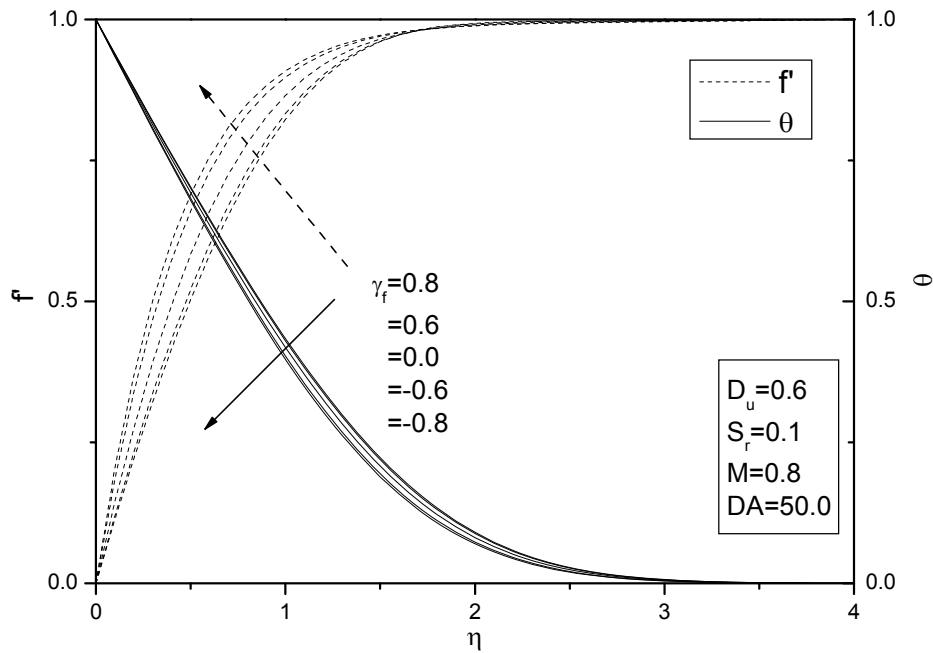


Figure 8. Effect of variable viscosity γ_f on velocity (f) and temperature (θ) profiles.

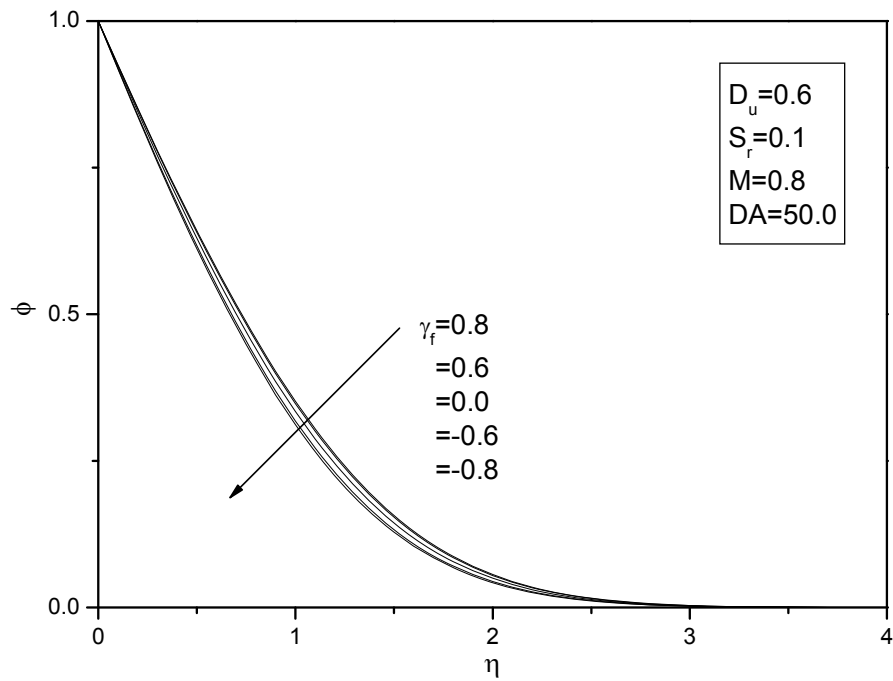


Figure 9. Effect of variable viscosity γ_f on concentration profile (ϕ).

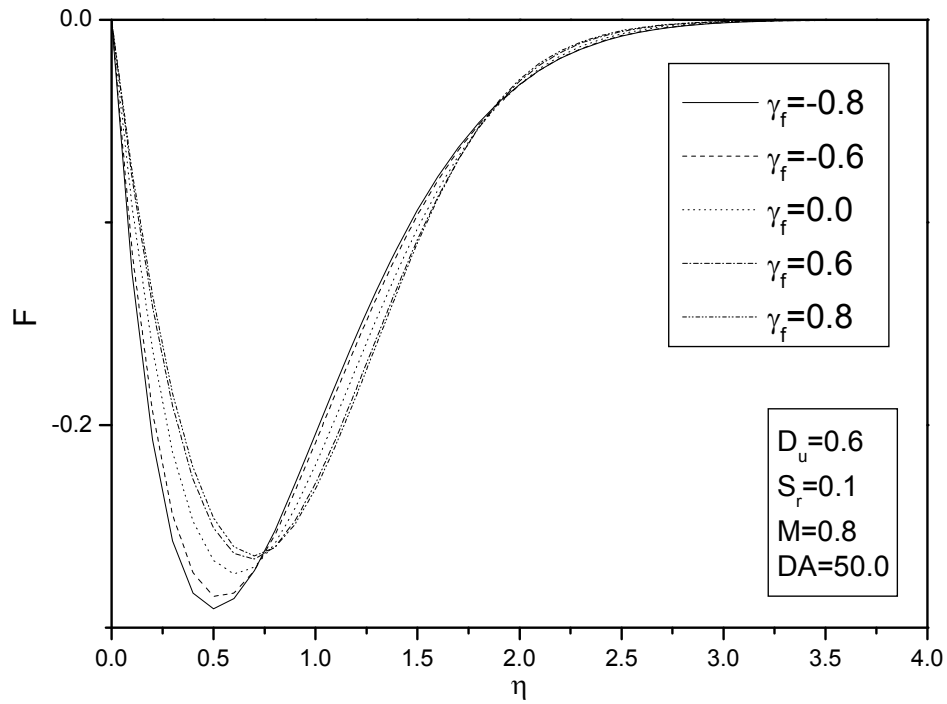


Figure 10. Effect of variable viscosity γ_f on Velocity profile (F).

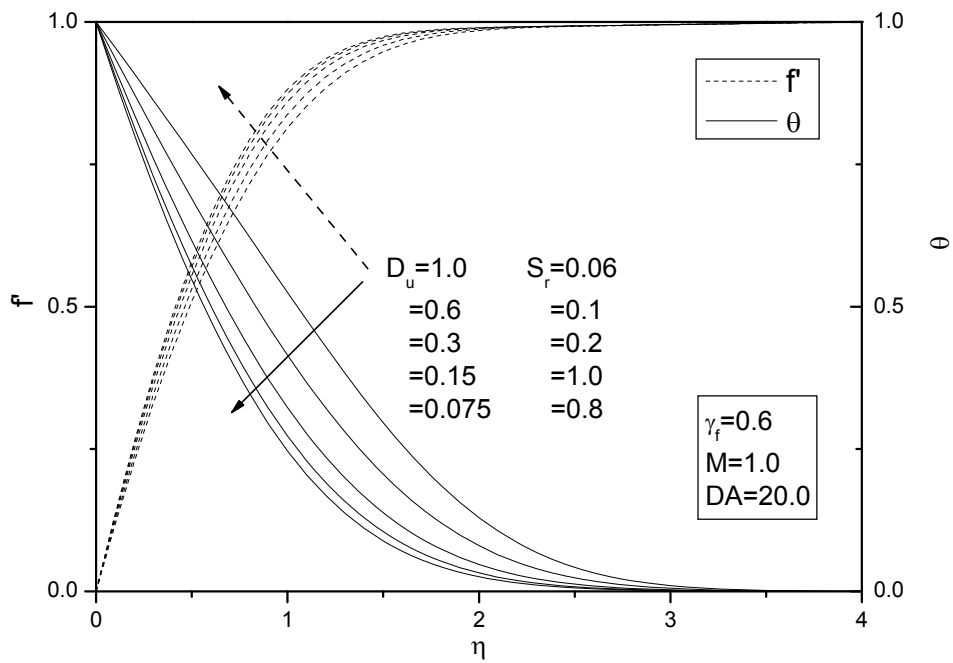
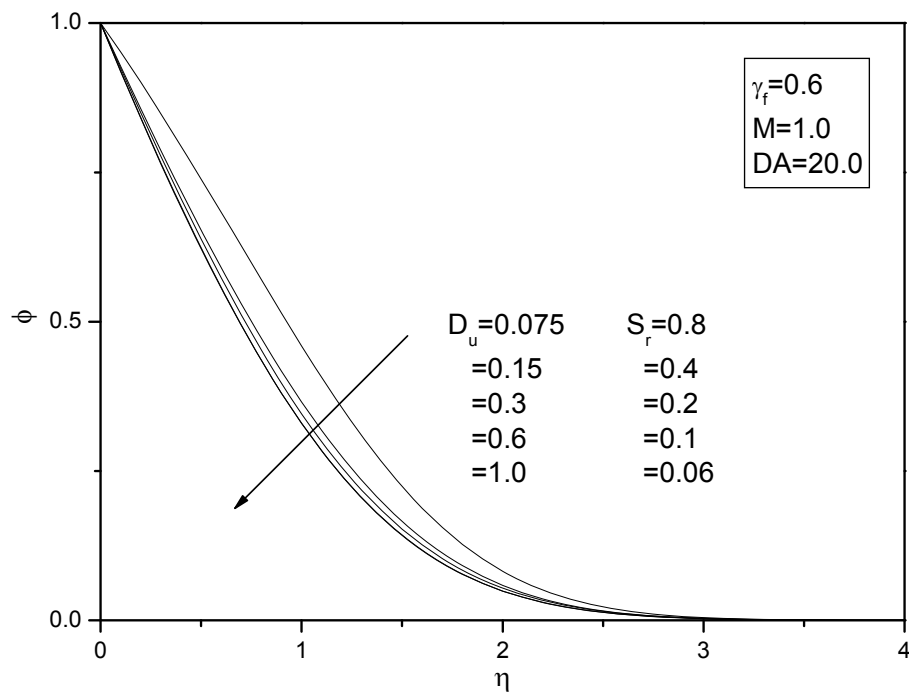
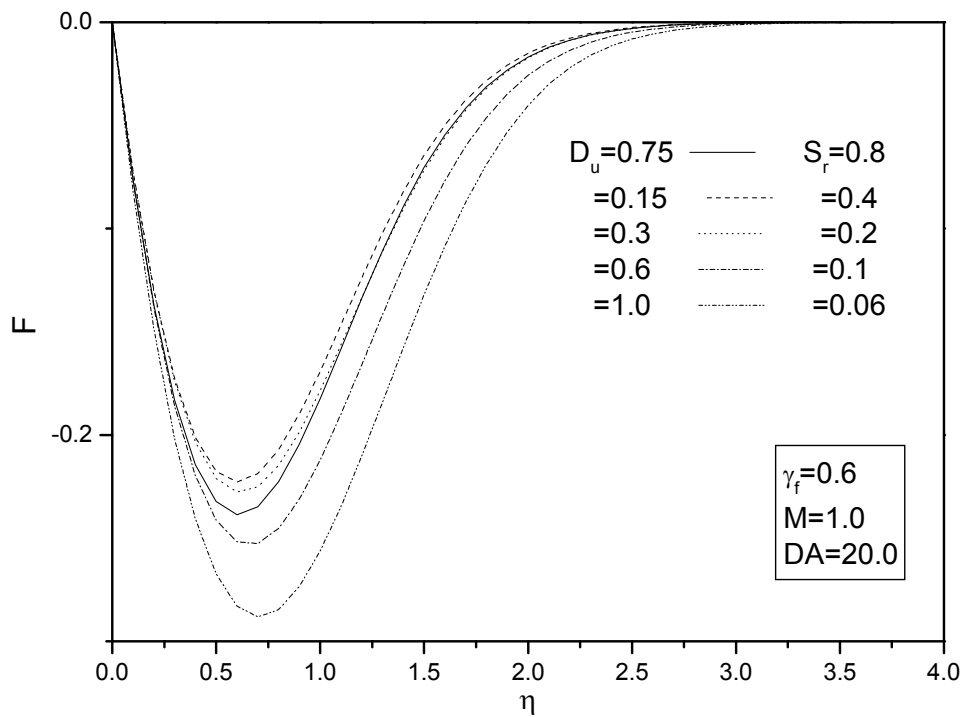


Figure 11. Effect of Dufour D_u and Soret S_r on velocity (f') and temperature (θ) profiles.

Figure 12. Effect of Dufour D_u and Soret S_r on concentration profile (ϕ).Figure 13. Effect of Dufour D_u and Soret S_r on Velocity profile (F).

CONCLUSION

In the present work, the melting effect on natural convection flow with variable viscosity in the vicinity of an axisymmetric stagnation point on heated vertical surfaces in saturated porous media in the presence of Soret and Dufour effects was studied. The viscosity of the fluid was taken as a function of temperature. The governing equations were developed and transformed into a set of similarity equations. These equations were solved by the fourth order Runge-Kutta numerical method. Favorable comparisons with previously published work were performed and the results were found to be in good agreement. The effects of Darcy number parameter, melting parameter, viscosity parameter, Dufour number and the Soret number on the velocity, temperature, and concentration profiles as well as the skin friction coefficient, Nusselt number and the Sherwood number were investigated. It was concluded that as the melting parameter increased, the local skin friction coefficient was increased while the local Nusselt number and Sherwood number had the opposite behavior. The Darcy number had a noticeable effect on the local skin friction coefficient and the local heat and mass transfer coefficients. Increasing the Dufour number (with the Soret number decreasing) led to significant changes in the local heat and mass transfer coefficients and a slight change in the value of local skin friction coefficient. As the Dufour number increased (and the Soret number decreased), the local skin friction coefficient increased and the local surface concentration decreased and thus, increased the local Sherwood number. Increasing the Dufour number increased the local surface temperature and thus, decreased the local Nusselt number.

REFERENCES

- [1] Seddeek, M. A., Effects of magnetic field and variable viscosity on forced non-Darcy flow about a flat plate with variable wall temperature in porous media in the presence of suction and blowing, *Journal of Applied Mechanics and Technical Physics*, vol. 43, No. 1, pp. 13-17, 2002.
- [2] Hassanien, I. A. Essawy, A. H. and Moursy, N. M., Variable viscosity and thermal conductivity effects on combined heat and mass transfer in mixed convection over a UHF/UMF wedge in porous media: the entire regime, *Applied Mathematics and Computation*, vol. 145, No. 2-3, pp. 667-682, 2003.
- [3] Bagai, S., Effect of variable viscosity on free convection over a non-isothermal axisymmetric body in a porous medium with internal heat generation, *Acta Mechanica*, vol. 169, No. 1-4, pp. 187-194, 2004.
- [4] Abdou, M. Modather M. and EL-Kabeir, S.M.M., Magnetohydrodynamics and radiative effect on free convection flow of fluid with variable viscosity from a vertical plate through a porous medium, *J. of Porous Media*, vol. 10, No. 5, pp. 503-514, 2007.
- [5] Abdou, M. Modather M., Effect of Radiation with Temperature Dependent Viscosity and Thermal Conductivity on Unsteady a Stretching Sheet through Porous Media, *Nonlinear Analysis: Modelling and Control*, vol. 15, No. 3, pp. 257-270, 2010.
- [6] Chapman S., and Cowling, T.G., *The mathematical theory of non-uniform gases*. Cambridge, UK: Cambridge Univ. Press; 1952.

-
- [7] Hirshfelder J.O., Curtis C.F., and Bird R.B., *Molecular theory of gases and liquids*, New York, Wiley, 1954.
- [8] Kafoussias, N.G., and Williams, E.W., Thermal-diffusion and diffusion thermo effects on mixed free-forced convective and mass transfer boundary layer flow with temperature dependent viscosity, *Int. J. Eng. Sci.*, vol. 33, pp. 1369–1384, 1995.
- [9] Anghel M., Takhar H.S., and Pop I. Studia universitatis Babes-Bolyai. *Mathematica* 2000; XLV:11.
- [10] Alam M.S., and Rahman M.M., Dufour and Soret effects on mixed convection flow past a vertical porous flat plate with variable suction, *Nonlinear Analysis: Modelling and Control*, vol. 11, pp. 3–12, 2006.
- [11] Alam, M.S., Rahman, M.M. and Samad, M.A., Dufour and Soret effects on unsteady MHD free convection and mass transfer flow past a vertical porous plate in a porous medium, *Nonlinear Analysis: Modelling and Control*, vol. 11, pp. 217–226, 2006.
- [12] Postelnicu, A., Influence of a magnetic field on heat and mass transfer by natural convection from vertical surfaces in porous media considering Soret and Dufour effects, *International Journal of Heat and Mass Transfer*, vol. 47, pp. 1467–1472, 2004.
- [13] Postelnicu, A., Influence of chemical reaction on heat and mass transfer by natural convection from vertical surfaces in porous media considering Soret and Dufour effects, *Heat Mass Transfer*, vol. 43, pp. 595–602, 2007.
- [14] Partha, M.K., Murthy, P.V.S.N., and Sekhar, G.P. Raja, Soret and Dufour effects in a non-Darcy porous medium, *Journal of Heat Transfer*, vol. 128, pp. 605–610, 2006.
- [15] Mansour, A., Amahmid, A., Hasnaoui, M., and Bourich, M., Multiplicity of solutions induced by thermosolutal convection in a square porous cavity heated from below and submitted to horizontal concentration gradient in the presence of Soret effect, *Numerical Heat Transfer; Part A: Applications*, vol. 49, pp. 69–94, 2006.
- [16] Narayana, P.A. Lakshmi, and Murthy, P.V.S.N., Soret and Dufour effects in a doubly stratified Darcy porous medium, *Journal of Porous Media*, vol. 10, pp. 613–624, 2007.
- [17] Narayana, P.A. Lakshmi, and Murthy, P.V.S.N., Soret and Dufour effects on free convection heat and mass transfer from a horizontal flat plate in a Darcy porous medium, *Journal of Heat Transfer*, vol. 130, pp. 104504–104505, 2008.
- [18] Chamkha, A.J., and Ben-Nakhi, A., MHD mixed convection-radiation interaction along a permeable surface immersed in a porous medium in the presence of Soret and Dufour's effects, *Heat Mass Transfer*, vol. 44, No. 7, pp. 845–856, 2008.
- [19] El-Aziz, M.A., Thermal-diffusion and diffusion-thermo effects on combined heat mass transfer by hydromagnetic three-dimensional free convection over a permeable stretching surface with radiation, *Physics Letter A*, vol. 372, No. 3, pp. 263–272, 2008.
- [20] Mahdy, A., MHD non-Darcian free convection from a vertical wavy surface embedded in porous media in the presence of Soret and Dufour effect, *International Communications in Heat and Mass Transfer*, vol. 36, pp. 1067–1074, 2009.
- [21] Cheng, C.Y., Soret and Dufour effects on natural convection heat and mass transfer from a vertical cone in a porous medium, *International Communications in Heat and Mass Transfer*, vol. 36, pp. 1020-1024, 2009.
- [22] Cheng, C.Y., Soret and Dufour effects on free convection boundary layer flow over a vertical cylinder in a saturated porous medium, *International Communications in Heat and Mass Transfer*, vol. 37, pp. 796–800, 2010.

- [23] Cheng, C.Y., Soret and Dufour effects on natural convection boundary layer flow over a vertical cone in a porous medium with constant wall heat and mass fluxes, *International Communications in Heat and Mass Transfer*, vol. 38, pp. 44–48, 2011.
- [24] Tai, B.-C., and Char, M.I., Soret and Dufour effects on free convection flow of non-Newtonian fluids along a vertical plate embedded in a porous media with thermal radiation, *International Communications in Heat and Mass Transfer*, vol. 37, pp. 480–483, 2010.
- [25] Pal, D., and Mondal, H., Effects of Soret Dufour, chemical reaction and thermal radiation on MHD non-Darcy unsteady mixed convective heat and mass transfer over stretching sheet, *Commun. Nonlinear Sci. Numer. Simulat.*, vol. 16, pp. 1942–1958, 2011.
- [26] Carey, P. V., and Mollendorf, C. J., Natural convection in liquids with temperature-dependent viscosity, in *Proceedings of the Sixth International Heat Transfer Conference*, Toronto, vol. 2, pp. 211-217, Hemisphere, Washington, D. C. 1978.
- [27] Wang, C. Y., *J. Appl. Mech.*, vol. 2, pp. 724-725, 1987.
- [28] Takhar, H.S., Variable viscosity effects on natural convection in axisymmetric stagnation flows adjacent to vertical surfaces, *Int. Comm. Heat Mass Transfer*, vol. 20, pp. 255-264, 1993.

Received 08 June 2011, *received in revised form* 18 September 2012; *accepted* 18 September 2012.

PUSHING THE LIMITS OF LIQUID COOLING: DESIGN AND ANALYSIS OF A DIRECT LIQUID COOLING SYSTEM FOR POWER MODULES

Matt Reeves, Jesus Moreno, Peter Beucher,
Sy-Jenq Loong, and David Bono*

Wolverine Tube Inc., MicroCool Division, Market Street NE,
Decatur, AL, USA

ABSTRACT

Direct cooling of power modules offers significant advantages over traditional cooling technologies using coldplates. Essentially, direct cooling of power modules eliminates the layer of TIM (Thermal Interface Material) needed between the module and the coldplate yielding to a much lower thermal resistance. As a consequence of such improvement lower operating temperatures or, conversely, high power densities can be achieved. Additionally, direct cooling of power modules offers a more compact, reliable, and cost effective cooling technology than traditional coldplates. Design and analysis of a new direct cooling integrated system for power modules will be presented in this work. It is concluded that the new proposed integrated cooling concept could improve by up to 70% the thermal performance of the system compared to a traditional coldplate design. Suppression of the TIM layer allows to take advantage of the promising micro deformation technology (MDT) to create optimal fin and pin geometries 'pushing the limits' of liquid cooling restricted, usually, by the low thermal performances of the traditional coldplate designs.

Keywords: Liquid cooling, design, analysis, coldplate, thermal performance

INTRODUCTION

Power electronics are used in many different applications from inverters in hybrid and electric vehicles, power conversion for wind and solar, traction drives for trains, to MRI amplifiers. Generally the higher power applications require liquid cooling of the power electronics. Assembling power modules on liquid-cooled coldplates is a well-known method for increased cooling. Typical coldplates are simple, large channels in aluminium plates, or

* To whom correspondence should be addressed, email: jesus.moreno@wlv.com.

cooper tubes pressed into aluminium slabs [1-3]. Recently, straight fin micro-channels and pin fin cold plates geometries are becoming popular because of the high power densities to be dissipated [4]. Nonetheless, trends in power electronics systems have placed increasing demands on the efficiencies of the thermal management systems for the power modules. Increases in switching frequencies and voltages ratings of IGBTs as well as denser packing of the die reflect that the cooling capacity of present modules are approaching current liquid cooling limits. Faced with this challenges and limitations, new module cooling solutions need to be explored.

ADVANTAGES OF DIRECT LIQUID COOLING

High-power electronics comprise a number of silicon power dies soldered onto one or more substrates, which are usually direct bounded copper (DBC) metalized ceramics soldered into a base plate. The module is then mounted into a liquid cooled base plate by means of a thermal interface material (TIM). Much of the overall thermal resistance occurs between the module's base and the liquid-cooled cold plate. Direct liquid cooling eliminates the TIM and associated thermal resistance and the liquid directly flows to the backside of module. The DBC substrate is then directly joined to the liquid cooled coldplate eliminating the thermal barrier of the TIM. Moreover, eliminating the TIM material barrier allows to develop high-performance coldplates with high inner heat exchange properties as the improvement in the coldplate is no longer negligible.

COLDPLATE GEOMETRIES AND MANUFACTURING METHODS

Standard manufacturing methods like machining or forging can be used to create the typical straight fin and round staggered pin fin cold plate geometries. Promising Micro Deformation Technology (MDT) is now available to create optimal fin and pin geometries. MDT is able to create custom, high performance mezzo and micro-channels as well as new pin and fin geometries suitable for liquid cooling applications.

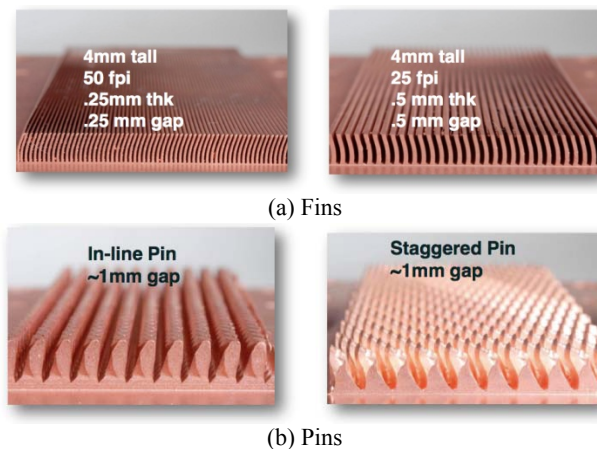


Figure 1. Samples of MDT geometry options.

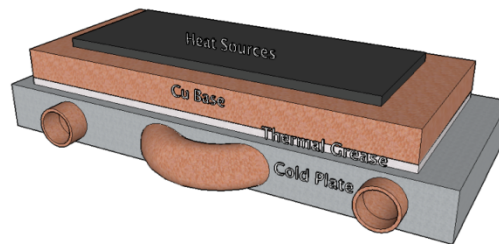
This patented process employs a fixed tool, which mechanically and plastically deforms the work piece to form finite and repeatable fin and pin patterns. Unlike machining or etching this is not a subtractive process, and no metal is wasted. MDT Technology is highly flexible and can create a wide variety of fin, pin and micro-channels geometries.

DESIGN OF A DIRECT LIQUID SYSTEM FOR POWER MODULES

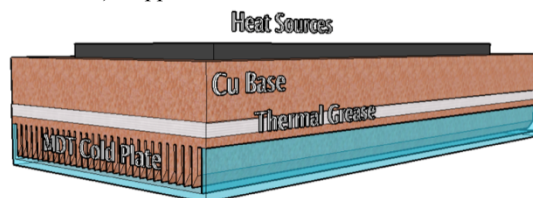
Because of the advantages mentioned above direct liquid cooling appears to be a realistic method to face challenges and limitations of the current liquid cooling module solutions. Additionally direct liquid cooling will provide room for improvement and it will also allow to anticipate future thermal management needs.

Design methodology combines two complementary means of improving the effectiveness of the power module:

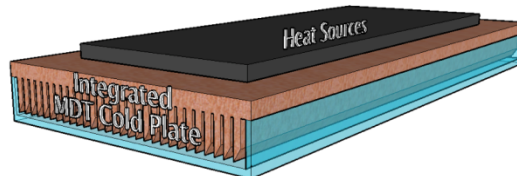
1. Reducing the thermal resistance by eliminating layers between the die and the cooling media
2. Increasing efficiency of the coldplate by improving heat transfer rate from the coldplate to the coolant



a) Copper tubes into aluminum slab



(b) MDT micro-channels coldplate



(c) MDT Integrated cold plate

Figure 2. Conventional and proposed coldplate designs for comparison.

In order to explore means of improving effectiveness of the power module, coldplates designs in Figure 2 are considered. While comparison between (a) and (b) captures

improvement of the heat transfer rate of the cold plate to the coolant, comparison between (a) and (c) captures improvement due to the suppression of the TIM material.

ANALYSIS OF A DIRECT LIQUID SYSTEM FOR POWER MODULES

Computational Fluid Dynamics (CFD) was used to characterize the coldplates. Generated CFD models for the simulations included DBC layer decomposition. Figure 3 shows layer decomposition and corresponding physical properties. The aim of this added complexity is to include the package heat spreading effect in the numerical model in order to provide more realistic results. Most of the results reported in the literature included only the cold plate, the calculated thermal resistivity of the die, DBC AlN and appropriate solder layers need to be added to determine the overall thermal resistivity from the junction to the inlet water.

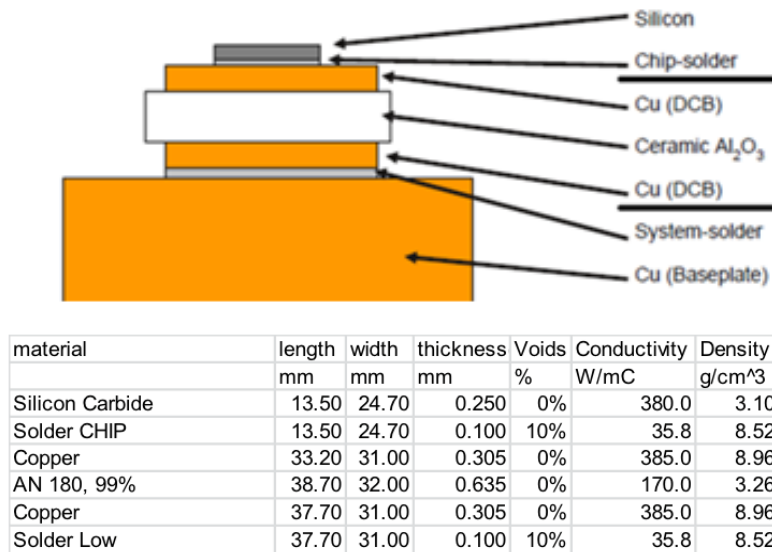


Figure 3. DBC Layer decomposition and properties used to calculate total DBC thermal resistivity.

According to the design guidelines established previously, three 3D-models of power modules were generated for the CFD simulations.

MDT in-line pin fin structure was selected for the MDT coldplates. Based on a previous numerical and experimental study [2] as it provides the best thermal performance per pressure drop. The twisted pin shape adds turbulence and breaks up of boundary layer increasing the heat transfer coefficient with only a minimal impact on the pressure drop when compared to a straight fin or round pin fin.

The cooling fluid is water and the inlet temperature was set to 65°C. The flow rate range was varied between 2 l/min and 6 l/min. They were 8 dies per module and the total power to be dissipated was set 350 W.

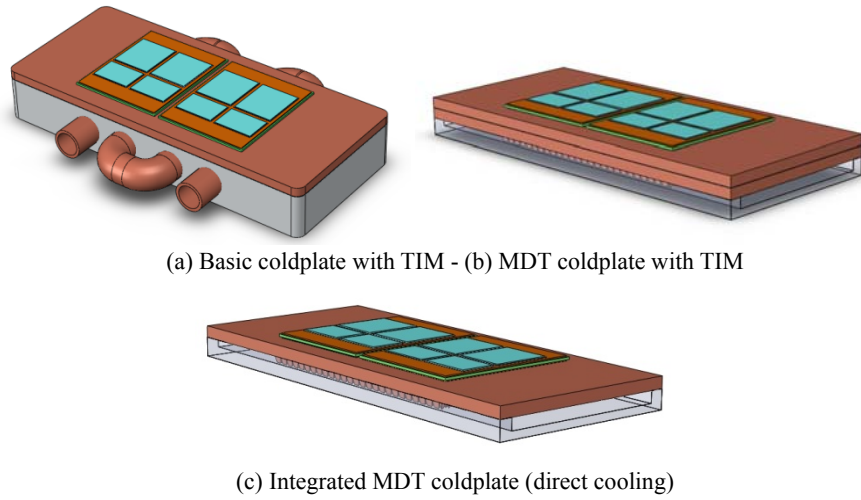


Figure 4. 3D numerical models.

RESULTS

Figure 5 shows velocity streamlines and velocity contour plots for the MDT coldplate. It is important to point out how MDT in-line pin fin geometry insures a uniform flow distribution avoiding dead zones, which could lead to non-desirable high temperature gradients and potential hot-spots.

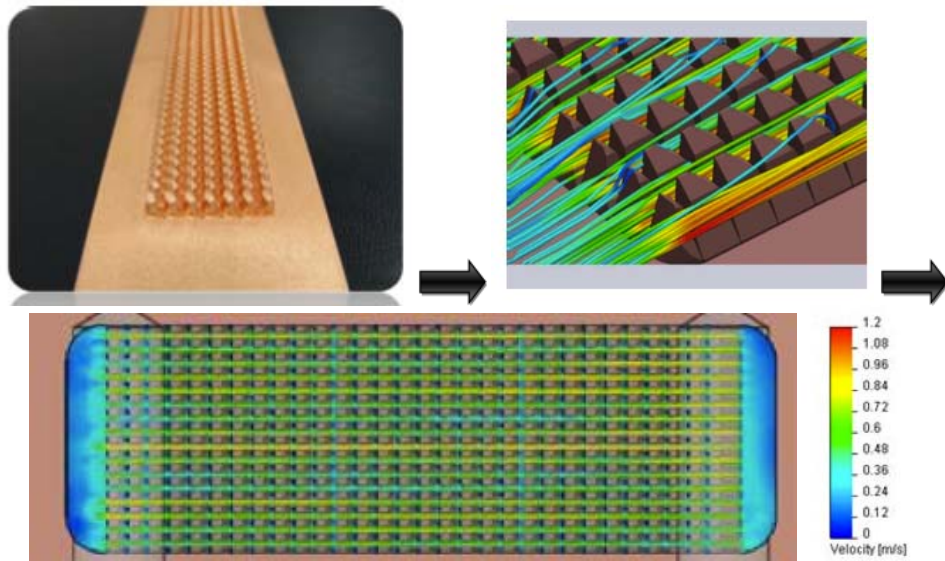


Figure 5. MDT in-line pin fin coldplate: Velocity plots.

Figure 6 shows variation of the thermal resistance versus flow rate. As expected Integrated MDT coldplate induces a significance reduction in the thermal resistance.

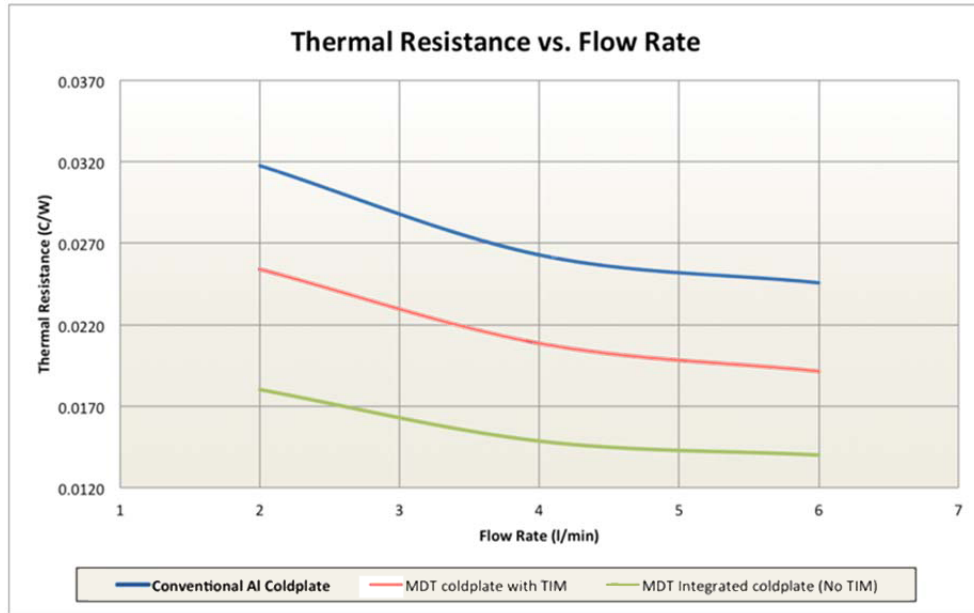


Figure 6. Thermal resistance vs flow rate.

Figure 7 shows variation of the max surface temperature versus flow rate. Integrated MDT coldplate induces the lowest coldplate surface temperature.

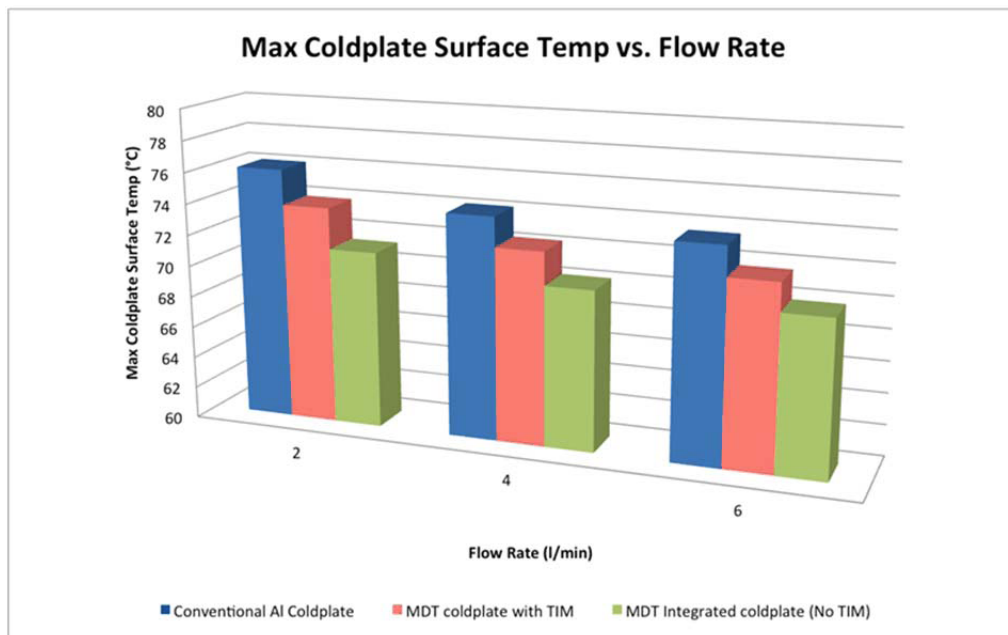


Figure 7. Max. coldplate surface temperature vs flow rate.

Figure 8 shows the thermal resistance enhancement factors for MDT coldplate with TIM and MDT integrated coldplate without TIM. The enhancement of MDT integrated coldplate without TIM is much larger than the integrated coldplate with TIM.

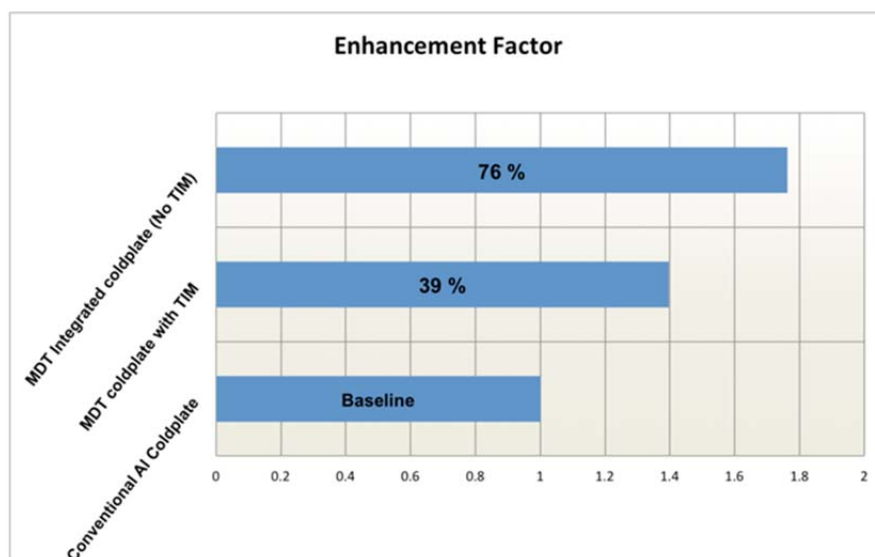


Figure 8. Thermal resistance enhancement factor.

CONCLUSION

Results show that eliminating the thermal interface material (TIM) layer lead to a significant enhancement of the thermal performances in power electronics modules. Moreover, suppression of the TIM layer allows to take advantage of new technologies and manufacturing methods to improve heat transfer rate from the coldplate to the coolant. Direct liquid cooling of power modules, combined with new technologies and coldplate manufacturing methods appears to be a realistic approach to anticipate future thermal management needs of the power electronics systems.

REFERENCES

- [1] F. Nagaume, H. Gohara, S. Adachi, T. Hitachi, H. Shibata, A. Morozumi and A. Nishura, Small size and high thermal conductivity IGBT module for automotive applications, *Proceedings PCIM Europe 2011*, pp.785-790.
- [2] M. Reeves, J. Moreno, P. Beucher, S.-J. Loong and D. Brown, Investigation on the impact on Thermal Performances of new pin and fin geometries applied to liquid cooling of power Electronics, *Proceedings PCIM Europe 2011*, pp.772-778.
- [3] K. Olesen, F. Osterwald, M. Tønnes, R. Eisele and R. Drabek, Direct liquid cooling of power modules in converters for the wind industry, *Proceedings PCIM Europe 2010*, p.738-741.

- [4] Advanced Thermal Solutions, Inc. Norwood, MA, “Direct cooling of power modules using microchannel structures”, Power Electronics Technology, March 2010, <http://powerelectronics.com/thermal-management/direct-cooling-power-modules-using-microchannel-structures>.
- [5] J. Schulz-Harder, Efficient cooling of power electronics, 3rd International Conference on Power Electronic systems and Applications, *PESA* 2009, pp.1-4.

Received 20 July 2012, accepted 30 August 2012.